Polydispersity in Colloidal Phase Transitions

David John Fairhurst

Thesis submitted for the degree of Doctor of Philosophy

Department of Physics and Astronomy
University of Edinburgh
1999

Polydispersity destroys everything.
R. Klein

Crystallinity is Death.
E.S. Fedorov

Well, that's philosophy I've read,
And Law and Medicine, and I fear
Theology too, from A to Z;
Hard studies all, that have cost me dear.
And so I sit, poor silly man,
No wiser now than when I began.
J. Goethe

Abstract

I have studied the effects of polydispersity on the phase behaviour of suspensions of PMMA colloidal spheres on their own and in the presence of non-adsorbed polymer.

I systematically explored the volume fraction–polydispersity ($\phi - \sigma$) phase behaviour of hard spheres (with radii R =167, 244, 300 and 303nm) through direct observations and crystallography measurements. I observed normal crystallisation for $\sigma \lesssim 7.5\%$, and no crystals at $\sigma \gtrsim 18\%$. Samples at $\sigma \approx 9.5\%$ showed crystal-fluid coexistence between $0.52 \lesssim \phi \lesssim 0.56$ but no fully crystalline behaviour above this region. This may be explained by slow particle diffusion in the dense metastable fluid and a glass transition, possibly involving only the larger particles.

The addition of random coil polymer (radius of gyration r_g) to a suspension of single-sized spherical colloidal particles induces an attractive *depletion potential* which, for size ratios $\xi = r_g/R \lesssim 0.2$, has the effect of expanding the crystal-fluid coexistence region. Surprisingly, when such a polymer solution (with $\xi = 0.1$), with a range of concentrations c_p, is added to a polydisperse colloidal suspension ($\sigma \approx 10\%$), crystal formation is actually suppressed. This can be explained by the fact that the polymer compresses the nascent crystal phase to volume fractions greater than the maximum ϕ permitted for polydisperse spheres. By modifying existing free energy equations to include the effects of colloidal polydispersity we also succeed in reproducing the observed phase diagram.

Larger added polymer ($\xi \gtrsim 0.3$) introduces a region of stable gas-liquid coexistence. In systems where crystallisation is suppressed due to polydispersity, this will theoretically be the only transition. By preparing many samples over a range of ϕ and c_p this prediction was observed experimentally for $\xi \approx 0.5$. Fractionation studies on coexisting phases enabled verification of a recent universal law of fractionation in slightly polydisperse systems.

Declaration

The experiments described in this thesis were carried out by myself and, where indicated, in collaboration with colleagues. The data analysis and interpretation is my own work. This thesis has been written entirely by myself.

David Fairhurst

Acknowledgements

As I am quite an accident-prone person, it is perhaps appropriate that the motivation for this work should come from an experimental blunder (which for once was not my own). Following a botched synthesis which created vats of poor quality particles, Wilson Poon, showing his typical enthusiasm and resourcefulness, persuaded me to undertake an epic three year mission to use up these junk particles, in any way I saw fit. Throughout this time I benefitted from Peter Pusey's guidance and seemingly unbounded practical experience and from discussion, computer programs and trips to Unilever courtesy of Patrick Warren. I would like to express my gratitude to my supervisors for these and all their other contributions.

There are many other people who deserve my thanks, including:

Mike Evans with whom I collaborated over physics, beer and badminton courts. I would like to thank him for always having time to skillfully deal with my barrage of pints, shuttle-cocks and questions.

All the members of E=M.C.C. Although officially the departmental cricket team, it is in fact a ramshackle group of friends who will do anything, from rock climbing to fishing, to avoid doing any work. My late submission is testimony to its flourishing success. Thanks to all of you for keeping me sane !

The rest of the "Squidgy" Group, especially those in my office who don't play cricket for being so tolerant.

Kat and Charlotte for introducing me to the wonders of bingo. It really makes growing old something to look forward to.

My family, who despite not being here, were always there.

And finally I thank Jane, for more things than I could possibly list, but above all for hugs.

Contents

List of Figures

List of Tables

Notation

The main variables used throughout this work are listed in this section. Many of these appear in the text with subscripts, the meaning of which should be made clear in the adjacent text.

Thermodynamic Quantities

E	Energy
F	Helmholtz free energy
f	Helmholtz free energy density
G	Gibbs free energy
H	Semi-grand free energy
h	Semi-grand free energy density
Φ	Grand potential
N	Number of particles
p	Pressure
S	Entropy
T	Temperature
V	Volume
v_{m}	Molar volume
μ	Chemical potential
ρ	Number density
Π	Osmotic pressure

Light Scattering

$\boldsymbol{Q}$	Scattering vector
Q	Scattering amplitude
$I(Q)$	Total scattered intensity
$P(QR)$	Individual particle form factor
$S(Q)$	Structure factor
d_{nn}	Nearest neighbour separation

Sample Properties

R, R_c	Colloidal particle radius
σ	Polydispersity
ϕ	Colloidal volume fraction
ϕ_{hs}	hard sphere
ϕ_m	melting
ϕ_f	freezing
ϕ_{cp}	close packed
ϕ_{rcp}	random close packed
ϕ_{gt}	glass transition
$\Delta\phi$	coexistence gap, $\phi_m - \phi_f$
Φ_M	Colloidal mass fraction
β	Fractional mass of core
$\mathcal{M}$	Sample mass divided by mass at melting
χ	Percent crystal
$f_{psd}(R)$	Colloidal particle size distribution
$\langle R^{(n)} \rangle$	n-th moment of radius
$\rho^{(n)}$	n-th density moment
r_g	Polymer radius of gyration
M_n	Number averaged polymer molecular weight
M_w	Weight averaged polymer molecular weight
c^*	Polymer concentration at coil overlap
c_p	Polymer concentration normalised by c^*
n_p	Number density of polymer coils
ξ	Colloid-polymer size ratio
$V^{(free)}$	Free volume
α	Free volume fraction
$c_p^{(free)}$	Polymer concentration in the free volume
$n_p^{(free)}$	Number density of polymer coils in the free volume

Abbreviations

PMMA	Polymethylemthacrylate
PHSA	Poly-12-hydroxystearic acid
SLS	Static Light Scattering
SALS	Small Angle Light Scattering
DLS	Dynamic Light Scattering
RGD	Rayleigh-Gans-Debye
PMT	Photomultiplier Tube
FCC	Face Centred Cubic
HCP	Hexagonal Close Packed
RCP	Random Close Packed
TEM	Transmission Electron Microscope
TCDLS	Two Colour Dynamic Light Scattering

Chapter 1

Introduction

1.1 The Colloidal State

The colloidal realm covers a broad range of liquids. The defining property of such a liquid is that the size of at least one component of these multi-component systems is in the mesoscopic, range between nanometre and micrometer. This condition ensures that the mesoscopic component (particles or droplets or bubbles or molecules or polymers...) is large enough to be treated classically (i.e. they are non-quantum mechanical) but small enough for Brownian motion to dominate over gravitational settling. This definition encompasses many practical and useful substances such as paint, blood, crude oil and many food products. The study of colloids requires an interdisciplinary approach: chemistry provides the synthesis techniques to produce well characterised systems; physics provides the language of statistical mechanics and thermodynamics to describe and predict their behaviour and the experimental tools to investigate these properties directly; industry often provides financial motivation for studying specific systems and can help direct the research by suggesting interesting problems.

1.2 Why Study Colloids ?

Colloidal systems are studied for a number of reasons. As they occur in many substances around us it is important to understand why they behave in the way they do, how they will behave in new situations, and ways of altering this behaviour to suit our needs. Another reason is that they are fascinating to study in their own right: interesting phases can exist and phenomena occur which are not seen elsewhere and therefore warrant in-depth study. Finally, as will be seen later on, colloidal systems can be used as large-scale models of atomic systems. They permit control and observation of properties and phenomenon which are outside the usual physically accessible range. For example it is possible to alter the size,

shape and interactions of particles and to observe phenomena such as crystallisation which occur too quickly in atomic systems to be resolved sufficiently clearly.

1.3 What is Polydispersity ?

Polydispersity arises naturally in almost every colloidal system. It is the property of having many (thus *poly*) non-identical components in the *dispersed* phase of a colloidal system. The variation from one component (e.g. a particle) to the next could be one of many parameters, such as size, shape, charge, density etc. In theoretical studies polydispersity is often ignored, as solving the single-sized or monodisperse problem is often sufficiently complicated. However, as real experiments are always performed on at least slightly polydisperse systems it is essential to quantify the effects of this pervasive phenomenon.

1.4 Thesis Layout

This work is split into three main sections: background information is in Chapters 2 and 3; methodology is in Chapter 4; and experimental observations are in Chapters 5, 6 and 7.

Chapter 2 presents a brief review of some essential concepts of thermodynamics, including the use of different thermodynamic variables to quantify a system and graphical representation of phase behaviour.

Chapter 3 provides an introduction to some of the key concepts in polydispersity, and extends the discussion of graphical representation into multi-component systems. Also presented is a brief, but by no means exhaustive, overview of relevant work in the field of polydisperse phase transitions. It includes results from polymer, hard sphere colloid, interacting colloid, theoretical and computational systems.

Chapter 4 is in essence a technical manual describing *how* I performed the particular experimental measurements required in this scientific investigation. The methods covered include sample preparation and characterisation, light-scattering theory and practice and electron microscope techniques. For those who wish to avoid this level of hands-on detail, or who are already familiar with such methodology, this chapter can initially be skipped and then referred to only when the need arises.

In Chapter 5 results from the investigation of the hard-sphere colloidal system are presented. Chapter 6 is concerned with how these hard sphere systems behave on addition of small random coil polymers and Chapter 7 focuses on the addition of larger polymers to a more polydisperse system.

Chapter 8 attempts to pull all the conclusions together, and presents a few thoughts on future work.

Chapter 2

Thermodynamics of Phase Behaviour

2.1 Introduction

Colloidal suspension are by definition thermodynamic systems. The constituent components are small enough to be significantly affected by Brownian motion, but not so small that quantum effects must be considered. An overview of relevant thermodynamic concepts is useful in understanding this work, so in this chapter I will cover several key areas including: the use of particular thermodynamic variables, thermodynamic potentials, equation of state, the representation of phase behaviour using phase diagrams, transforming between different variables, metastability and kinetics. Most of the material is based on References [1–3]

In later sections, I will discuss how these concepts are used in predicting the behaviour of colloidal suspensions. This will start with the simplest case of hard spherical particles. Theoretically these are often used as a first approximation to many more realistic systems, such as molecular liquids, but can also be realised experimentally. I will also consider the case of hard spheres interacting via the *depletion* potential.

2.2 Overview of Thermodynamic Concepts

2.2.1 Thermodynamic Variables

Thermodynamic systems are typically composed of very many individual components, usually on the order of Avogadro's number $N_{\mathrm{A}} \approx 6 \times 10^{23}$, each with several degrees of freedom. It is amazing that such seemingly chaotic systems can

be identified by a few macroscopic parameters, known as *state variables*. These variables are either intensive (which remain unchanged on combining identical systems) or extensive (additive on combining), and often appear in intensive-extensive pairings, which correspond to generalised thermodynamic forces and displacements. Common examples of these are pressure p and volume V, chemical potential μ and number of particles N, and temperature T and entropy S. Another (derived) variable of importance is the number density $\rho = N/V$. The variables may also be divided into *field* and *density* categories. Field variables, which are always intensive, must have equal values in all coexisting phases. Density variables, on the other hand, which can differ between coexisting phases, can be either intensive or extensive. For example, T, p and μ are intensive field variables, S, V and N are extensive density variables and ρ is an intensive density variable.

2.2.2 Thermodynamic Potentials

For any thermodynamic system we can calculate the energy, or potential associated with it. This can be written as a function of the thermodynamic variables, which can be thought of as generalised displacements. In much the same way as a mechanical force is found by taking the derivative of the potential with respect to the displacement, we can deduce the other related thermodynamic variables by differentiating the thermodynamic potential with respect to the chosen displacement variable. For example, temperature is the derivative of energy with respect to entropy, $T = \partial E/\partial S$. The energy E is useful when considering isolated (micro canonical) systems and is a function of S and V. We can also define a useful energy associated with a canonical ensemble, the Helmholtz Free Energy $F(T, V)$ in which E and P fluctuate. The Gibbs Free Energy $G(T, P)$ and the Enthalpy $H'(S, P)$ can then be derived by suitable transformations. These energies are extensive in N the number of particles present, which is fixed. If N is also permitted to fluctuate, the grand canonical ensemble, then the *grand potential* $\Phi(T, V, \mu)$ is the relevant energy.

The thermodynamic variables and potentials cannot all be assigned arbitrary values simultaneously: in general only three can be altered independently. For example, for a fixed number of particles N, we cannot take the system to all locations in p–V–T space but are restricted to points which lie on the p–V–T surface. This surface is given by the *equation of state*.

2.2.3 Phase Equilibrium and Phase Diagrams

A system is at equilibrium when the average values of all of the state variables are constant in time, which occurs when the relevant thermodynamic potential is minimised. When phase coexistence is a possibility, the individual phases must have equal field variables, T, μ and p. If the relevant thermodynamic potential of

the system is known, it can be minimized for states which fulfil these coexistence conditions, and thereby coexisting phases can be predicted. A theoretical phase diagram can be plotted depicting the phase behaviour at various values of the state variables. Likewise, phase diagrams can be determined experimentally. A system, initially homogeneous, is observed over a range of variables (usually T, p and V) and at each location the question "Does the system do anything ?" is asked. By this we mean will it sit there in the homogeneous state we have left it in or will it change somehow: the bulk appearance may alter (e.g. from a liquid to a solid phase) or the system may separate into two or more coexisting phases. A simple experiment involves changing relevant parameters and determining the regions of phase space in which different behaviour is observed. The boundaries between such regions are called phase boundaries. The nature of these regions will depend upon the variables used to characterise the system. Field variables must have equal values in all phases at equilibrium so coexisting phases are marked by points in a field-field representation. In a density-field representation, the density variable can take on different values so coexistence is indicated by a so called *tie-line* connecting the two phases. This line will be horizontal if we plot the field variable on the vertical axis. In a density-density plot, the tie-lines are at an angle, indicating a difference in both variables at coexistence.

Conservation of matter, when applied to samples situated on tie-lines yields the so called *lever rule*. For the simple case of a sample with an initial density variable ρ_{i} which separates into two coexistence phases with densities ρ_1 and ρ_2, conservation of the total particle number yields

$$\begin{aligned} N_{\mathrm{T}} &= N_1 + N_2 \\ V_{\mathrm{T}}\rho_{\mathrm{i}} &= V_1\rho_1 + V_2\rho_2 \\ \rho_{\mathrm{i}} &= f_1^{(\mathrm{V})}\rho_1 + f_2^{(\mathrm{V})}\rho_2, \end{aligned} \tag{2.1}$$

which indicates the fractional volume ($f_1^{(\mathrm{V})} = V_1/V_{\mathrm{T}}$) of each of the coexisting phases. It is called the lever rule not after the soap product pioneer, but because of the physical picture of balancing a tie-line at the initial composition with weights relative to the amounts of the two phases at either end. The lever rule can be extended to multiple phases, and multiple density variables.

2.2.4 Gibbs' Visualisation of Coexistence

In Reference [3] Gibbs presents an alternative technique for visualising how this procedure for determining phase coexistence is performed. As the energy is given by $\mathrm{d}E = T\mathrm{d}S - p\mathrm{d}V$ a three dimensional energy surface can be described in terms of S and V. The slope along the S and V directions respectively gives the temperature and the pressure. For a simple substance (e.g. Argon) $E(S, V)$ will have three minima corresponding to gaseous, liquid and solid phases. One common tangent plane exists between these three minima (a three legged table cannot wobble !) and describes a triangle. The fact that this triangle is flat

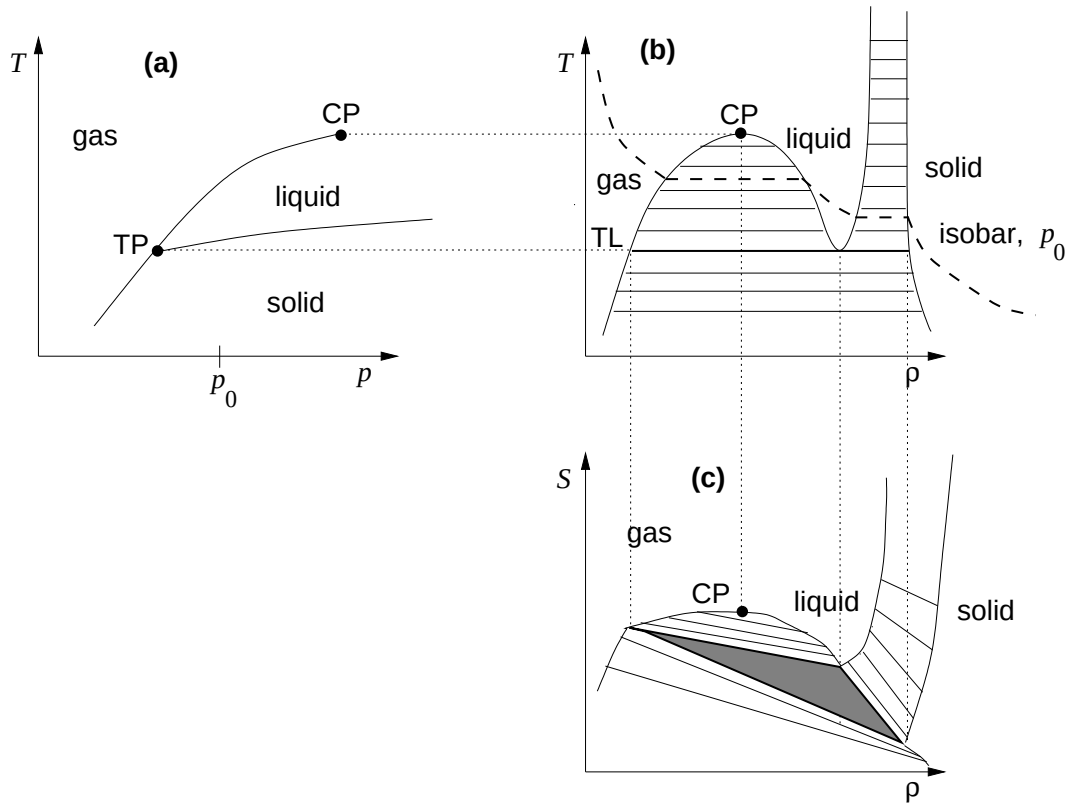

Figure 2.1: Phase behaviour represented in three different representations. (a) Shows field-field variables in which coexistence is indicated by lines separating the homogeneous or single phase regions. Gas-liquid coexistence terminates at the critical point, CP. Three phases coexist at the triple point, TP. In (b) density-field variables are used and coexistence occurs within a region, spanned by tie-lines connecting coexisting phases. Three phases are seen along the triple line, TL. Plotting isobars allows recovery of lost information due to the projection. Density-density variables are used in (c). Tie-lines are now slanted as both variables can partition between coexisting phases. A three phase triangular region is seen.

indicates that the pressure and temperature are constant across this three phase region, the inclination of the triangle indicating the values of these quantities. For all values of (S,V) within the triangle, the energy of the single phase surface will be greater than that of the three phase triangle, so the system can minimise its energy by separating into the three phases (gas, liquid and solid) indicated by the vertices. The entropy and volume will be given by the sum of the values at the three vertices, weighted by the relative proportion of each phase. Now, the energy surface can be tipped over any of the three edges of the triangle (equivalent to altering T and p), leaving only two points in contact with the plane. The lines marked on the plane as the surface is pushed further indicate two phase coexistence regions, and the inclination of the tangent plane gives the value of T and p at coexistence. In the case of the gas-liquid branch, the two coexistence points approach each other until, at the critical point, they meet.

2.3 Phase Behaviour of Colloidal Systems

2.3.1 Colloids as Atoms

A colloidal suspension is structured on two very different length scales. Colloidal particles have radii in the range 50nm to 1μm and are suspended in a solvent of molecules a few orders of magnitude smaller. Thermodynamically, this permits the separation of the behaviour of the two species: the suspending liquid can be treated as a continuum existing in the complicated volume defined by the container walls and the colloidal particles. The exact dimensions of this region will change as the colloidal particles move, but the overall volume and surface area will, to a very good approximation, remain constant. (The approximation only breaks down when we look on the very short length scale of the molecules and realise that solvent molecules are excluded from a small region surrounding each colloidal particle.) As these two quantities (at constant temperature) completely define the characteristics of the liquid, it is thermodynamically almost totally decoupled from the particles. In other words, the partition function of the fluid is independent of the partition function of the colloidal particles and the two can be separated, reducing the problem to an effective *one component system*. The suspending fluid acts as a heat bath ensuring equal temperature throughout the system and allowing the particles to reach thermal equilibrium. The colloidal system, although many times larger than an atomic system, can then be described by the same physics used in atomic physics, where for example the osmotic pressure Π of the colloidal fluid is equivalent to the pressure of a molecular fluid, and equations of state developed for the later are equally applicable to the former (provided that interactions are equivalent).

Atomic processes which occur much too quickly to observe in detail (such as crystallization, and early time phase separation) are more accessible in colloidal systems. This is because particle sizes are that much greater, and the particle

motion is diffusive, not ballistic as for molecules. To illustrate the large difference in time-scales we can calculate a characteristic time-scale, equal to the time taken for a particle to travel a distance equal to its own radius. For a ballistic, thermal molecule, the kinetic energy is given by the equipartition of energy from which we find the thermal velocity. The time taken to travel one radius is therefore

$$t_{\mathrm{bal}} = R\sqrt{\frac{m}{3k_{\mathrm{B}}T}} \approx 10^{-12}\mathrm{s}, \tag{2.2}$$

using typical values of the molecular size ($R \approx 1$nm) and mass ($m \approx 10^{-25}$kg) and at temperature $T = 300$ K. On the other hand, a colloidal particle in a solvent of viscosity $\eta \approx 10^{-3}$Pa.s at the same temperature will diffuse its own radius ($R \approx 100$nm) in a time given by

$$t_{\mathrm{diff}} = \frac{6\pi\eta R^3}{k_{\mathrm{B}}T} \approx 10^{-3}\mathrm{s}. \tag{2.3}$$

It is clear from this calculation that colloidal process will occur approximately 10^9 times slower than the comparative molecular process.

Another crucial difference between the dynamics in molecular and colloidal dynamics are hydrodynamic effects. These are ignored in this simplified discussion but interested readers can find thorough treatment of this important phenomenon by Batchelor in [4], by Dhont in [5] and the references contained therein.

2.3.2 Free Energies

As was discussed previously, there are several different thermodynamic potentials, which are functions of different combinations of the thermodynamic variables. The selection between the possible choices is made by consideration of the most useful and relevant variables which describe the system. For the colloidal systems under study in this work, temperature, volume and particle number are held constant. For this reason the Helmholtz free energy $F(T, V, N)$ is generally used, but sometimes it is useful to permit particle number fluctuations and transform to the grand potential $\Phi(T, V, \mu)$ for calculational purposes.

As both F and V are extensive they must scale linearly with the amount of matter, and therefore with N. So if a system in equilibrium is divided into small (but still macroscopic) regions, the quantities T, F/N and V/N (and p, on which F does not depend) will be identical in all regions and equal to the overall values of these quantities. F/N, which does not change from region to region can, only be a function of variables which likewise are equal in all these regions, namely V/N and T. Mathematically, we write

$$\frac{F(V,T)}{N} = h\left(V/N, T\right), \tag{2.4}$$

where h is some function. The free energy density $f = F/V$ is a more convenient intensive variable and can be written in terms of ρ and T:

$$\frac{F(V,T)}{V} = \frac{N}{V} h\left(V/N, T\right) = \rho h\left(1/\rho, T\right) = f(\rho, T). \tag{2.5}$$

We show that an arbitrary function of the form $a + b\rho$ can be added to $f(\rho)$ without altering the predicted phase behaviour.

We can now examine the conditions for thermal coexistence (equal T, p and μ), in terms of this new variable f. In hard core systems, temperature merely scales the overall free energy so in the following discussion it has been dropped. In Figure 2.2 typical free energy densities for two phases which can coexist are plotted schematically.

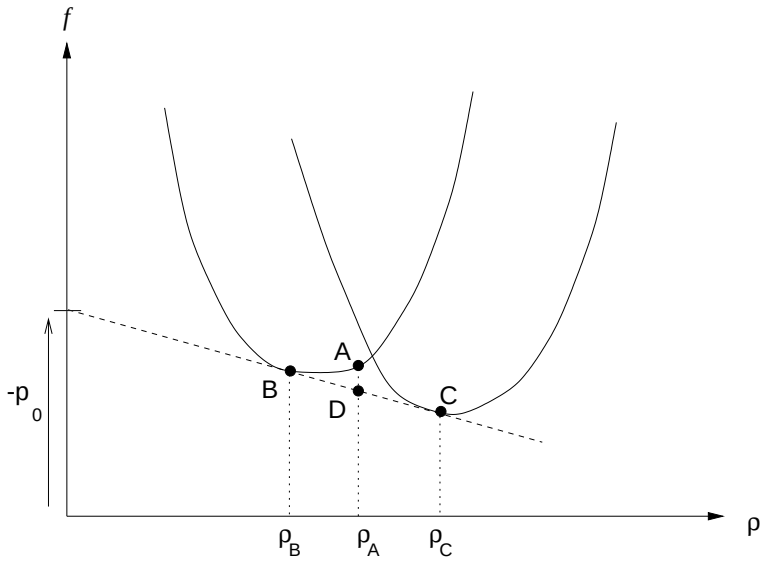

Figure 2.2: Free energy curves and the common tangent construction. A system prepared at point A can lower its free energy by separating into two coexisting phases given by B and C.

Firstly we can rewrite the chemical potential μ in terms of $f(\rho)$ as

$$\begin{aligned}
\mu &= \left(\frac{\partial F}{\partial N}\right)_V \\
&= V\left(\frac{\partial f}{\partial N}\right)_V \\
&= V\left(\frac{\partial \rho}{\partial N}\right)\left(\frac{\partial f}{\partial \rho}\right)_V \\
\mu &= \left(\frac{\partial f}{\partial \rho}\right)_V .
\end{aligned} \tag{2.6}$$

In other words, μ is given by the slope of $f(\rho)$ and therefore the equal μ constraint leads to the condition that coexisting phases must have equal slopes. Addition

of an arbitrary function of the form mentioned above, will change the chemical potential: $\mu \to \mu + b$.

The pressure p is given by

$$\begin{aligned} -p &= \left(\frac{\partial F}{\partial V}\right)_N \\ &= f + V\left(\frac{\partial f}{\partial V}\right)_N \\ &= f + V\left(\frac{\partial \rho}{\partial V}\right)\left(\frac{\partial f}{\partial \rho}\right)_N \\ -p &= f - \rho\left(\frac{\partial f}{\partial \rho}\right)_N . \end{aligned} \tag{2.7}$$

After a moment's thought, we can see that this expression means geometrically that the pressure at a given ρ is given by the intersection on the $f(\rho)$ axis of the tangent to the free energy density at that ρ, as indicated on Figure 2.2. The arbitrary function alters the pressure, $p \to p - a$.

The coexistence conditions of equal μ and p are satisfied if two phases (points on $f(\rho)$) have tangents with equal slopes and equal intercepts, i.e. they share a *common tangent*. Such a common tangent is shown in Figure 2.2, between two coexisting phases, B and C. The free energy of a system containing both phases B and C is a simple weighted sum of $f(\rho)$ in each individual phase. By increasing the fraction of phase C present, from 0% to 100%, the free energy of the two phase system will move along the common tangent from B to C.

The energetic stability of the two phase coexistence is then determined by considering points on the free energy curves between the two coexisting phases. In Figure 2.2 all points on both curves between B and C are above the common tangent, and can lower their overall free energy by phase separating. The relative amounts of the two phases are given by the lever rule. For example, a system prepared at A can reduce its energy to D by forming roughly equal amounts of B and C.

2.3.3 Hard Spheres

Phase Behaviour

A collection of hard spheres is, arguably, the paradigmatic non-ideal system (either classical or quantum). The particles considered are identical spheres which do not interact except at contact, when the repulsion is infinite. Hard spheres are often used as the starting point from which properties of fluids can be calculated by treating any (finite) attractions as perturbations. Theoretically and computationally hard spheres possess the obvious advantage of not having long range

interactions (which give rise to mathematical complications). Also, as no energy scale is present, altering the temperature makes no difference to the behaviour, and the system can be characterised by one parameter, the number density ρ, or more often the volume fraction

$$\phi = \frac{4}{3}\pi R^3 \rho, \tag{2.8}$$

where R is the particle radius.

In experiments, real spherical particles interact through a short range van der Waals force, caused by electro-magnetic attraction of induced dipoles in nearby particles. This leads to irreversible clustering and aggregation of unstabilised hard spheres. By chemically grafting a thin layer of polymer hairs to the surface of each particle, the van der Waals attraction can effectively be screened out. When the particles approach one another the polymer brushes begin to interpenetrate and must pay a very high entropic cost for the loss of degrees of freedom. Consequently, the interaction between such *sterically stabilised* particles is a very good approximation to that of hard spheres.

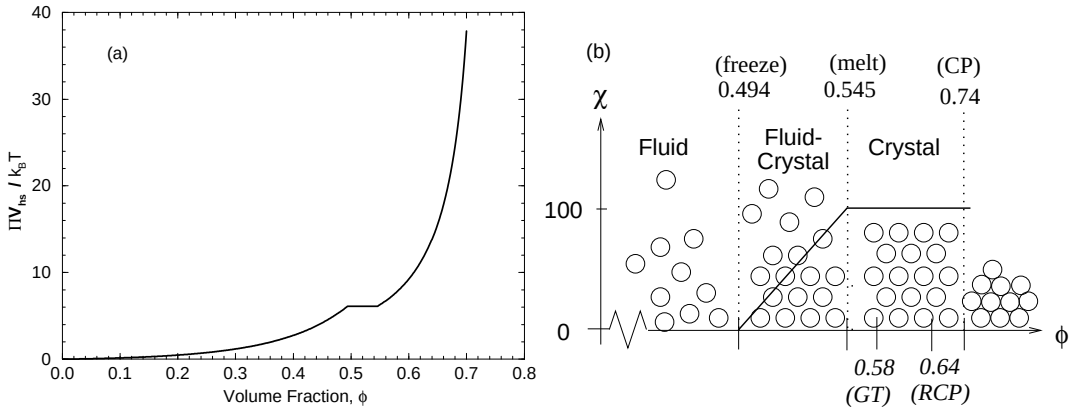

Figure 2.3: (a) The hard sphere equation of state showing the variation in the osmotic pressure Π times the particle volume $V_{\rm hs}$ in units of $k_{\rm B}T$. (b) The phase diagram for hard spheres is illustrated along the x-axis. For clarity the percent of crystal χ (not a true thermodynamic variable) as a function of ϕ is plotted on the y-axis. The equilibrium melting and freezing points and the maximum closest packing of hard spheres (CP) are indicated above the plot. Non-equilibrium behaviour, the glass transition (GT) and random close packing (RCP) are in italics below.

Almost single sized hard spheres have been extensively studied experimentally, theoretically and by computer simulation. The equilibrium phase behaviour is very well established. The equation of state is shown in Figure 2.3(a), calculated using expressions derived by Carnahan and Starling [6] for the fluid portion and by Hall [7] for the solid. Remarkably these largely phenomenological equations of state agree well with simulation data of Hoover and Ree [8] and recent experimental measurements by Phan and colleagues [9]. Coexistence is indicated

by the flat portion of the curve during which an increase in ϕ does not result in an increase in the osmotic pressure Π as crystal forms at the same pressure but higher density than the fluid it replaces.

The x-axis of Figure 2.3(b) shows the complete phase diagram for the hard sphere system. (The percent of crystal present χ is plotted along the y-axis, however as this is not a true thermodynamic variable, the two-dimensional picture does not constitute a real phase diagram.) At low ϕ the particles are ergodic and explore the whole available volume; they are arranged with short range order which is lost over long distances. This phase is called a colloidal fluid. At larger volume fractions, the lowest free energy state is the coexistence of colloidal fluid and crystal. Over this range the volume fraction of the fluid and crystal remain fixed at 0.494 (freezing) and 0.545 (melting) respectively. The overall value of ϕ increases by crystal forming at the expense of fluid. Experimentally, small (<1mm) crystallites are observed to nucleate homogeneously throughout the sample, sediment because of the density difference and form a polycrystalline phase at the bottom of the container. As ϕ is increased above the melting point, $\phi > 0.545$, crystallites alone are observed until ϕ reaches the theoretical closest packing for spheres in three dimensions, $\phi_{\rm cp} = \pi\sqrt{2}/6 \approx 0.74$. If the particles are randomly arranged, then the closest packing is given by the random close packed value of $\phi_{\rm rcp} \approx 0.64$. In practice however, a glass transition is encountered at $\phi = \phi_{\rm gt} \approx 0.58$ at which homogeneous nucleation of crystals ceases due to the arrest of long time diffusion.

For a long time, the existence of a crystal phase in a purely hard sphere system was disputed. Without attractive interactions, many argued that a crystal phase could not possibly form. Its stability can be understood by considering the two types of entropy involved: configurational and vibrational. A crystal phase has lower configurational entropy than a fluid, but as in a crystal the spheres have extra room locally in which to move, this increase in vibrational entropy more than compensates for the long range order. The enhanced packing of ordered hard spheres can be seen by comparing the close packed values quoted above: a randomly ordered phase has maximum packing at $\phi \approx 0.64$ whereas ordered hard spheres at the same ϕ will have space in which to vibrate, as maximum crystalline packing does not occur until $\phi \approx 0.74$.

Free Energies

The hard sphere phase behaviour may be predicted by considering the free energies of the two states. In Figure 2.4 plots of calculated free energy curves for the hard sphere fluid and crystal are shown. The fluid phase free energy has been calculated from the simple Carnahan and Starling (C-S) equation of state [6], which diverges unrealistically at $\phi = 1$. A Padé approximant (the official name for the ratio of two polynomials) calculated by Yuste and co-workers [10], which diverges, more realistically near the glass transition, is also shown. Other expressions are also available in the literature (see e.g. [11]). For the solid, the continuous curve comes from a Padé fit to simulation data by Hall [7] and the dashed curve from

a cell theory free energy [12, 13]. Deviations in the solid branch predictions are small, which is encouraging for the relatively straight-forward cell theory prediction. The inset in Figure 2.4 shows the common tangent construction between the fluid phase at $\phi = 0.494$ and the crystal at $\phi = 0.545$.

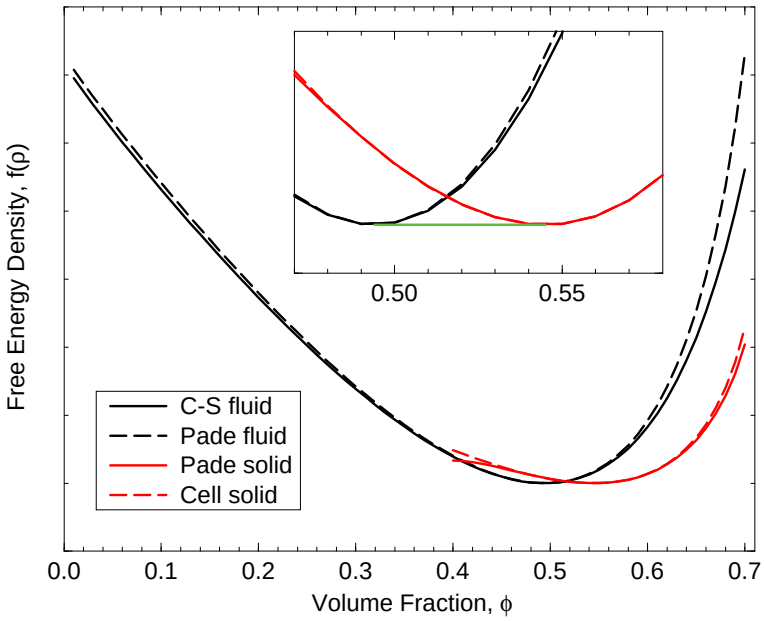

Figure 2.4: Hard sphere free energy curves. The fluid phase curves (left) come from the Carnahan and Starling (C-S) equation of state [6] and from a Padé approximant [10]. The solid phase curves (right) are from a polynomial fit to simulation data [7] and from a cell theory free energy [12, 13]. The inset shows an enlargement around coexistence, and the location of the common tangent. The fluid and solid phases have volume fractions of 0.494 and 0.545 respectively.

Non-Equilibrium Behaviour

The hard-sphere system can exhibit non-equilibrium behaviour, which cannot be deduced from free energy considerations. Above the glass transition ($\phi > \phi_{\rm gt} \approx 0.58$) homogeneously nucleated crystals are no longer observed. A few large crystals are seen to grow from the walls, the meniscus and other imperfections in the system. Much work has been carried out on glassy systems, and I direct the interested reader to the literature [14, 15].

2.3.4 Colloid-Polymer Mixtures

Historically, free polymer was added to commercial suspensions in an attempt to increase their stability. The reasoning was that the polymer would increase

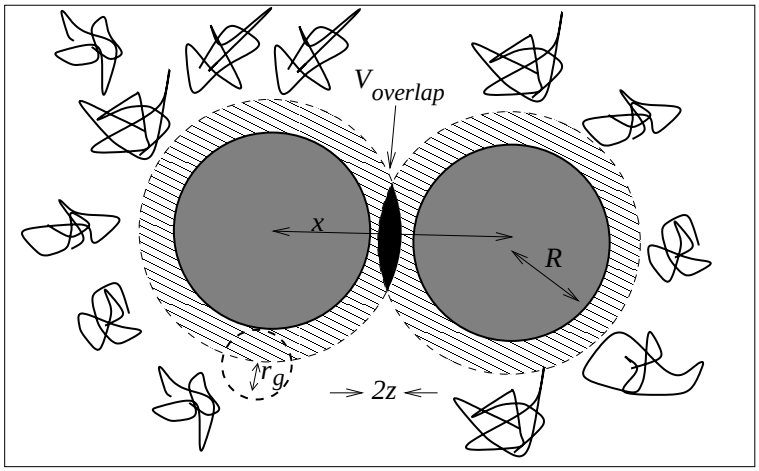

Figure 2.5: Schematic illustration of depletion and free volume. Two particles (shaded solid gray) and the zones around them from which polymers are excluded (hatched). The overlap volume is the intersection of these two zones. The region unshaded corresponds to the free volume.

the viscosity of the system thereby slowing down any aging processes (e.g. sedimentation or creaming), prolonging the shelf-life. More added polymer would result in higher viscosities and slower dynamics. On the contrary, when sufficient polymer was added, a rapid phase separation was observed. This phenomenon has been explained by the depletion force (or macro-molecular crowding), which arises when the polymer coils (or any other depletants) are excluded from the region between adjacent particles. The osmotic force due to the depletants is unbalanced and results in an attractive force between the particles, which in turn can lead to flocculation, aggregation, or phase separation. Besides the industrial importance of understanding this phenomenon, it can also be used to extend the "colloids as atoms" analogy of hard spheres, by enabling experimentalists to introduce a tunable attraction between particles. By so doing, insights into fundamental questions of condensed matter physics, such as the conditions required for the existence of a critical point, and the rôle of metastable states in phase ordering are gained.

Depletion Potential

The first theoretical interpretation of phase separation due to an added, non-adsorbed component was due to Asakura and Oosawa [16], and was later developed independently by Vrij [17], who considered the situation illustrated in Figure 2.5. Polymer coils are assumed to be spheres of radius equal to the polymer radius of gyration r_{g} and colloid particles are of radius R. As the two species are mutually impenetrable, around each colloidal particle there is a region of thickness r_{g} from which the centre of any polymer coil is excluded, and consequently, each particle feels an osmotic pressure due to the rebounding polymer coils, Π_{p} .

When colloidal particles approach, polymer is squeezed out of the gap described by the overlap of the depletion zones, the overlap volume V_{overlap}. There is no osmotic pressure contribution from the polymer-free V_{overlap} so the particles are drawn towards this region of pure solvent. The force can be expressed as an attractive pair potential, U_{dep}, dependent on the centre-centre separation x:

$$U_{\text{dep}}(x) = \begin{cases} +\infty & \text{for} \quad x \leq 2R \\ -\Pi_{\text{p}} V_{\text{overlap}}(x) & \text{for} \quad 2R < x \leq 2(R + r_{\text{g}}) \\ 0 & \text{for} \quad x > 2(R + r_{\text{g}}) \end{cases} \tag{2.9}$$

An analytic expression is available for V_{overlap}, which has a simple form in terms of a new variable z, the half width of the overlap volume ($x = 2(R + r_{\text{g}} - z)$).

$$V_{\text{overlap}}(z) = \frac{2}{3}\pi z^2 \left[3(R + r_{\text{g}}) - z\right]. \tag{2.10}$$

At contact ($x = 2R$ or $z = r_{\text{g}}$) this expression reduces to

$$V_{\text{overlap}} = \frac{2}{3}\pi r_{\text{g}}^2 (2r_{\text{g}} + 3R). \tag{2.11}$$

Assuming the polymers behave ideally (which in practice is approximately true at the theta temperature), the osmotic pressure is given by

$$\Pi_{\text{p}} = n_{\text{p}}^{(\text{free})} k_{\text{B}} T, \tag{2.12}$$

where $n_{\text{p}}^{(\text{free})}$ is the number of polymer particles divided by the total *free volume* $V^{(\text{free})}$. This is the total volume available to the polymer centres (i.e. the system volume V minus the volume taken up by the particles and their depletion zones), which is represented by all the unshaded region in Figure 2.5, and can be written as a fraction of V,

$$V^{(\text{free})} = \alpha V. \tag{2.13}$$

The function α, the free-volume fraction is dependent upon colloidal volume fraction ϕ, polymer number density $n_{\text{p}}^{(\text{free})}$, the colloid-polymer size ratio, $\xi = r_{\text{g}}/R$ and the positions of all the colloidal particles. In the case of very dilute colloid and polymer in which no depletion zones overlap, the volume inaccessible to the polymer coils is simply ϕ scaled by $(1 + \xi)^3$, so

$$\alpha \approx 1 - \phi(1 + \xi)^3. \tag{2.14}$$

A complete expression describing all the dependencies of $\alpha(\phi, n_{\text{p}}^{(\text{free})}, \xi)$ would be ideal, however at present this is not available. One approximation, which comes from taking a mean-field average over colloidal particle coordinates which are assumed to be unperturbed by the presence of polymer, can however be obtained from scaled particle theory (SPT) [18],

$$\alpha = (1 - \phi) \exp\left[-A\gamma - B\gamma^2 - C\gamma^3\right] \tag{2.15}$$

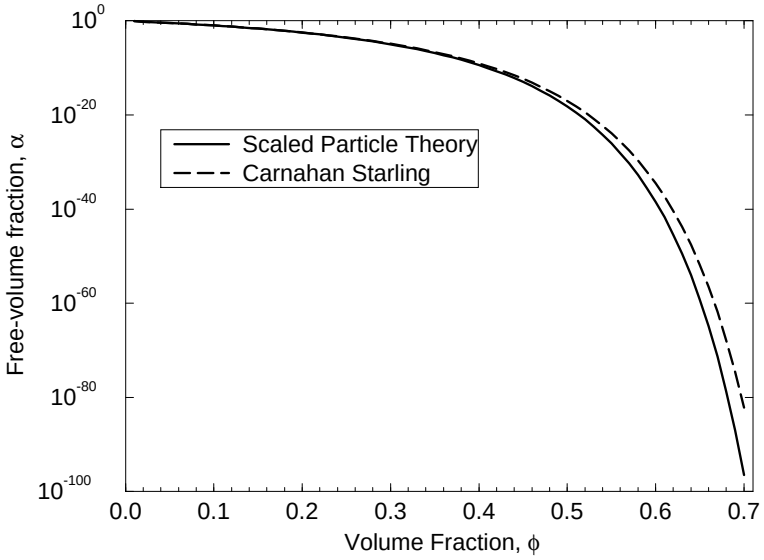

Figure 2.6: Free-volume fraction α, calculated from scaled particle theory for $\xi = 1$ and using the Carnahan-Starling equation of state.

in which $\gamma = \phi/(1-\phi)$, $A = 3\xi + 3\xi^2 + \xi^3$, $B = 9\xi^2/2 + 3\xi^3$ and $C = 3\xi^3$. An expression for α when $\xi = 1$ can also be obtained using the fluid free energy, and the equation

$$\alpha = \exp\left[-\frac{\mu^{\mathrm{ex}}}{k_{\mathrm{B}}T}\right] \tag{2.16}$$

where μ^{ex} is the excess (i.e. non-ideal) part of the chemical potential derived by differentiating the fluid free energy. This formula comes from considering the potential energy required to insert an extra sphere into a fluid at a given ϕ. It is interesting to compare the $\xi = 1$ form of the α determined from SPT, with that calculated from the Carnahan-Starling equation of state. As can be seen in Figure 2.6 the agreement is good, but not perfect.* Ideally, we would demand consistency between these expressions, but until a simple expression for calculating the free energy (and hence a consistent α) for arbitrary hard sphere mixtures is available, we are content to tolerate this small discrepancy.

Recent simulations performed by Dijkstra, van Roij and Evans [19] have studied the phase behaviour of additive mixtures of hard spheres. They conclude that the depletion description, which incorporates an approximation for α are in remarkable agreement with their more detailed simulation results. Experimental tests have also been carried out to investigate the range over which the depth of the depletion potential varies linearly with polymer number density, as predicted by Equation 2.12. Ohshima *et al.* [20] used laser radiation pressure to directly measure the depletion potential and conclude that "the observed force almost coincides with the predicted one". Ye *et al.* [21] inferred information regarding the depletion potential from neutron scattering measurements and find that

*This discrepancy can be foreseen, as the Carnahan-Starling result is in fact a fortuitously accurate combination of SPT and an equation of state derived by a different route.

"the magnitude of the attraction is found to increase linearly with concentration, but it levels off at higher polymer concentration." In summary, it appears that despite the approximations in constructing the theory of depletion, it offers a robust description of colloid-polymer mixtures, provided that polymer-polymer interactions are not dominant.

Free Energies

Having determined how the addition of free polymer can lead to an effective depletion potential, it is an obvious next step to inquire about the behaviour of such a colloid-polymer mixture [22]. Keeping the same assumptions as before (i.e. ideal polymers constrained to move in the free volume) we can write the Helmholtz free energy F of the composite system as the sum of the colloidal and polymeric contributions,

$$F = F_{\mathrm{c}}(N_{\mathrm{c}}, V) + F_{\mathrm{p}}(N_{\mathrm{p}}, V_{\mathrm{p}}). \tag{2.17}$$

The colloidal and polymeric free energies (F_{c} and F_{p}) are only dependent on the number density (N/V) of the relevant component (but it is more usual to use the volume fraction ϕ for indicating the density of colloidal particles) and the volume in which it is free to move (V and V_{p}). The expression for the colloidal fluid can be that due to Carnahan and Starling, or more recent improvements on this, depending on the desired accuracy. Irrespective of the chosen expression, the pure colloidal free energy will only display a single minimum, indicating that the fluid is locally stable at all values of ϕ. The free energy of a crystal formed from a colloid-polymer mixture can also be calculated using this method. The expression for the polymer free energy is simply that of an ideal gas constrained to move in a volume αV, i.e. $F_{\mathrm{id}}(\rho_{\mathrm{p}}, \alpha V)$. By differentiation this gives the ideal gas equation,

$$\Pi = \frac{N_{\mathrm{p}} k_{\mathrm{B}} T}{\alpha V} \tag{2.18}$$

relating the polymer osmotic pressure Π to the free volume αV, the total number of polymer coils and the temperature T.

For practical purposes, it is actually very convenient to transform to a new ensemble, in which the chemical potential of the polymer, not the actual number of coils, is fixed. This is a *semi-grand ensemble*, and the associated free energy H only depends on ϕ and μ_{p}, the polymer chemical potential. Dropping the volume dependence, it can be written as

$$H(\phi, \mu_{\mathrm{p}}) = F_{\mathrm{c}} - \alpha V n_{\mathrm{p}}^{(\mathrm{free})} k_{\mathrm{B}} T \tag{2.19}$$

where we remember that α is a function of ϕ and ξ. The polymer concentration in the free volume $n_{\mathrm{p}}^{(\mathrm{free})}$ is given by $\lambda_{\mathrm{p}}^{-3} \exp\left[\mu_{\mathrm{p}}/k_{\mathrm{B}}T\right]$ where λ_{p} is the de Broglie wavelength of the polymer coil. In coexisting phases, equality of chemical potentials, of all species, must occur. We can enforce the equality of polymer chemical potential in the semi-grand ensemble by simply fixing μ_{p} through $n_{\mathrm{p}}^{(\mathrm{free})}$.

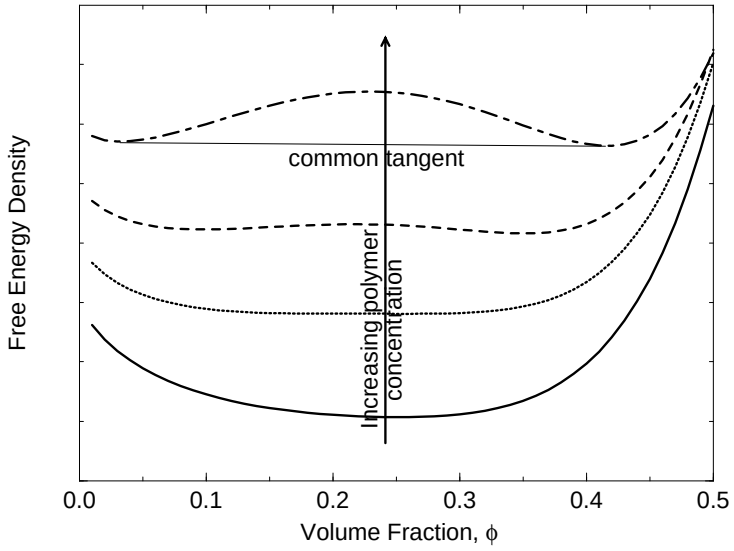

Figure 2.7: Free energy curves for colloid-polymer mixtures. The emergence of a two phase coexistence via a second order phase transition is apparent on increasing the polymer concentration. These curves bear a close resemblance to those seen in atomic systems.

Coexisting phases, which must have equal colloidal chemical potential and osmotic pressure can then be determined by using the double tangent construction on the free-energy density h . Figure 2.7 shows four free energy curves for a colloid-polymer mixture with size ratio $\xi = 0.5$ covering a range of polymer concentrations. The curve corresponding to the lowest value of $n_{\rm p}^{(\rm free)}$ (solid curve) shows a single minimum, indicating that the fluid phase is locally stable everywhere (there may still be coexistence with a crystal phase). The next curve has a flat region near $\phi \approx 0.25$ around which the system can fluctuate and give rise to pockets of varying density with very little free energy cost. This is close to the critical point of the system. The next two curves show how the critical point splits smoothly to make two distinct phases. In analogy with atomic systems, the high density phase is commonly called a colloidal liquid and the low density phase is a colloidal gas. The common tangent is drawn on the uppermost curve indicating the gas and the liquid phases at either end and the lever rule can be applied to the tangent to predict how much of each phase is expected. This behaviour is similar to that seen in atomic systems near a critical point: an increase in polymer chemical potential is equivalent to a decrease in temperature, as both result in a strengthening of the effect of the interparticle attraction. It is interesting to then find which quantity, in colloid-polymer systems, is analogous to entropy in atomic systems. It must be an intensive variable which when multiplied by the chemical potential gives the units of energy. It turns out that $n_{\rm p}$, the number density in the sample (not in the free volume), is analogous to atomic entropy. This quantity is accessible experimentally and is often used in conjunction with ϕ to plot density-density phase diagrams. In fact Gibbs in [3] while introducing

a "molar volume-entropy" phase diagram (where the molar volume is defined as $v_{\rm m} = \rho^{-1}$, so he could have equivalently used ρ or ϕ instead) says that it "presents certain characteristics which entitle it to a somewhat detailed consideration, and for some purposes give it a substantial advantage over any other method." The particular purpose he considers is the equilibrium of heterogeneous substances.

The full effect of the size ratio ξ will be pursued in the next section so here I restrict myself to mentioning that for any size ratio, it is possible to obtain a second minimum in the fluid free energy and hence a critical point. However, as the added polymer becomes smaller, the amount of polymer which is required increases rapidly and the density difference between the two coexisting phases increases.

Phase Diagram

The phase diagram can be calculated by considering the common tangents between gas, liquid and solid phases over a large range of polymer chemical potentials, at a fixed size ratio. The equilibrium phase (or phases) will be that (or those) with the lowest free energy, and other possible common tangents indicate metastable equilibria. Metastable boundaries play a crucial rôle in phase ordering kinetics, but do not alter the equilibrium state. [23, 24]

In Figures 2.8(a,b) theoretical free energies are plotted for two colloid-polymer mixtures, with size ratios $\xi = 0.08$ and 0.37. The value of the polymer concentration in the free volume (in normalised units to give an effective polymer coil volume fraction, see page 52) is 0.35 and 0.43 respectively. The common tangents are shown by a thin solid line between the phases in equilibrium coexistence and by a dashed line between phases in metastable coexistence.

In Figures 2.8(c,d) the phase diagrams constructed by varying the polymer concentration over a suitable range are plotted in the density-field (ϕ-$c_{\rm p}^{(\rm free)}$) representation. The relationship between the free energy profiles and the phase behaviour at that particular value of the $c_{\rm p}^{(\rm free)}$ are indicated by the vertical lines. Coexisting phases have the same value of $c_{\rm p}^{(\rm free)}$ so would be connected by horizontal tie-lines. From Figure 2.8(c) we can see that the addition of "small" ($\xi \lesssim 0.2$) polymer widens the coexistence gap between crystal and fluid. If sufficient polymer is added, the fluid branch of the free energy develops two minima, indicating a critical point which enables a distinction between gas and liquid to be made. Although this behaviour is metastable it has been observed experimentally [25, 26] and interferes with the kinetics of phase separation.

For the "large" polymer case ($\xi \gtrsim 0.3$) the critical point is stable and we expect equilibrium three phase coexistence, as in atomic substances between a gas, a liquid and a solid. This has been confirmed experimentally.

Experiments using colloid-polymer systems where ξ can be gradually altered have

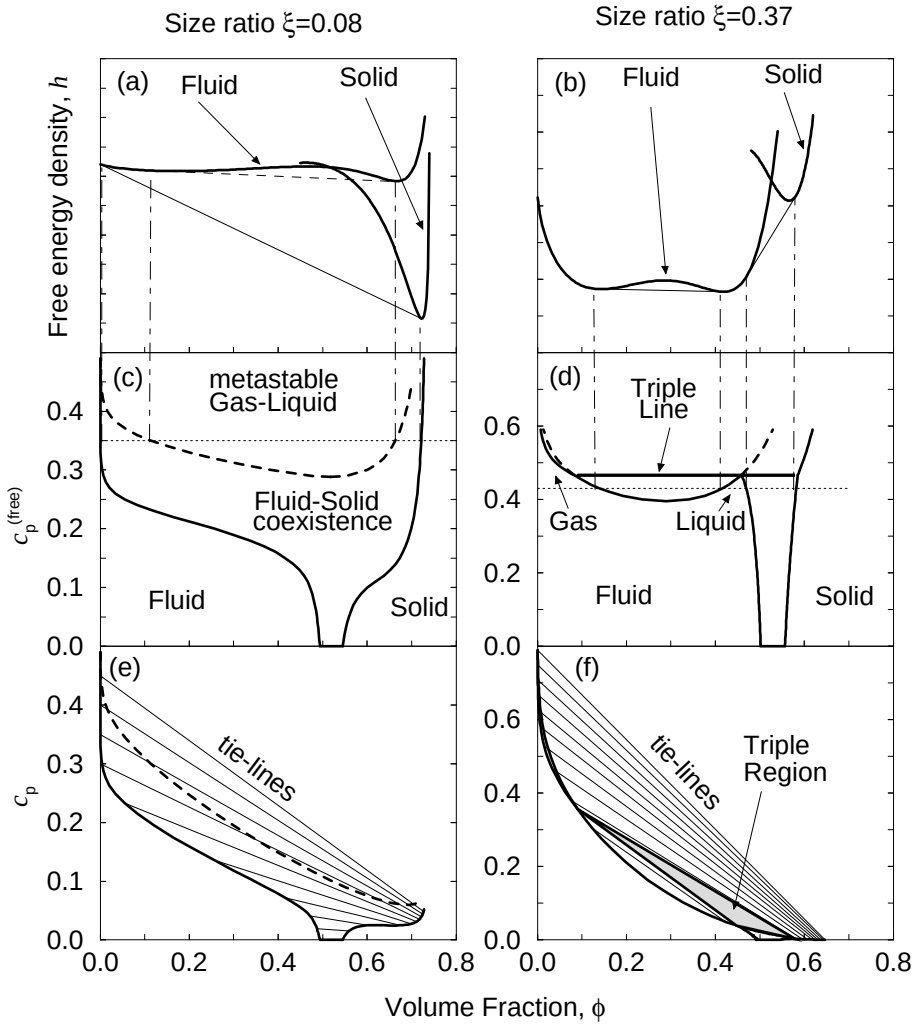

Figure 2.8: Free energies and phase diagrams for colloid with small and large polymer. See text for an explanation.

enabled estimates to be made of the size ratio where the critical behaviour first becomes stable. This is known as the cross over value , ξ_{co} . Currently there is an unresolved discrepancy between theoretical predictions ($\xi_{\mathrm{co}} \approx 1/3$) and experimental observations ($\xi_{\mathrm{co}} \approx 1/4$) for the precise value at cross over. Only for $\xi > \xi_{\mathrm{co}}$ is the liquid state seen. This is an example of how colloidal science has provided insights into the behaviour of atomic systems, in which it is impossible to alter the range of the inter-particle attraction.

The lower two phase diagrams, Figures 2.8(e,f), show the same phase diagrams plotted on the more usual experimental axes using two density variables. As polymer partitioning can occur between the colloid-rich and colloid-poor phases, the tie-lines in this representation are no longer horizontal. In Figure 2.8(f) we observe that the three phase coexistence is now represented by a triangular region, indicating that the gas, liquid and solid differ in their compositions with respect to both colloid and polymer concentrations.

Gelation

Besides the equilibrium and meta-stable behaviour already described, another scenario is often observed in colloid-polymer mixtures. When large amounts of polymer are added, the system rapidly forms a gel: the particles are stuck together by the very deep depletion potential and form fractal or self similar (i.e. they look similar at all magnifications) branches, which span the system and arrest any other motion. After a significant period of time, the gel will break and sediment rapidly, until a dense amorphous sediment has developed at the bottom of the sample, above which is a clear supernatant. See the literature for more detail of this fascinating, and presently poorly understood, side of colloidal physics. [27,28]

Chapter 3

Concepts of Polydispersity

3.1 Introduction

3.1.1 Polydispersity: A fact of life

Complex fluids, are so called because they are more intricate than simple molecular fluids. The complexity essentially arises from the presence of one or more mesoscopic components dispersed in a simple fluid. With such a broad definition it is not difficult to appreciate how complex fluids appear in many guises in daily life: products from shampoo to salad dressing, and from paint to petroleum all fall into this category. In practically all complex fluids, except those of biological origin, the properties of individual mesoscopic components are not identical. For example, size, shape, composition, charge or densities may vary. In other words complex fluids are generally *polydisperse*. Consider the simplest system in which the variation of properties in the mesoscopic component can be described by a single parameter ε. The distribution of ε can be described by a normalised distribution function $f(\varepsilon)$. The polydispersity σ is defined to be the standard deviation of this distribution divided by the mean value:

$$\sigma = \sqrt{\frac{\langle \varepsilon^2 \rangle}{\langle \varepsilon \rangle^2} - 1}, \tag{3.1}$$

where the nth moment $\langle \varepsilon^n \rangle$ is defined in the usual way as

$$\langle \varepsilon^n \rangle = \int_{-\infty}^{+\infty} \varepsilon^n \, f(\varepsilon) \mathrm{d}\varepsilon. \tag{3.2}$$

Perhaps the most ubiquitous (and therefore important) kind of single parameter polydispersity, and that with which I am predominantly concerned, is size polydispersity, described by the normalised particle size distribution, $f_{\mathrm{psd}}(R)$. The

fraction of particles with radii between R and $R+\mathrm{d}R$ is given by $f_{\mathrm{psd}}(R)\mathrm{d}R$. The normalisation condition requires that

$$\int_{R=0}^{R=\infty} f_{\mathrm{psd}}(R)\mathrm{d}R = 1, \tag{3.3}$$

although there is nearly always a sensible maximum radius. The measurement of $f_{\mathrm{psd}}(R)$ in a real system is non-trivial. Most experimental techniques used to measure particle sizes cannot access the entire distribution, but actually measure a small number if its moments, where the n-th moment is defined as in Equation 3.2 above.

The effect of polydispersity (in size, charge, etc.) on complex fluid behaviour has been the subject of research for some time. In this thesis we focus on polydispersity effects on phase behaviour.

3.1.2 Gibbs Phase Rule

Gibbs determined a simple rule which tells us the maximum number of phases which can coexist in a given system. This so called Gibbs Phase Rule can be proved by counting variables in the coexistence equations relating the independent variables in a given system. [2, 3]

Consider a single-component system, characterised by the thermodynamic variables pressure P, volume V and temperature T. At equilibrium, the chemical potential μ and temperature T of two coexisting phases must be equal. Mechanical equilibrium also requires equal pressures in the two phases. Denoting coexisting phases by Roman superscripts and writing μ as a function of P and T we can write this as

$$\mu^{\mathrm{I}}(P,T) = \mu^{\mathrm{II}}(P,T). \tag{3.4}$$

The solution of this equation is where the two planes $\mu(P,T)$ intersect, and is, in general, a line of points given by $P(T)$, the coexistence curve. For three coexisting phases, the solution is the intersection of three planes, and occurs only at one point, the triple point $(P_{\mathrm{t}}, T_{\mathrm{t}})$. That there is only one solution is a consequence of the two unknowns (P and T) being completely specified by the two equations ($\mu^{\mathrm{I}} = \mu^{\mathrm{II}}$ and $\mu^{\mathrm{I}} = \mu^{\mathrm{III}}$, or equivalently $\mu^{\mathrm{II}} = \mu^{\mathrm{III}}$). This argument also shows that the maximum number of coexisting phases in a one component system is three.

Note that the monodisperse hard sphere system is a special case, because here μ is a function of P but not T. The solution of the two phase coexistence problem is a matter of finding the intersection of the two lines $\mu^{\mathrm{I}}(P) = \mu^{\mathrm{II}}(P)$ which occurs at one particular value of P, where hard-sphere crystal and fluid are in coexistence. Three-phase coexistence in monodisperse hard spheres is not possible.

This argument can be extended to deal with a mixture of l different species and r coexisting phases. The chemical potentials of each of the l species must be equal in all r coexisting phases. As $r-1$ equations are needed to equate the chemical potentials, we obtain $l(r-1)$ equations. The unknowns for which we are trying to solve are the coexistence temperature and pressure T, P and the (mole) fraction of each species in each phase x_i, where i identifies the species and is between 1 and l. As the sum of the mole fractions must equal one, we can write one of them as a function of the others as $x_l = 1 - \sum_{i=1}^{l-1} x_i$. We find there are $2 + r(l-1)$ unknowns. For a solution to exist we demand there are more unknowns than equations, so that $l(r-1) \leq 2 + r(l-1)$, or $r \leq l + 2$. For a single component system, $l = 1$ and we recover the result found above that there are at most 3 coexisting phases.

In a multi-component hard sphere system, the chemical potential is still only a function of P. The general Gibbs phase rule for such a system is $r \leq l + 1$. The addition of random-coil polymer to an effective single component hard-sphere fluid (in which the effect of the solvent has been integrated out, as discussed in Section 2.3.1) increases l to 2, and we are permitted a maximum of three coexisting phases, which has been observed experimentally. Often, the effect of this added polymer is likened to an "effective temperature". We can use the usual Gibbs rule, except with $l = 1$ and we recover the same result.

In a truly polydisperse system, there are infinitely many species and infinitely many chemical potentials to equate. Therefore, we may expect a plethora of coexisting phases. However, for a continuous distribution, although there are *mathematically* infinitely many species, it is probably unphysical to assign say particles with a radius difference of 1 angstrom out of 500nm as being different species. However, the level on which any histogramming, or coarse-graining should be performed, is unclear. Also, this prediction of Gibbs only places an upper bound on the number of phases which can coexist. More than this number of phases may be possible in a given system, but never in existence at the same time. This argument highlights the potentially exciting (but complicated) situations which could occur in multi-component, or polydisperse systems.

3.2 Graphical Representation

3.2.1 Preface

The results of phase behaviour studies are almost invariably presented in the graphical form of "phase diagrams". The graphical representation of the phase behaviour of a polydisperse system is subtle. Here we give a tutorial review of the subject by discussing in detail the phase behaviour of a minimalist "polydisperse" system–a binary mixture where most of the above-mentioned subtleties of the

truly polydisperse case are already present. Then we move on to consider the use of moment densities and associated graphical representations.

3.2.2 One-Component Phase Diagram

First consider a one-component system. Since only 3 variables p, T and ρ (or its reciprocal, the molar volume v_{m}) are needed to describe a system, its phase behaviour can be *completely* represented by the equilibrium surface. First we review briefly this surface for a monodisperse system containing a gas-liquid transition, Figure 3.1(a), which contains complete information regarding the phase behaviour. A projection along any axis (e.g. P in Figure 3.1(c)) onto the plane formed by the other two axes (T–v_{m}) simplifies the phase diagram, but results in a loss of all information concerning the projection variable. We can restore some of this missing information by including lines of constant pressure (isobars) on the T–v_{m} plot. Such isobars (or isotherms on a T–v_{m} plot) have constant value across the coexistence region.

3.2.3 Two Component Systems

The commonplace mixture of alcohol and water is a good example of a binary mixture, of which we may already have some intuitive grasp. For example as alcohol has a lower boiling point (or conversely a higher vapour pressure) than water, the vapour in equilibrium above a glass of gin and tonic will contain relatively more alcohol than the drink. Distillation of almost pure alcohol from a mixture is only possible because of this phenomenon, known as the *fractionation* of a multi-component mixture. In general it is achieved by exploiting variations in physical or behavioural properties of the different components.

To characterize a two component mixture consisting of substances A and B, we need to introduce a fourth state variable. Here I will use the mole fraction x, which specifies the relative quantity of one of the species. For pure component A, we define $x = 0$ and for pure B, $x = 1$. It is apparent that the phase behaviour is now controlled by the four state variables (p, v_{m}, T, x), so *any* graphical representation (in two or three dimensions) is necessarily a projection. Here we will limit the discussion to the case of a mixture of two substances (such as alcohol and water), which in the fluid state mix in any proportion. Ignoring any solid phases, we only expect to see two phases, a gas and a liquid.

The p–T Projection

We can project the equilibrium surface along both v_{m} and x onto the p–T plane. The $x = 0$ and the $x = 1$ curves are trivially obtained: they are the vapour

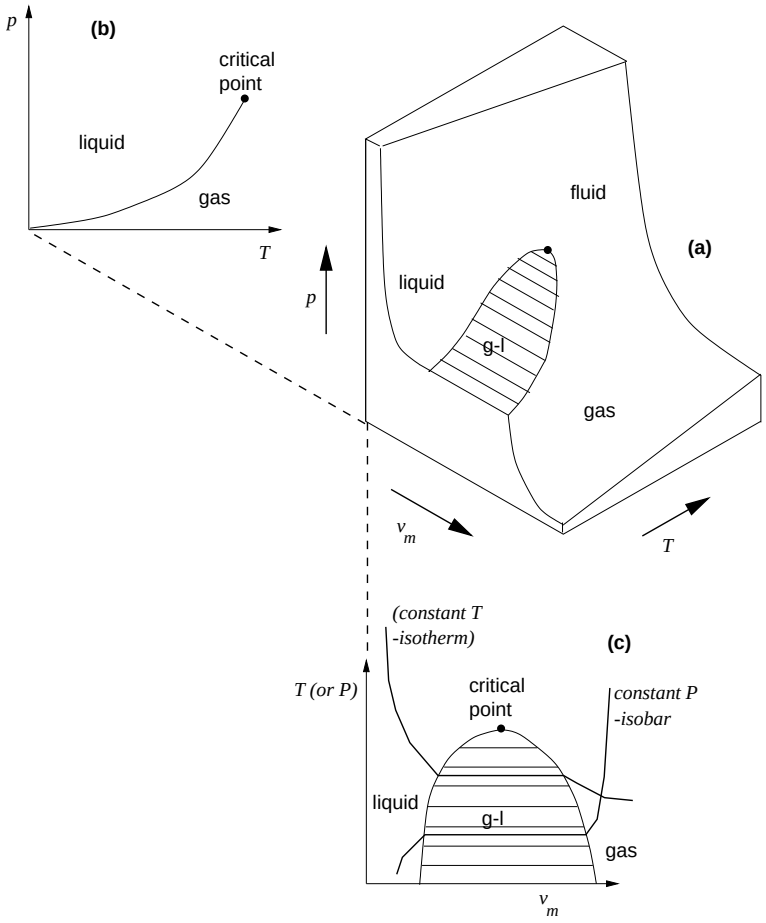

Figure 3.1: (a) The p–$v_{\rm m}$–T surface showing gas, liquid and coexistence regions. (b) The projection onto the p–T plane in which the coexistence region becomes a line.(c) Projection along p (or T) onto the T–$v_{\rm m}$ (or p–$v_{\rm m}$) plane. Isobars (isotherms) can be projected to recover lost p (T) information.

pressure curves for pure A and B respectively and are plotted in Figure 3.2(b). As the curve for A ($x = 0$) is above that for B, we know that A has a higher vapour pressure at a given temperature, or conversely, a lower boiling point at a fixed pressure (and corresponds to the alcohol in the example earlier). The two pure substance critical points are connected by a line of critical points corresponding to a mixed component critical fluid. The region of gas-liquid coexistence has expanded from the single vapour pressure curve to the region between the two curves. To understand more clearly what happens in this region we can look at cross-sections taken at constant p.

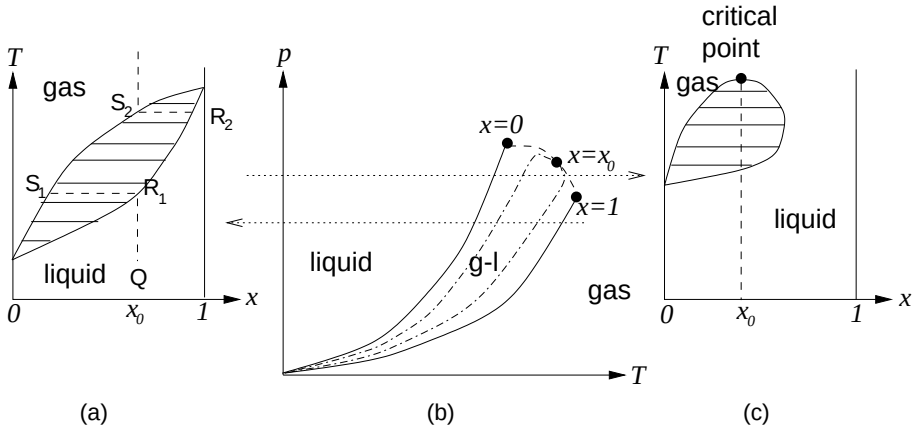

Figure 3.2: (b) Projection of the equilibrium surface on the p–T plane for a two component system. The two pure substance critical points are connected by a line of critical points for $0 \leq x \leq 1$. In the region between the two vapour pressure curves, gas-liquid coexistence occurs. The dashed-dotted lines enclose the coexistence region for some value of $x = x_0$ between 0 and 1 and also contain a critical point. (a) Cross-section at constant p below both critical points. (c) Slice at p between the critical points of the two pure species for which the mixed system at x_0 is critical.

At pressures below both critical points, we see a cigar shaped coexistence region, bounded above by the *condensation point curve* and below by the *boiling point curve*, as illustrated in Figure 3.2(a). Below the boiling point, the equilibrium state is a liquid and above the condensation point it is a gas. On heating a liquid initially at Q to point R_1, a gas with composition S_1 boils off. This gas contains more of component A (alcohol) than the liquid. On continued heating the compositions of both phases alter, the liquid phase following the curve R_1R_2 and the gas S_1S_2. At the condensation point only an infinitessimal amount of B-rich (water-rich) liquid remains. This then boils off leaving a gas with the same composition as the initial liquid at Q.

At the critical pressure of the pure B component, the condensation point curve is normal to the $x = 1$ curve, and this indicates a critical point at $x = 1$. On increasing the pressure further, the "cigar" disconnects from the $x = 1$ line and the critical point moves to smaller values of $x = x_0$, as illustrated in Figure 3.2(c). By projecting these points onto the p–T plane we obtain the line of critical points,

which terminates at the pure phase A critical point.

As experiments are nearly always performed at a constant overall composition, it may seem appropriate to take cross-sections at a given value of x. However, in such a two dimensional picture, we would lose all information regarding the variation of x in the coexisting phases. Nevertheless in Figure 3.2 the dash-dotted curve sketched between the $x = 1$ and the $x = 0$ curves shows the coexistence region for a composition given by x_0. As opposed to the single species behaviour of constant pressure across the coexistence region, indicated by the flat isobar in Figure 3.1(c), this binary system permits a range of p values at coexistence at a given temperature.

The T–v_{m} Projection

It is also possible to project the equilibrium curve onto the T–v_{m} plane as in Figure3.1(c). The coexistence curves for $x = 0$ and $x = 1$ are the pure component curves. These will differ from each other in both critical temperature and molar volume (or density), but will share the general form of the coexistence curve in Figure 3.1(c). The curves for intermediate values of x pose more difficulties, but by tackling these problems, we will gain deeper understanding of multi-component phase separation. As mentioned in the previous section, in a binary system the pressure at coexistence may vary for a given temperature. This is equivalent to saying that the isobars for the binary system are not horizontal in the coexistence region in a T–v_{m} projection.

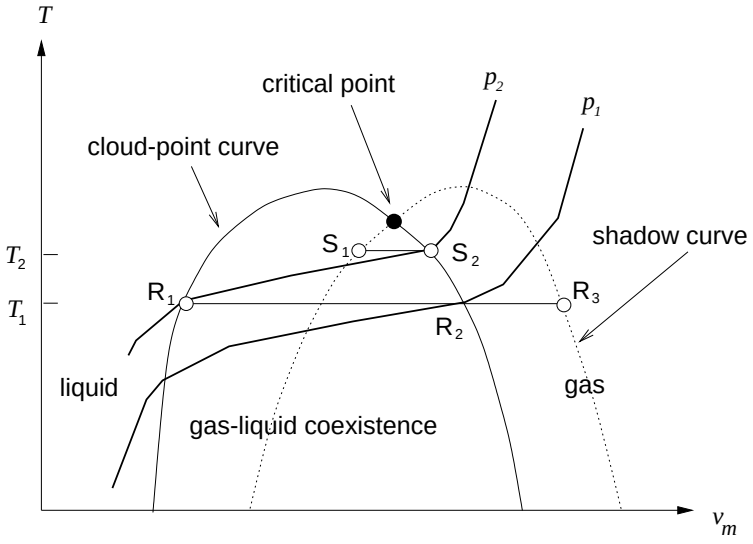

Figure 3.3: Projection onto the T–v_{m} plane. See text for details.

In Figure 3.3 a slice through phase space at an arbitrary composition x_0 is plotted. For reasons which will hopefully become clear, the curve containing gas-liquid states is no longer referred to as the coexistence curve, but instead as the *cloud*

point curve. All points outside this curve, for this particular initial composition ($x = x_0$), are stable states. Typical isobars are plotted for two pressures ($p_2 > p_1$) for this particular slice of x_0, and do not have a constant value throughout the coexistence region. A liquid phase sample at point R_1, with temperature T_1 and pressure p_2 (open circle), is situated on the cloud point curve. This means that it is on the brink of phase separation and is therefore in equilibrium with an infinitessimal amount of a gaseous phase. However, the gaseous phase is *not* given by the other branch of the cloud point curve at the same temperature (point R_2 at T_1, p_1), because this gas phase would have a lower pressure. It therefore appears that there are no possible phase points which satisfy both the equal temperature and pressure constraints. Indeed, in the $x = x_0$ plane there are none, but there will be a point with a different composition ($x \neq x_0$) which satisfies the constraints. When such points are projected onto the $x = x_0$ plane, there is no reason to expect them to overlay the cloud-point curve. All that we demand of the projection of these infinitessimal phases, is that they describe a "sensible" (i.e. smooth and continuous) curve in the $x = x_0$ plane. This curve is commonly called the *shadow curve*. (I'm not sure whether the name comes from the almost ephemeral nature of the phase it describes, or because it is usually drawn as a projection (shadow) on phase diagrams.) For example, the phase indicated by point R_3 could be the projection of the infinitesimal gas phase which coexists with bulk liquid R_1. Likewise, at the higher temperature, T_2, but still at the same pressure p_2, the bulk gas phase S_2 could coexist with the infinitesimal phase S_1. Points R_3 and S_1 both lie on the shadow curve.

Previously we noted that there was a specific critical point for every composition, at which tie-line lengths go to zero and the gas and liquid phase become indistinguishable. This could occur at the top of the cloud point curve, but as tie-lines are out of the plane there is no reason to demand it. In Figure 3.3, the critical point is to the right of the maximum, and occurs when the shadow curve lies in the $x = x_0$ plane and intersects the cloud point curve.

The various points raised in our discussion of the cloud-point and shadow curves for a binary mixture carry over to the case of a mixture with more components, including the truly polydisperse case, provided that we are only interested in the case of two-phase coexistence.

Tielines

Tie-lines connect coexisting phases, and the lines R_1R_3 and S_1S_2 in Figure 3.3 are examples of such tie lines. As the shadow curve does not lie in the $x = x_0$ plane, these are projections onto this plane. To see this we can consider how one would move along a tie-line. Consider a liquid cloud point sample at R_1, in coexistence with an infinitessimal amount of gas phase described by R_3. To move along this tie line, we must add gas phase and subtract liquid phase. However as the composition of these two phases differs, the overall composition of the sample changes, and we must move out of the $x = x_0$ plane.

Coexistence Curves

Experimentally, it is common practice to determine "co-existence curves", by preparing a sample at a given overall density (or molar volume) and composition x and observing the volumes of coexisting phases at different temperatures. The molar volumes of the coexisting gas-liquid phases are determined and plotted as a curve on the T–v_{m} phase diagram. Such curves are coexistence curves, but they are only relevant for one specific value of v_{m}. Two typical coexistence curves are plotted in Figure 3.4, for initial molar volumes indicted by 1 and 2. In fact, it is possible to measure an entire family of these curves for all initial values of v_{m}. The shadow curve can in fact be thought of as the coexistence curve relating to the cloud point curve.

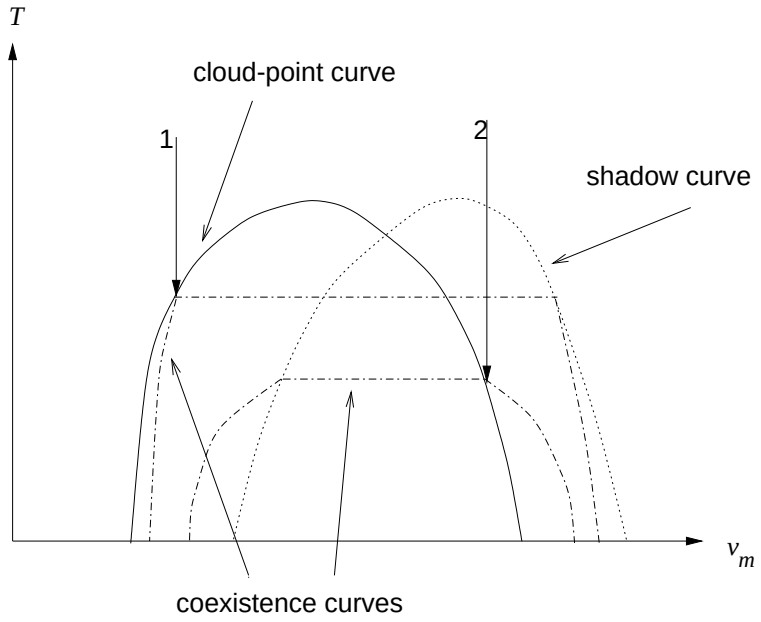

Figure 3.4: Coexistence curves for a polydisperse system are indicated by the dot-dashed curves.

3.2.4 Another Representation using Moment Densities

Other representations of polydisperse phase behaviour are also possible. For example Warren [29] considers the phase diagram of a Flory-Huggins model of a polydisperse polymer system using two moment densities to describe the composition (volume fraction ϕ and number density ρ) and the Flory-Huggins interaction parameter χ (which is often related to temperature T by $\chi = a + b/T$) as the vertical axis. For simplicity, he scales values of ρ by the mean polymer length $\langle L \rangle$ in the parent distribution.

He finds a bubble shaped equilibrium surface in three dimensions, which is represented schematically in Figure 3.5. The horizontal axes are the two relevant

composition parameters (they could be moment densities or individual species densities) and the vertical axis is temperature. The initial composition surface is indicated by the grid and corresponds in this case to a constant average size of the parent distribution (as the volume of a polymer is proportional to its length, $\phi = \langle L \rangle \rho$, the slice is at constant $\langle L \rangle$). The cloud point curve which is given by the intersection of this plane and the coexistence surface, does not lie in the plane of the dashed shadow curve, and they only cross at the critical point.

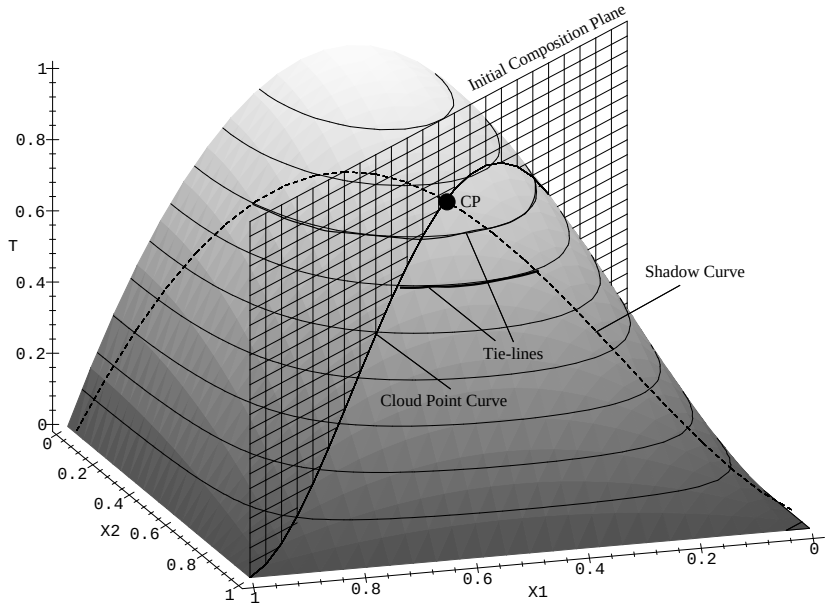

Figure 3.5: Schematic 3D phase diagram for a generic polydisperse system. The horizontal axes ($X1$,$X2$) are either species or moment densities, and the vertical axis is a parameter which controls interaction strengths, typically temperature. The cloud point curve is the intersection between the surface and the initial composition plane. The shadow curve, marked by a dashed line, is evidently not in this plane. Tie-lines run along the isothermic contours.

The use of moment densities of the distribution rather than actual densities of individual components as a means to formulate polydisperse problems has been discussed by Warren [29] and Sollich & Cates [30]. We define the zeroth moment density $\rho^{(0)}$ as the number density $\rho = N/V$, the number of particles per unit volume. Densities of higher moments can then be defined by multiplying the particular moment (defined in Equation 3.2), by the number density, $\rho^{(n)} = \langle R^n \rangle \rho^{(0)}$. The volume fraction ϕ is proportional to the third moment $\phi = 4/3\pi\rho^{(3)}$. If arbitrary moments (say the $\rho^{(m)}$ and $\rho^{(n)}$) are used as axes on a phase diagram, the initial composition plane will correspond to all distributions with equal values of $\langle R^m \rangle / \langle R^n \rangle$.

These moment densities behave like species densities, in that one can define associated chemical potentials and they are also conserved. In other words, when a system separates into coexisting phases, the sum over all phases of any given moment density weighted by the fractional volume of each phase is equal to the initial moment density. In multi-component and truly polydisperse systems, a sufficiently accurate description can often be obtained by using only a few moment densities. This reduces the coexistence equations which must be solved to calculate the phase behaviour from infinitely many species densities to a handful of moment densities. The cost of this approach is that the other moments are not conserved, but annealed (allowed to vary thermodynamically to reach equilibrium), and as a result conservation of particles is not enforced. This is a minor price to pay considering the simplifications to the mathematics and the physical insights gained. In the example formulated by Warren, he solves the problem in terms of the first two moments (ϕ and ρ), and as a consequence there is no partitioning of the second moment (proportional to polydispersity) between the coexisting phases.

Representations of phase behaviour using $\rho^{(n)}$ coordinates are general for *any* type of distribution. In experiments, an initial composition plane has the values of all the moments fixed by the particular stock solution being used. This plane can be represented by a slice through the full phase space. Points on this slice can be made by diluting the stock solution, but those not lying on this plane have a particular moment of their distribution which is either greater or smaller than the parent, depending on which side of the slice they are situated. These points, and the connecting tie lines which cross the initial composition slice, indicate fractionation.

3.2.5 Projection Problems

Cloud point, shadow and coexistence curves can be determined experimentally if a technique for measuring densities *in situ* is available. The cloud point curve can then be plotted exactly as a function of a moment density and temperature in the initial composition plane, but any other curves must be projected onto this plane. The method of projection depends upon experiment as a certain technique will measure a particular moment density: absolute intensity of light, integrated over all solid angles, scattered by a colloidal suspension is proportional to the total volume of the scattering particles, and therefore to the volume fraction $\phi = 4/3\pi\rho^{(3)}$; particles with monodisperse fluorescent cores would have a fluorescence proportional to ρ; particles uniformly coated with a fluorescent polymer would have a fluorescence proportional to $\rho^{(2)}$. Conceivably, other moments could be probed using different techniques.

In Figure 3.6(a) a slice through Warren's phase diagram at a given value of χ (or equivalently T) is shown. Two coexisting phases are indicated by solid circles, one of which lies in the initial composition plane and the other is clearly away

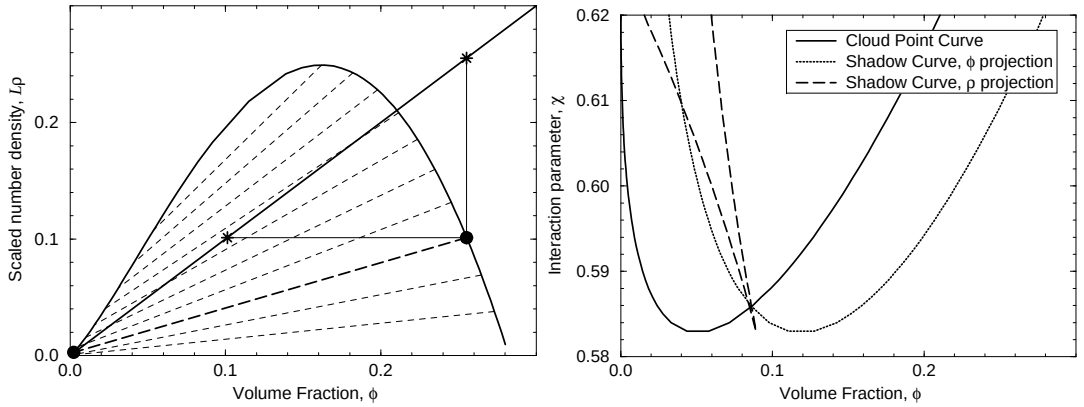

(a) (b)

Figure 3.6: (a) A slice through Warren's phase diagram at constant χ. Two coexisting phases are indicated by solid circles. Projections along ϕ and ρ onto the initial composition plane are indicated by stars ($*$).(b) The resulting shadow curves for these two projections are plotted with the cloud point curve.

from it. This fractionated sample has been projected onto the initial composition plane by two techniques, indicated by stars. The horizontal projection corresponds to a measurement of ρ, and the vertical projection to a measurement of ϕ. Very different looking shadow curves are found, Figure 3.6(b). The somewhat bizarre looking, almost vertical ρ projection of the shadow curve indicates that the emergent, shadow phase has an almost fixed number density, despite having a large range of volume fractions. The multiple crossing points are artifacts of the projection.

3.3 Overview of Previous Work

The use of moment densities greatly simplifies the calculation of phase behaviour and the plotting of phase diagrams. However, other theoretical techniques have also been used. In this section I summarise some of these, and present an overview of some general results for polydisperse systems, followed by some more specific predictions and observations for colloid and/or polymer systems.

3.3.1 Structure of Polydisperse Phases

Much work has been performed to calculate how disordered phases such as dense fluids, are altered by polydispersity. This includes results for radial distribution functions and light scattering measurements, and have been fairly well corroborated experimentally. In this work, I am primarily concerned with how polydispersity alters the phase behaviour not the structure of the equilibrium phases.

Readers interested in this area are directed towards the literature (e.g. [31, 32]) which already exists.

3.3.2 Equilibrium Behaviour in Polydisperse Systems

DeDonder [33], despite being the first to ponder over the polydisperse problem, tackled perhaps the most general situation by considering an infinite number of components, phases and chemical reactions. Aris and Gravalas laid down a rigorous foundation through the use of functional analysis and several other authors then produced results for specific systems. These included results for multi-component hard spheres (scaled particle theory results by Lebowitz and coworkers [18], fluid phase equation of state by Mansoori and coworkers [11] and Dickinson's work on the crystal-fluid transition [34–36]) and polymer systems (for example, by Koningsveld [37]). From these and other efforts Gualtieri and co-workers [38] developed a general framework for calculating polydisperse phase equilibria. Using their formalism they determined cloud point and shadow curves for fluid-fluid equilibrium in a polydisperse van der Waals system, whose behaviour is only dependent on the first two moments of the distribution. (Gualtieri *et al.* assume Schulz distributions.) Their calculated phase diagrams are topologically similar to that presented in Figure 3.3, but their mathematical formalism requires the solution of non-linear simultaneous algebraic equations and offers few insights into the beguiling intricacies of polydisperse systems.

More recently, a universal law of fractionation, applicable to *any* slightly polydisperse system was developed by Evans *et al.* [39], but the experimental verification of this law and further discussion thereof is postponed to Chapter 7 which deals with mixtures of colloids and large polymers.

Few results, other than those already mentioned, have been developed for equilibrium in general polydisperse systems. However, many techniques, spanning theory, computation and, even occasionally, experiments have been used to study specific systems.

3.3.3 Specific Systems

The studies mentioned in this section do not constitute an exhaustive list of work on polydisperse systems. Instead, the intention is more to give a flavour of the field, indicating the main areas of activity, showing where this work fits in and highlighting results which may be of relevance.

Polymers

There is a wealth of literature on polymer polydispersity dating back to the middle of this century when Flory and Huggins [40] proposed a general form for the free energy of a polymer system. Many experiments and calculations since have observed cloud point and shadow curve behaviour and they are well accepted in the polymer literature. For example, Koningsveld in Reference presented many calculated and experimental phase diagrams, Dobashi and co-workers have studied critical phenomenon and exponents [41], Clarke and co-workers [42] have studied mixtures of linear and branched polymers theoretically and experimentally. Of particular importance to this work is the work of Berry [43] who performed very accurate measurements on polystyrene, the polymer used throughout these experimental studies. Berry's main result concerning how the size of polymer coils depends on molecular mass polydispersity is discussed in Chapter 4.

Hard Spheres

Much of the attention on equilibrium polydispersity in the hard-sphere system can be divided into answering two main questions. Firstly, how is the order-disorder (or crystal-fluid) transition affected as the polydispersity of the hard spheres is increased, and secondly whether a sufficiently polydisperse hard sphere fluid can demix to form two coexisting fluid phases, distinguishable not only by density but also by composition. I discuss the first of these questions in great depth in Chapter 5 which is devoted to the experimental study of this phenomenon. The main idea is that above a given size polydispersity, the crystal phase is no longer stable. Debate continues over the value of this "terminal" polydispersity σ_{t} , and the extent of fractionation between coexisting fluid and crystal phases.

The second question has been addressed theoretically by many. Early theoretical work on binary hard spheres found stability over all parameter ranges, but as improved expressions for the fluid free energy became available, predictions for both two component and broad distributions suggested that demixing was possible. See for example References [44–46]. However, at small σ this demixing transition is only metastable with respect to freezing

Schaertl and Sillescu [47] simulated triangular and rectangular distributions of hard spheres, using Brownian dynamics to determine how the random close packed volume fraction ϕ_{rcp} varies with the width of the distributions. Their results, summarised in Table 3.1 show an increase in the maximum packing density at larger polydispersities, as smaller particles can be incorporated into spaces between larger particles.

σ (%)	0	2	5	7.5	10	15	20	25	30	35	40
ϕ_{rcp}	0.64	0.65	0.66	0.66	0.67	0.68	0.68	0.69	0.71	0.74	0.78

Table 3.1: Simulation values for ϕ_{rcp} as a function of σ.

Emulsions

Emulsions are generally very polydisperse. Bibette and collaborators succeeded in purifying a surfactant-stabilised oil in water emulsion through repeated fractionation crystallization [48–50]. They observed separation between a dilute fluid and a disordered but compact phase, which they called a solid phase, induced by the depletion potential due to micelles formed from excess surfactant. The aggregated solid phase was skimmed off, and the process repeated. Visual observations showed that the larger particles were incorporated preferentially into the dense phase, and after four such fractionation steps, the dense solid phase was observed to crystallize. For this to occur, the size polydispersity of the droplets (assumed to be hard spheres) must be less than the terminal polydispersity, $\sigma_{\mathrm{t}} \approx 10\%$. This is evidence for a remarkable fractionation: initially sizes varying from 0.2 to a ~ 3 microns were observed; after fractionation the solid phase contained particles of equal size, to within 10% ($\sim 0.3\mu$m). They offer a heuristic explanation for this observation. Assuming that the many component system can be treated as "a crude superposition of the monodisperse behaviour," they superimpose theoretical phase boundaries for a range of particle sizes. The larger droplets undergo the transition to solid phase more easily (at lower surfactant concentration) than the smaller droplets, so are expected to be enriched in the dense phase.

Depletion Potential

The depletion potential is important in the understanding of many complex fluid systems. In the previous chapter I explained the effect in the situation where large particles are in the presence of many small, monodisperse depletants. Several authors have extended these considerations to multi-component, or polydisperse depletants.

Chu, Nikolov & Wasna [51] and Mao [52] theoretically determined the effect of depletant polydispersity on the form of the depletion potential. They both conclude that the influence of the polydispersity is to slightly weaken the depletion potential. Although Walz [53] predicted that polydispersity would "increase the range and magnitude of the depletion potential", he agrees that the "effect is relatively small ... even for systems with (polydispersity) as large as 25%." When he later performs his calculations by fixing constant the volume fraction of depletants, rather than the slightly unrealistic number density, he also finds that the strength of depletion potential decreases.

Warren [54] and Sear & Frenkel [55] do not explicitly determine the depletion potential, rather they directly calculate the phase diagram for monodisperse hard spheres (colloids) interacting through the presence of depletants (random coil polymers). They both conclude that a system with polydisperse polymers shows an enhanced tendency to separate compared with a reference system containing single sized depletants. Also, both calculations show that the larger polymers are found preferentially in the polymer rich (colloid poor) phase. Presumably, although the depletion potential is reduced, the phase separation is enhanced due to polymer fractionation between the phases: the small polymer is distributed evenly, but the larger coils are found preferentially in the colloid poor phase. Warren noted that if the monodisperse reference system has the same mass averaged molecular weight as the polydisperse system then there is almost no shift in the predicted phase boundaries. He suggested that using this particular moment of the mass distribution function would remove any effect of polydispersity.

Gas-Liquid Equilibrium

Gas-liquid separation can be distinguished from fluid-fluid demixing on a couple of issues. The demixing transition, which is not present in a single sized system, is introduced only by the presence of polydispersity, even if the particles have long-ranged interactions (previously I only mentioned hard-sphere demixing). The two phases are distinguished by composition: fractionation is necessary. In gas-liquid separation, a phase transition is already present in the monodisperse case, and the two phases are distinguished by density. With polydispersity added, the interest lies in seeing how this transition is altered, and whether any fractionation takes place.

Gualtieri *et al.* [38] used their formalism to calculate results for polydisperse gas-liquid equilibrium in a system interacting via a van der Waals potential. Stapleton, Tildesley & Quirke [56] simultaneously simulated, using Monte Carlo techniques, a coexisting gas and liquid phase containing polydisperse particles interacting via the Leonard-Jones potential. They found that the "effect of size polydispersity is to reduce coexisting densities and pressures; the particles in the liquid phase are significantly larger than those in the fluid phase". The inclusion of energy polydispersity (larger particles attracting more strongly) magnifies the effects found for pure size polydispersity. Relating these findings to experimental systems is difficult. They do not impose an initial distribution, but permit particles in coexisting Monte Carlo boxes to change diameters and to swap between boxes, and allow the boxes to alter in volume. The output of this computational technique corresponds neither to cloud point and shadow curves nor to coexistence curves at a given initial density.

Salomons & Mareschal [57] also use Monte Carlo techniques to study liquid-vapour coexistence in binary systems. They are more concerned with the surface tension than with calculating the phase diagram and determining fractionation.

Although Pan & Toxvaerd [58] consider demixing, their molecular dynamics results are more relevant to this gas-liquid discussion. They consider a two component system of van der Waals particles (A and B), distinguished by interaction strengths ("opposites attract, but likes attract even more"). When the two species have the same size, the system demixes into regions of pure A and pure B, separated by crisp interfaces. However, when the particles are unequal in size the interfaces become noticeably fuzzy and the solubility, particularly of the smaller particles in the large-particle rich phase, is high.

3.4 Thoughts on Kinetics

Compared to the equilibrium studies of polydisperse behaviour the study of kinetics in polydisperse systems is very much in its infancy. It presents new, difficult and potentially interesting problems. For example, we can consider two possible routes to equilibrium in a polydisperse system.

In the first situation phase separation occurs, initially with the entire distribution of particles incorporated into both phases. This fast "density equilibration" lowers the free energy to a "constrained", non fractionated minimum. Afterwards, the system realises that by partitioning particles between the phases, the free energy can be reduced to the global, unconstrained minimum. However the equilibration of higher moments will occur on a much slower time-scale, as species incorporated in the depths of the "wrong" phase must extract themselves via long range diffusion. We might expect this type of kinetic behaviour in systems in which polydispersity is not the driving force behind the separation, such as the gas-liquid behaviour considered previously.

In the second case we demand fractionation for phase separation to occur. An example of this is the fluid-fluid demixing transition of hard spheres, or the freezing of binary alloys. This type of separation requires moment equilibration to occur before density equilibration.

In either situation the time to reach thermal equilibrium is expected to be slower than in a single species system and other effects may come into play. In a colloidal system the most obvious extra consideration is that of gravity which may play an increasingly important rôle. Several authors (e.g. [59–61]) have considered the effects of gravity on the settling of a fluid of polydisperse spheres. They all observe a variation of mean particle size with height through the sample.

A still disputed question relating to kinetics in polydisperse systems is whether single sized hard spheres crystallize too quickly to show a glass transition. Experiments are always performed using synthesised particles which are by nature polydisperse, so the question cannot be answered this way. In simulations of hard sphere glasses, polydispersity is often introduced to prevent the spheres from crystallizing. The studies of Moriguchi and co-workers [62] showed evidence

for a glass transition at $\sigma = 0\%$. Also, recent studies in micro-gravity, have shown that quasi-monodisperse particles crystallize above the glass transition, but it is presently unclear whether this occurs heterogeneously (as in normal gravity) or homogeneously. Irrespectively, the subtle interplay between gravity, polydispersity and crystallization remains an interesting topic.

To summarise, using Warren's words [63], "dynamics remains one of the most intriguing problems in polydisperse systems, and the above discussion suggest that at least one of the moment densities (namely the overall density) may become separated from the others in time-scale. It remains to be seen how fruitful a decomposition into moment variables is for understanding the dynamics of polydisperse systems."

Chapter 4

Methods

In this chapter I describe the particular experimental methods which I have used in the rest of the thesis, justify them scientifically, and quantify any associated errors.

4.1 Sample Preparation and Handling

The preparation of a clean, well characterised sample is essential to any experiment. The exact method by which spherical poly-methylmethacrylate (PMMA) colloidal particles are made and then sterically stabilised by chemically-grafting a mono-layer of poly-12-hydroxystearic acid (PHSA) polymer chains is described in the literature [64, 65]. As my work did not involve colloidal synthesis I direct anyone interested in the details of these methods to the references. Therefore this section starts with the assumption that a stock solution has been supplied by an obliging colloid synthesist. Usually the particles as synthesised will be dispersed in an unsuitable solvent, for example, dodecane. This differs greatly in refractive index from PMMA making any visual observations difficult. Samples prepared in dodecane have a bright milky white colour, evidence of multiple Rayleigh scattering (see Section 4.2). The first step of sample preparation is therefore to replace the dodecane with a more suitable solvent; in this work *cis*-decahydronapthalene (or *cis*-decalin for short) and tetrahydronapthalene (tetralin) were used.

To quantify the concentration of particles, I use volume fraction ϕ, which is the volume of colloidal particles per unit volume of sample. In a sample with a distribution of particle sizes (a polydisperse colloid) ϕ is defined by $\phi = \langle V_c \rangle \rho$ where $\langle V_c \rangle$, the average particle volume, is related to the particle radius R by $\langle V_c \rangle = 4/3\pi\overline{R^3}$. The particle number density, $\rho = N_c/V_T$, which is the total number of particles N_c divided by the total sample volume V_T, can also be used. In the case of single-sized (or monodisperse) particles, these two quantities are interchangeable, but for polydisperse systems the situation can become more complex.

For example, two polydisperse samples can have identical number densities but different volume fractions, as the average particle volume can be different in each case.

In the study of colloid-polymer mixtures stock solutions of the appropriate polymers are also required. Careful choice of the polymer stock concentration, $c_\mathrm{p} = m_\mathrm{p}/V_\mathrm{T}$ where m_p is the total mass of polymer added, is required. A sensible stock concentration to work with is one that is not so dilute that excessive amounts are required to reach interesting regions of the phase diagram, but not so concentrated that the solution is too viscous to handle easily. A stock with polymer volume fraction of around one is ideal. (See page 52 for definition of polymer volume fraction.) The polymer I used for this work is commercially available polystyrene, supplied by Polymer Laboratories.

The techniques for preparation are described in more detail below, along with details of measuring heights in samples and the technique I employed to extract coexisting phases from a sample cell.

4.1.1 Colloid Stock Preparation

Washing the Colloid

A stock sample of colloidal PMMA particles suspended in an unsuitable solvent such as dodecane must first be washed. This is performed by centrifuging a sufficient volume of colloid in either a glass or plastic cylindrical cell at approximately 3000 revolutions per minute for about two days. The upper limit to the centrifuge speed is set by the mechanical strength of the cells. The exact time required depends on the size of the colloid particles as can be seen by considering the forces on a spherical particle of radius R_c and density ρ_c suspended in a solvent of density ρ_s and viscosity η (see Figure 4.1).

The gravitational force F_grav downwards on a particle is

$$F_\mathrm{grav} = \frac{4}{3}\pi R_\mathrm{c}^3(\rho_\mathrm{c} - \rho_\mathrm{s})g \tag{4.1}$$

and the viscous drag force for a sedimentation velocity of v_sed in the infinite dilution limit is

$$F_\mathrm{drag} = 6\pi\eta R_\mathrm{c} v_\mathrm{sed}. \tag{4.2}$$

Equating the two forces and solving for v_sed clearly shows the quadratic dependence of the sedimentation velocity on the particle size, (this forms the basis of a method to purify a polydisperse sample, see e.g. [66]):

$$v_\mathrm{sed} = \frac{2R_\mathrm{c}^2(\rho_\mathrm{c} - \rho_\mathrm{s})g}{9\eta}. \tag{4.3}$$

In normal gravity, a 300nm particle in *cis*-decalin will sediment at approximately 1.5mm per day.

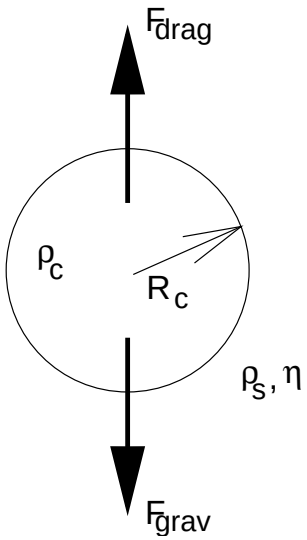

Figure 4.1: Forces on a colloidal sphere.

After two days, most samples will have settled into a dense, random close packed (RCP) structure at the bottom of the sample container and pure solvent above. Initially, this solvent is dodecane. The volume fraction of the RCP sediment is approximately $\phi_{\rm rcp} \gtrsim 0.64$, the exact value being dependent on polydispersity [47] and the (slight) compressibility of the particles. It does not flow when the bottle is tilted, enabling the dodecane to be poured out and replaced by the desired solvent. However, as some dodecane is trapped in the RCP sediment, this procedure, called a wash, is repeated until the desired purity of solvent is reached. The fraction Y of impurity solvent in the total solvent volume after one wash can be calculated if we know $\phi_{\rm rcp}$, and the fraction of the sample which is occupied by the RCP sediment f.

$$Y = \frac{(1-\phi_{\rm rcp})f}{1-\phi_{\rm rcp}f} \tag{4.4}$$

Typically, $\phi_{\rm rcp} \gtrsim 0.64$ and $f \approx 0.5$ giving $Y \approx 0.25$ i.e. one part in four is now dodecane. Each wash will reduce the dodecane concentration by a factor of Y, so the number w of washes required to reduce the amount of the impurity to an acceptable value of around one part in ten thousand can be calculated from

$$Y^w = (0.25)^w = 10^{-4}. \tag{4.5}$$

This gives a value of $w \approx 7$, and so the washing procedure was repeated seven times.

The purity of the solvent which is discarded can be determined by measuring its refractive index (using an Abbe refractometer) and comparing it to the refractive index of the pure solvent. After seven washes the difference of refractive indices is negligible (less than 0.1%) and the solvent is concluded to be sufficiently pure.

Measuring Volume Fraction ϕ

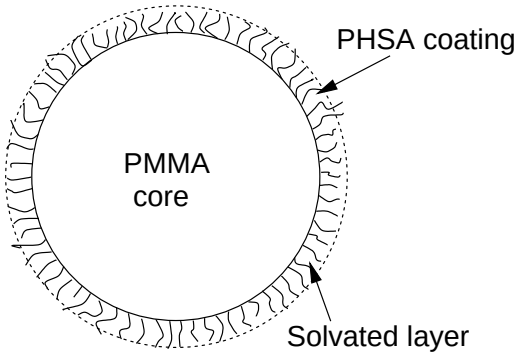

Figure 4.2: Schematic of a core-shell particle. The solid circle indicates the core volume and the dashed line corresponds to an effective hard-sphere volume.

The next step for preparing the colloidal stock is to measure the volume fraction. This can be performed by a variety of techniques, all of which are complicated by requiring at least one assumption about the physical properties of the system. A fundamental difficulty arises when we consider the structure of each colloidal particle: a PMMA core, coated by a thin PHSA polymer brush, as sketched in Figure 4.2. The core is assumed to be impenetrable to *cis*-decalin and tetralin, which are in fact *poor* solvents for PMMA. Conversely, the coating layer extends into the solvent due to the favourable interactions: it is a *good* solvent for PHSA. As it is the steric interactions of these polymer coatings on touching particles which produce the hard-sphere behaviour the overall particle appears larger due to this solvated layer (dotted line in Figure 4.2). The fractional volume occupied by the cores alone, ϕ_{c}, is the easiest to define, but the effective hard sphere volume fraction ϕ_{hs} (or just ϕ) is the more relevant quantity in phase behaviour studies.

The core mass fraction can be easily determined by evaporation of a representative sample of the stock solution. The sample to be calibrated is left in a wide mouthed beaker (to avoid the potentially explosive situation of a film forming across the mouth and then bursting, spraying colloid and solvent everywhere) in a vacuum oven at 50°C until the mass becomes constant (which requires up to 3 days). It is then straightforward to calculate the mass fraction Φ_{M} of the particle cores by dividing the dry mass by the wet mass. We assume that any contributions to the mass of the cores by the collapsed PHSA layer are negligible ($< 1\%$). This mass fraction can be converted into the core volume fraction ϕ_{c} through knowledge of the densities of the core (ρ_{core}) and the solvent (ρ_{s}),

$$\phi_{\mathrm{c}} = \left[1 + \left(\frac{1}{\Phi_M} - 1\right)\left(\frac{\rho_{\mathrm{core}}}{\rho_{\mathrm{s}}}\right)\right]^{-1}. \tag{4.6}$$

Recent experimental work by Martelozzo in Edinburgh [67] has confirmed that the core density of PMMA particles is close to that for bulk PMMA, $\rho_{\mathrm{core}} \approx$

1.18g.cm^{-3}. For the solvent densities, either literature values or experimentally determined values can be used.

To now calculate $\phi_{\rm hs}$, we must include the effect of the solvated layer. Assuming that the extra fractional mass due to this layer is β, then the mass fraction increases to $\Phi_M(1+\beta)$ and it can be shown that

$$\phi_{\rm hs} = \phi = \left(1 + \beta\frac{\rho_{\rm core}}{\rho_{\rm s}}\right)\phi_{\rm c}. \tag{4.7}$$

To eliminate the unknown constant β we must measure the hard-sphere volume fraction ϕ by another method. As it is this parameter which controls the phase behaviour we can use physical properties of the suspension, which depend sensitively on the volume fraction, to determine ϕ.

The obvious first method which can potentially yield the effective hard sphere volume fraction is to assume a particular volume fraction for RCP and measure f, the fraction of a sample which consists of RCP sediment after it has been spun down. The volume fraction of such a sample, obtained by this spinning down technique $\phi_{\rm spin}$ will be given by

$$\phi_{\rm spin} = f\phi_{\rm rcp}. \tag{4.8}$$

The only uncertainty here is the value of $\phi_{\rm rcp}$. For monodisperse particles, it is known that $\phi_{\rm rcp} = 0.64$. The presence of a distribution of particle sizes permits a denser random packing: small spheres can be incorporated into spaces between larger ones. This dependence of $\phi_{\rm rcp}$ on the polydispersity has been investigated in simulations by Schaertl and Sillescu [47] for different size distributions but has never, to my knowledge, been confirmed experimentally. Another source of uncertainty arises because we can never really be certain that the particles are arranged in a random structure. Particularly for samples with very small polydispersities there may well be a tendency for particles to form crystalline regions with volume fractions approaching the theoretical maximum value for packing spheres, $\phi = \pi\sqrt{2}/6 \approx 0.74$. Finally, if the particles were to deform during centrifuging this could also alter the volume fraction of the sediment, although this effect can be allowed for by measuring f over a period of time, thus allowing any compression in the sediment to relax. A final drawback of this method is the inherent inaccuracy involved in measuring f, which is generally known only up to 0.5%. Masses, however, can be measured with much smaller errors ($\approx 0.05\%$).

For monodisperse hard spheres, the most reproducible and accurate method of determining volume fractions is through thermodynamics. From simulations, it is known that there is a volume fraction window between freezing $\phi_{\rm f} = 0.494$ and melting $\phi_{\rm m} = 0.545$ within which a hard-sphere system will separate into a coexisting fluid (at $\phi_{\rm f}$) and crystal (at $\phi_{\rm m}$) (see Section 2.3.3 for more details). Since $\phi_{\rm m} > \phi_{\rm f}$, crystallites settle towards the bottom of a sample cell. By preparing a sample in this region and measuring the relative fraction of sample which has

crystallised (χ) the overall effective hard sphere volume fraction, $\phi_{\rm coex}$, can be calculated from

$$\phi_{\rm coex} = \phi_{\rm f}(1-\chi) + \phi_{\rm m}\chi \tag{4.9}$$

Obtaining χ requires care, because of the effect of gravity. Following Paulin and Ackerson [68], we monitor the heights of the various interfaces in a crystal-fluid coexistence sample over time (see Figures 4.3, 4.4). Extrapolation of the linear portion of the crystal-fluid boundary plot to zero time effectively removes the effects of crystal compression and allows us to recover an accurate measure of χ.

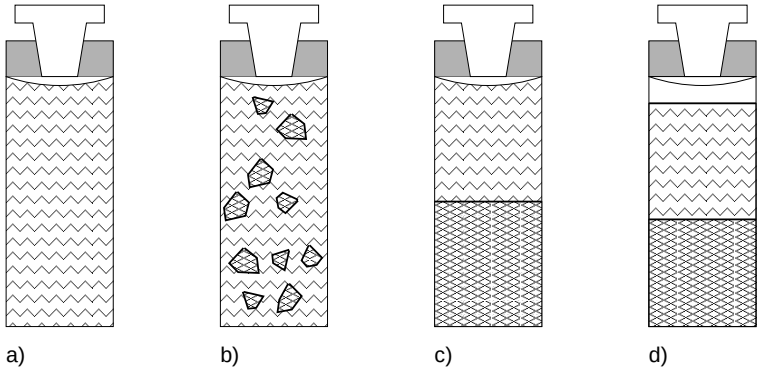

Figure 4.3: Sketch showing crystallisation in a gravitational field. Figure (a) shows a homogeneous colloidal fluid just after cessation of tumbling. After a few ($\gtrsim 2$) hours homogeneously nucleated crystallites are observed throughout the sample, as in Figure (b). After approximately one day the crystallites have sedimented and a clear boundary such as that in Figure (c) is seen between colloidal crystal and fluid. After a week, sedimentation of the fluid phase is first observed around the meniscus, as in Figure (d). The times are approximately those observed for quasi-monodisperse ($\sigma \approx 5\%$) 300nm particles. Higher polydispersity leads to an increase in the time for (b) to occur, the nucleation time. Larger (smaller) particles would behave similarly, over relatively shorter (longer) time-scales.

Using this method on a real sample is first dependent on the assumption that the particles really behave as hard spheres. In addition, the simulation values ($\phi_{\rm m}$ and $\phi_{\rm f}$) were for perfectly monodisperse spheres, which, unfortunately, do not exist in the laboratory. As mentioned in much more detail elsewhere in this work (see chapter on hard-sphere crystallisation), size polydispersity has a significant, but as yet unquantified (or at least disputed) effect on the freezing of hard spheres, and the study of shape polydispersity is still in its infancy. Therefore, for anything other than the most monodisperse spherical colloids ($\sigma < 2\%$, say) it is expected that these values are not appropriate, and additional uncertainty is introduced into the volume fraction calibration. Indeed, for polydispersities greater than a "terminal" value of around 12% crystals do not form at any density rendering this method completely useless. Ignoring these two sources of systematic uncertainties, the statistical uncertainties in χ and $\phi_{\rm coex}$ are related by

$$\Delta\phi_{\rm coex} = \Delta\chi(\phi_m - \phi_f) \approx \frac{\Delta\chi}{20} \tag{4.10}$$

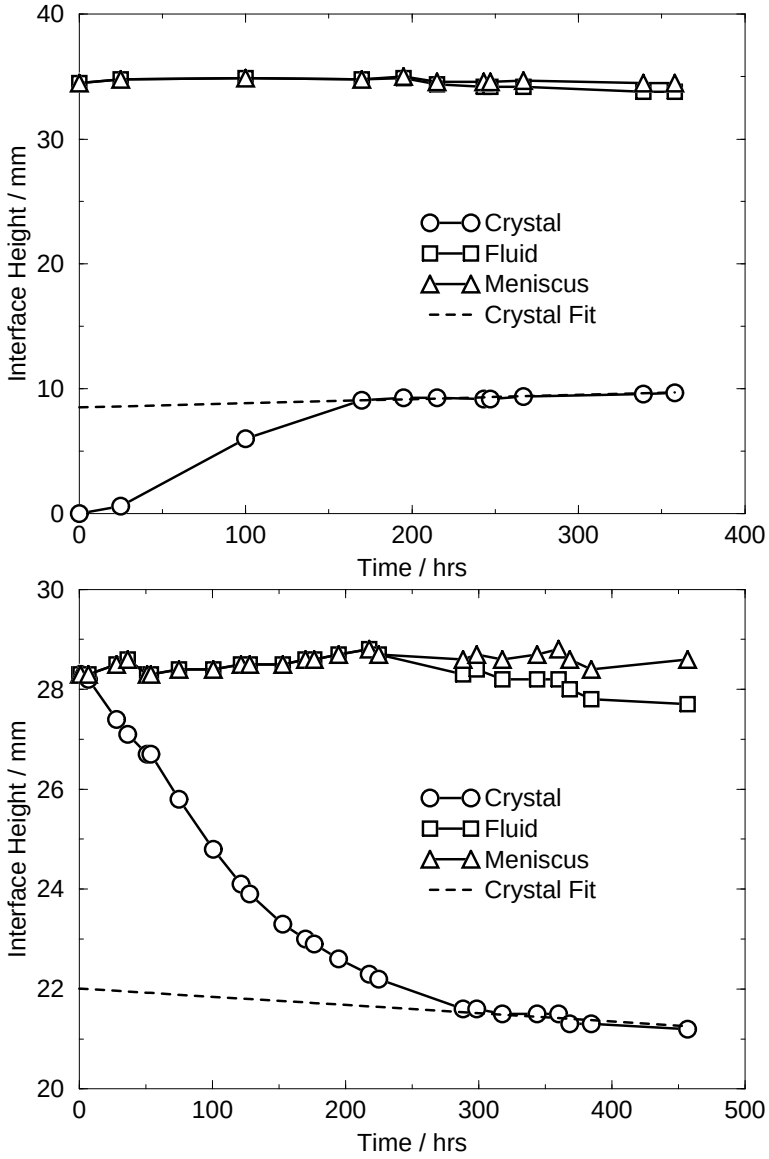

Figure 4.4: Sedimentation profiles for two hard sphere colloidal samples. The extrapolations to zero time of the linear parts of the crystal curves give 25% crystalline for the upper graph and 78% crystal for the lower graph. The volume fractions are 0.507 and 0.534 respectively, and the particles are Batch A, $\bar{R} = 244$nm, $\sigma = 5.2\%$.

Using $\Delta\chi = 5\%$, we find $\Delta\phi_{\text{coex}} = 0.25\%$.

If the particle radius is known, light scattering measurements of crystalline samples can also be used to measure the volume fraction (see Section 4.3.3), but gravitational compression of the crystals can lead to the existence of a density profile through the crystalline phase, which complicates the measurements.

Although it is possible to calibrate a stock volume fraction exactly by this method (without any estimations), when this stock is diluted to prepare a range of samples (either with or without polymer) one must choose values for a few physical parameters. If the particle density is taken as being equal to the core density ($\rho_{\text{core}} = 1.188\text{g.cm}^{-3}$), then an estimation is required for the parameter β. This can be obtained from rearranging Equation 4.7 if both ϕ and ϕ_{c} are known, or by using a previously determined value for a similarly sized system. Alternatively, β can be set equal to one, and the density for effective hard-sphere particles incorporating the solvated layer can be used. These values have been measured by Eldridge and co-workers [69] to vary between 0.979g.cm^{-3} for 186nm radius particles to 1.008g.cm^{-3} for 321nm particles.

The uncertainties associated with these approximations introduce systematic errors in individual sample volume fractions. However, as samples are diluted from the same stock, using the same parameter values, the *relative* uncertainties between individual samples spanning a range of volume fractions, are small, and due only to weighing errors.

Even so, over long time periods, all samples, including the stock solution, are prone to changes in volume fraction via evaporation. To limit this phenomenon, sample cells are sealed with tight-fitting lids, and wrapped with Teflon tape. The masses of samples are then checked periodically to monitor any evaporation. In well-sealed cells, the volume fraction change over a month is much less than 1%, introducing errors in ϕ that are negligible in comparison to other uncertainties. Over longer time scales, mass changes are recorded and contribute to the volume fraction error bars. Other investigators, studying very long time phenomena (years) reduce the effect of evaporation even more by separating the sample from the air by means of a thin layer of a non-volatile liquid such as oil. The cell can then be sealed with a glue or resin.

4.1.2 Polymer Stock Preparation

In comparison to the colloidal system, polymer stock solution is much simpler to prepare and characterise. For the purposes of the work described in this thesis, the two important parameters are the radius of gyration of the polymer and the concentration of the solution.

Determination of Radius of Gyration

The radius of gyration is dictated both by the molecular weight of the polymer, and by the temperature-dependent solvent-polymer interactions. Berry has performed comprehensive studies of the behaviour of polystyrene in *cis*-decalin over a range of temperatures [43] and his relevant results are summarised here. At the theta temperature for a given solvent (which occurs at $T_\theta = 12.4°\mathrm{C}$ for *cis*-decalin) the radius of gyration r_{g}^{θ} (in nm) of a polystyrene coil with molecular mass M (in atomic mass units) is given by

$$r_{\mathrm{g}}^{\theta} = 0.0276\sqrt{M} \tag{4.11}$$

The square root dependence on M in fact defines the theta temperature: at T_θ the monomers behave as ideal points with no excluded volume, so that the coil is described by a simple random walk. Above the theta temperature, the solvent-mediated monomer-monomer interaction is repulsive so that the coil expands. The expanded radius is a function of the interaction (or Fixman) parameter, z, which for linear polystyrene solutions in *cis*-decalin, is given by

$$z = 0.00975\sqrt{M}\left[1 - (T_\theta/T)\right]. \tag{4.12}$$

The expanded radius r_{g} is then given for small values of the Fixman parameter ($z \ll 1$) by

$$r_{\mathrm{g}} = r_{\mathrm{g}}^{\theta}\sqrt{1 + \frac{134}{105}z}, \tag{4.13}$$

or more accurately by reading off the expansion coefficient plotted for $0 < z < 10$ in Figure 12 in reference [43].

The only source of systematic uncertainty in using Berry's data is the polydispersity in the molecular weight, M. The manufacturers quote a ratio of moments to give an idea of the range of polymer sizes. This is usually a weight-averaged molecular mass M_{w} divided by the number-averaged molecular mass M_{n} and is a number greater than 1 ($M_{\mathrm{w}}/M_{\mathrm{n}} = 1$ for monodisperse polymers). Small polymer chains ($M \approx 10^4$) are narrowly distributed, with a typical $M_{\mathrm{w}}/M_{\mathrm{n}} \approx 1.01$. Large polymer chains ($M \approx 10^7$) are more polydisperse, and have $M_{\mathrm{w}}/M_{\mathrm{n}} \approx 1.2$. This ratio can then be used to calculate the polydispersity in molecular weight σ_{M}, by

$$\sigma_{\mathrm{M}}^2 = \frac{\langle M^2\rangle}{\langle M\rangle^2} - 1 = \frac{M_{\mathrm{w}}}{M_{\mathrm{n}}} - 1 \tag{4.14}$$

which leads to a polydispersity in the ideal radius of gyration, $\sigma_{\mathrm{r_g}}^{\theta} = \sigma_{\mathrm{M}}/2$.

Throughout this work, I have used M_{w} in Equations 4.11 and 4.12 to give a weight-averaged r_{g}. Likewise, Berry consistently used M_{w} for the molecular weight, and observed that polystyrene which was "somewhat more polydisperse" than $M_{\mathrm{w}}/M_{\mathrm{n}} = 1.07$ showed an increased in the value of $r_{\mathrm{g}}^{\theta}/\sqrt{M}$ in Equation 4.11 from 0.0276 to 0.0324. As this $\sim 17\%$ increase in polymer size at T_θ was only measured for one (unstated) value of $M_{\mathrm{w}}/M_{\mathrm{n}}$ it is unreasonable to generalise for

other ratios. He also reports that the expansion with temperature was unaffected by polydispersity.

For completeness, I note that it is also possible to measure the radius of gyration using static light scattering by producing what is called a Zimm plot (see e.g. Reference [70]). Related polymer coil parameters can also be measured by dynamic light scattering (see e.g. [71]). I did not use either of these techniques to characterise my polymer samples, as the physics I am trying to understand does not rely on knowing r_g to a great accuracy.

Calculating Polymer Concentration

The polymer mass concentration of a sample is calculated very easily. A known mass of solvent is used to dissolve a known mass of dry polymer (by prolonged tumbling rather than any rigorous stirring which may fragment large M_w polymer molecules). The concentration (in mass per unit volume) of polymer c_p is the mass of polymer divided by the volume of solvent (given by solvent mass divided by the literature value for its density). The polymer coils contribute negligibly (less than 1 %) to the overall stock volume. This absolute concentration can be converted to a polymer volume fraction by division by c^*, the concentration of polymer at "overlap".[†] To make preparation of other samples easier, it is generally recommended to prepare polymer stock with $c_p \approx c^*$

4.1.3 Preparing Colloid-Polymer Mixtures

A simple computer program is used to calculate the required masses of pre-calibrated colloid and polymer stock solutions, and pure solvent in order to create a colloid-polymer mixture with a given colloid volume fraction and polymer concentration. The precision of this technique is limited only by the care with which the experimentalist weighs out the individual components. Uncertainties in initial colloidal volume fraction due to any of the afore-mentioned phenomena (RCP uncertainties, PMMA density, evaporation etc.) only ever result in absolute (or systematic) errors. Relative volume fractions and polymer concentrations in a series of samples are accurate relative to each other to within weighing errors ($\approx 1\%$).

[†] Overlap is defined as the concentration at which the coil volume fraction is of order unity so that individual coils lose their separate identities. The most precise determination of c^* is by quasielastic light scattering spectroscopy to determine when the polymer correlation length begins to decrease as a function of increasing concentration. Here we estimate c^* by using the effective polymer volume fraction $\phi_\mathrm{p} = (4/3)\pi r_\mathrm{g}^3 c_\mathrm{p}(N_\mathrm{A}/M_\mathrm{w})$ (N_A is Avogadro's number) and by equating this to unity giving $c^* = \frac{3M_\mathrm{w}}{4\pi r_\mathrm{g}^3 N_A}$.

4.1.4 Measuring Heights

The bulk of this thesis describes work on two-phase equilibria in colloids. A key measurement in such work is that of the relative volumes of developing phases over a period of time. From these data, phase diagrams can be drawn and initial insights into the kinetics of phase separation can be deduced. For all cases, phase volumes are not measured directly. Instead, due to the density difference between different phases, and the crisp horizontal interface which usually separates them, measuring the height of this interface with respect to time in a sample cell of constant horizontal cross section is equivalent to measuring absolute volumes.

For all such measurements, correct lighting of the interface between phases is essential. Swan-necked lamps, which have optic-fibre arms to deliver focused light without the heat associated with many standard light-sources, are used to illuminate precisely the sample. The height of the interface can be measured using vernier callipers to an accuracy of $\pm$ 0.5mm. For greater accuracy a low power ($\times$40) travelling microscope is used. This is mounted in such a way that vertical displacements are measured on a vernier scale, and results in accuracies of approximately 0.1mm. As sample heights are typically 30mm this is an error of less than 1%. For following sample heights over a long period of time, a video camera with time-lapse recording facility is useful. Relative height measurements can be made after the experiment is complete, directly from the play-back monitor. The drawback of this method is that it is essential to set the illumination correctly beforehand, and as the relevant interfaces are not present initially, this can only really be achieved by trial and error.

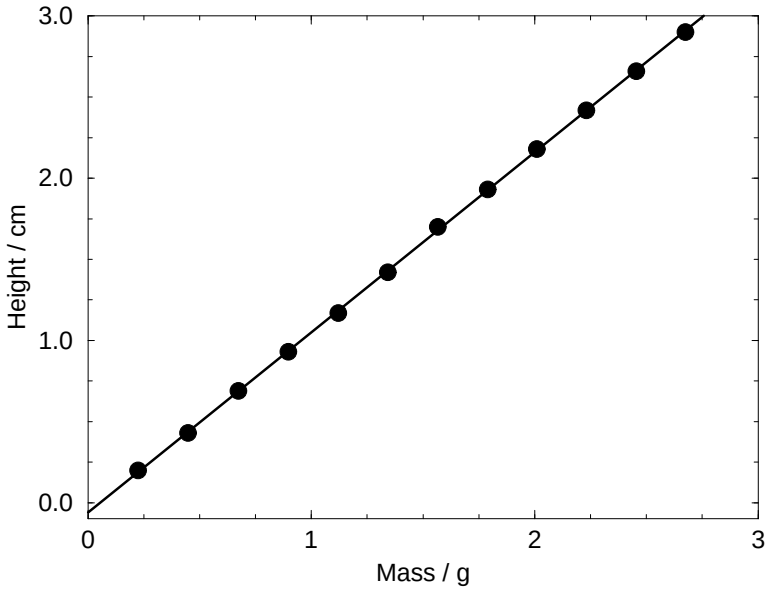

Figure 4.5: Calibration of volume around the meniscus.

To calculate the relative height of a phase, the total sample height must also be measured. Using a pure solvent of known density (*cis*-decalin, ρ=0.891g.cm^{-3}),

I measured the height of the meniscus as a function of the mass of solvent added to a square sample cell with cross-section area of $1cm^2$. The meniscus position was taken to be the lowest point on the interface visible when illuminated from directly behind. By plotting height against mass (see Figure 4.5) the density of the solvent is recovered from the slope of the graph. The volume of extra solvent above the bottom of the meniscus is given by the value of the intercept on the vertical axis. This volume is equivalent to an additional 0.6mm in total sample height, so this value is added to all subsequent meniscus height measurements. The effect of different solvents and the presence of colloids is assumed to be negligible with regards the shape and volume of solvent contained around the meniscus. This assumption is only justified by the observed similarity of menisci in all cases.

4.1.5 Phase Extraction

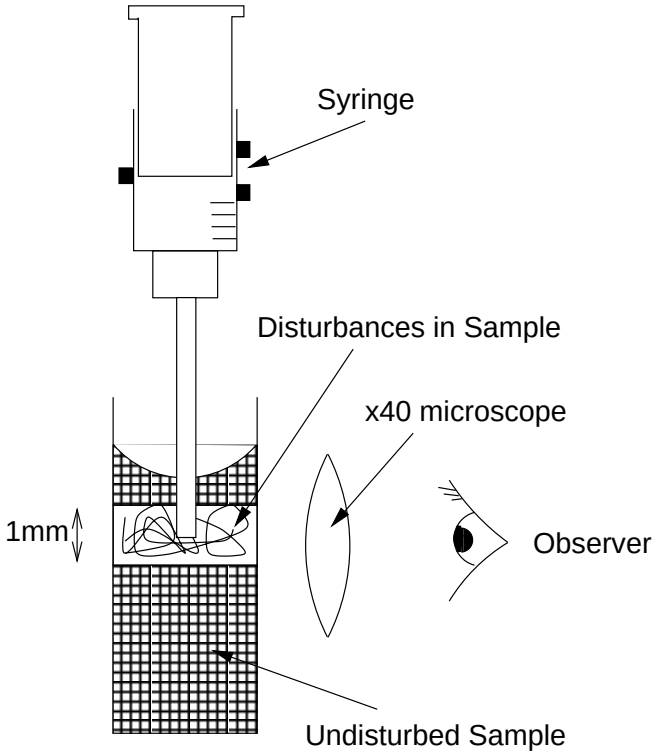

Figure 4.6: Schematic diagram for sample extraction setup.

Extraction of a small volume from a specific region in a sample is a delicate, but essential, procedure for the study of phase equilibria, including fractionation in polydisperse colloids. The method I used throughout this work to remove representative volumes is shown schematically in Figure 4.6. A syringe with a thin, blunt hypodermic needle was held in a retort stand placed on a movable platform. The sample cell was secured directly beneath the tip of the needle and a low-power ($\times 40$) microscope was focused on the sample. The syringe was

slowly lowered to the desired region of the suspension and a sample was removed. Disturbances to adjacent regions were observed through the microscope; with practice these could be limited to approximately a 1mm band around the needle tip. In some circumstances, when the sample was not required for further study, the entire phase was removed, except for a 1mm region close to the boundary. This boundary layer, containing a mixture of particles from both phases, was extracted separately and disposed of.

4.2 Static Light Scattering

4.2.1 Introduction

The scattering of light is behind many natural phenomena, such as the blue colour of the sky, the redness of sunsets and the rings seen around the moon on cloudy nights. The incident light in all these scenarios is scattered as it passes through a medium containing inhomogeneities in optical density (refractive index), such as dust or water droplets. This is because to first order the passage of an electromagnetic wave induces oscillating electric dipoles in the molecules which in turn radiate secondary emission in all directions. In a hypothetical, totally homogeneous medium (without the pervasive density fluctuations), all the light reradiated away from the incident beam undergoes complete destructive spatial averaging, so light only propagates in the initial direction. If the molecules are perfectly ordered, there are distinct directions in which the scattered light constructively interferes (Bragg scattering, see Section 4.3 for the colloidal equivalent). In the presence of non-crystalline inhomogeneities, the destructive spatial averaging is not complete and light is scattered in all directions. The detection and analysis of this scattered radiation, when performed in a controlled manner (e.g. using coherent laser light), is a very widespread and powerful tool for probing properties of mesoscopic systems (which characteristically have length-scales on the order of the wavelength of light).

In all of the techniques, the scattered light provides information in reciprocal, or scattering vector $\mathbf{Q}$, space which must somehow be interpreted to give insights into the behaviour of samples in real space. Information regarding static or averaged properties (individual particle characteristics and structures or arrangements of particles within different phases) can be measured by static light scattering (SLS). In this technique the intensity of scattered light over a range of angles is recorded and analysed. Specifically small angle static light scattering (SALS) is used to probe the structure and growth of large, many-particle objects, such as emergent phases or gels. To investigate particle motions, the fluctuations in the scattered light at a given angle can be measured. This is known as dynamic light scattering (DLS), photon correlation spectroscopy (PCS) or quasi-elastic light scattering (QELS).

SLS is the main analytic probe used throughout this work to characterise particles and phases. The other light scattering techniques were only used in passing and details of the theoretical bases and experimental details can be found in the literature (e.g. Ferri [72] for SALS and Berne and Pecora [73] for DLS.)

4.2.2 Assumptions

To simplify the theoretical analysis of the scattered light it is common practice to make a few assumptions, all of which are justifiable and can be realised experimentally.

- Scattered light is due predominantly to the particles, not to inhomogeneities in the solvent. Any residual solvent scattering can be removed by background subtraction.
- The particles scatter elastically. The shift in frequency on scattering is negligible, so no energy is absorbed by the particles.
- The particles themselves do not distort the incident wavefront. This assumption, known also as the weak scattering limit, leads to the Rayleigh-Gans-Debye (RGD) constraint on the scattering length Q, the particle radius R and the refractive indices n of colloid and solvent respectively, $2QR(\frac{n_c}{n_s} - 1) \ll 1$. In my work, this is enforced by working close to index match (when $n_c \approx n_s$). When this criterion is not met, we must use Mie scattering formulae rather than those for RGD scattering.
- Each photon is scattered at most once. This is the single scattering limit and can be enforced by reducing the refractive index difference , by diluting the suspension (lower volume fraction), or by using a smaller scattering volume. The latter condition can sometimes be obtained by passing the laser near to the edge of a sample and only detecting light scattered close to where the beam enters the cell.
- The scattered light is detected in the far field. We can dispense with the full treatment of Fresnel diffraction and use the Fraunhoffer approximation. This is achieved in practice by use of a lens to collect the scattered radiation.
- The distribution of particles is orientationally isotropic and the system is ergodic. This means there is no preferred direction (e.g. gravity has no influence on the structure) and the system can explore all of phase-space, so a time-averaged measurement of the small scattering volume is equivalent to an ensemble-averaged measurement.
- The particles are orientationally symmetric. If the refractive index profile of a particle is only a function of the distance from the centre of the particle, any scattered light will not depend on the particle's orientation, only its position relative to its neighbours.

- The particles are identical. All particles are assumed to have identical compositions. Variations in particle size are accounted for in the dilute sample analysis but neglected in the crystallography measurements.

4.2.3 The Electric Field

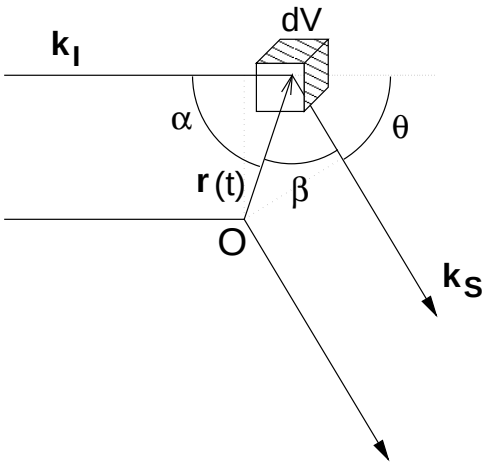

Figure 4.7: The far field scattering geometry. The incident beam (wave-vector $\mathbf{k}_\mathrm{I}$) scatters from volume dV located at $\mathbf{r}(t)$. The scattered beam ($\mathbf{k}_\mathrm{S}$) is detected at angle θ.

To calculate the theoretical intensity as a function of the scattering angle, it is sensible to start by considering the electric field. The geometry for far field scattering is shown in Figure 4.7. Vertically polarised, collimated laser light of *in vacuo* wavelength λ_0, angular frequency ω and electric field strength E_I is incident on a small volume element dV ($\ll \lambda_0^3$) centred at position $\mathbf{r}$ relative to an arbitrary origin. The incident and scattered wave-vectors ($\mathbf{k}_\mathrm{I}$ and $\mathbf{k}_\mathrm{S}$) are of equal magnitude $2\pi n_\mathrm{s}/\lambda_0$ (elastic scattering) and the electric field amplitude at $\mathbf{r}_\mathrm{s}$ is given by

$$dE(r_\mathrm{s}(t)) \propto \frac{E_\mathrm{I}}{|\mathbf{r}_\mathrm{s}|}\frac{(n_\mathrm{c}-n_\mathrm{s})}{\lambda_0^2}e^{-i(\delta\phi-\omega t)}dV, \tag{4.15}$$

where n_c and n_s are the refractive indices of the colloid and the solvent respectively. The phase difference, $\delta\phi$, between the scattered ray and a reference ray passing through the origin is (from Figure 4.7)

$$\begin{aligned}\delta\phi &= \frac{2\pi n_\mathrm{s}}{\lambda_0}(\mathbf{r}_\mathrm{s}(t)\cos\ \alpha + \mathbf{r}_\mathrm{s}(t)\cos\ \beta) \\ &= \mathbf{k}_\mathrm{I}\cdot\mathbf{r}(t) - \mathbf{k}_\mathrm{S}\cdot\mathbf{r}(t) \\ &= -\mathbf{Q}\cdot\mathbf{r}(t).\end{aligned} \tag{4.16}$$

A scattering vector $\mathbf{Q}$ has now been defined:

$$\mathbf{Q} = \mathbf{k}_\mathrm{S} - \mathbf{k}_\mathrm{I}; \tag{4.17}$$

its magnitude Q is given by the simple relation

$$Q = \frac{4\pi n_{\mathrm{s}}}{\lambda_0} \sin\left(\frac{\theta}{2}\right), \tag{4.18}$$

as can be seen from Figure 4.8.

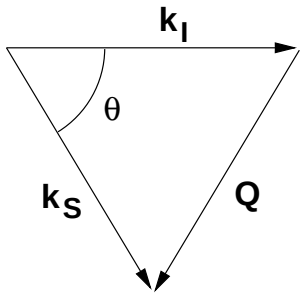

Figure 4.8: The scattering vector $\mathbf{Q}$, given by the difference between the scattered and the incident wave vectors.

For all experimental purposes, due to the sphericity of the particles and the isotropy of the suspension, only the magnitude of the scattering vector is needed. Also, as the terms $\mathbf{E}_{\mathrm{I}}$, $1/\mathbf{r}_{\mathrm{S}}$, $1/\lambda^2$ and $e^{i\omega t}$ in Equation 4.15 are independent of the scattering angle, we will not include them explicitly from now on. So the electric field scattered from the volume dV will be written as

$$dE(\mathbf{r}, \mathbf{Q}, t) = (n_{\mathrm{c}} - n_{\mathrm{s}}) e^{i\mathbf{Q}\cdot\mathbf{r}(t)} dV. \tag{4.19}$$

The calculation of the electric field contribution E_j from spherical particle j of radius R_j, is made easier by rewriting the position of the scattering volume within this particle $\mathbf{r}$ as the location of the centre of the sphere $\mathbf{r_j}$ plus the position of this volume relative to the centre of the sphere, $\mathbf{r}'$:

$$\mathbf{r} = \mathbf{r_j} + \mathbf{r}'. \tag{4.20}$$

The total contribution is now calculated by separating the exponential in Equation 4.19 into an $\mathbf{r_j}$ and an $\mathbf{r}'$ dependent part and integrating $\mathbf{r}'$ over the particle volume, yielding

$$E_j(\mathbf{Q}, t) = b_j(\mathbf{Q}, R_j)\ e^{i\mathbf{Q}\cdot\mathbf{r_j}(t)}, \tag{4.21}$$

where the amplitude $b_j(\mathbf{Q}, R_j)$ of the scattered field by particle j with radius R_j is the integral over the particle volume,

$$b_j(\mathbf{Q}, R_j) = \int_{\mathrm{sphere}} [n_{\mathrm{c}}(r) - n_{\mathrm{s}}]\, e^{i\mathbf{Q}\cdot\mathbf{r}'} dV. \tag{4.22}$$

The total scattering from the N spheres in the scattering volume can then be written as a sum over the contributions from all the individual spheres,

$$E(\mathbf{Q}, t) = \sum_{j=1}^{N} b_j(\mathbf{Q}, R_j)\ e^{i\mathbf{Q}\cdot\mathbf{r_j}(t)}. \tag{4.23}$$

4.2.4 The Scattered Intensity

The quantity measured in an experiment is the time-averaged intensity $\langle I(Q)\rangle$, not the instantaneous field amplitude $E(\mathbf{Q},t)$, but the two are related via

$$\begin{aligned}\langle I(Q)\rangle &= \langle E(\mathbf{Q},t)\ E^*(\mathbf{Q},t)\rangle \\ &= \sum_{j=1}^{N}\sum_{k=1}^{N} b_j(\mathbf{Q},R_j)b_k(\mathbf{Q},R_k)\left\langle e^{i\mathbf{Q}\cdot(\mathbf{r_j}(t)-\mathbf{r_k}(t))}\right\rangle . \end{aligned} \tag{4.24}$$

If the particles are identical, all $b_j(Q,R_j)$'s are equal to $b(Q,R)$ and can be moved outside the summation, allowing us to rewrite the intensity in terms of two useful quantities, the single particle form factor $P(Q,R)$ and the structure factor, $S(Q)$:

$$\langle I(Q)\rangle = N\left|b(0,R)\right|^2 P(Q,R)\ S(Q). \tag{4.25}$$

The normalised form factor is defined as

$$P(Q,R) = \frac{\left|b(Q,R)\right|^2}{\left|b(0,R)\right|^2}, \tag{4.26}$$

and the structure factor is given by

$$S(Q) = \frac{1}{N}\sum_{j=1}^{N}\sum_{k=1}^{N}\left\langle e^{i\mathbf{Q}\cdot(\mathbf{r_j}(t)-\mathbf{r_k}(t))}\right\rangle . \tag{4.27}$$

For very low concentration samples for which the inter-particle correlations are negligible, the $j \neq k$ terms in the product $\mathbf{Q}\cdot(\mathbf{r_j}(t)-\mathbf{r_k}(t))$, are random numbers $\gg 2\pi$ so the average of the exponential is zero. When $j=k$, the average is 1 so $S(Q)=1$ and $I(Q) = N\left|b(0)\right|^2\ P(Q,R)$ for dilute samples. Using this result, the form factor can also be defined as the scattered intensity of a dilute suspension, normalised by the intensity at $Q=0$.

4.2.5 Monodisperse Spherical Form Factors

The form factor of an homogeneous sphere (i.e. $n_c(r) = n_c$) of radius R can be calculated analytically. Integration of Equation 4.22, in spherical polar coordinates, yields

$$b(Q,R) = 4\pi R^3(n_c - n_s)\left(\frac{\sin QR - QR\cos QR}{(QR)^3}\right), \tag{4.28}$$

and the form factor is now only a function of the product QR

$$P(QR) = 9\left(\frac{\sin QR - QR\cos QR}{(QR)^3}\right)^2. \tag{4.29}$$

This is plotted in Figure 4.9. The form factor has minima whenever $QR = \tan QR$, the first few solutions of which occur at $Q_{\min}R = 4.4934, 7.7253, 10.9041, ..., (n+1/2)\pi$.

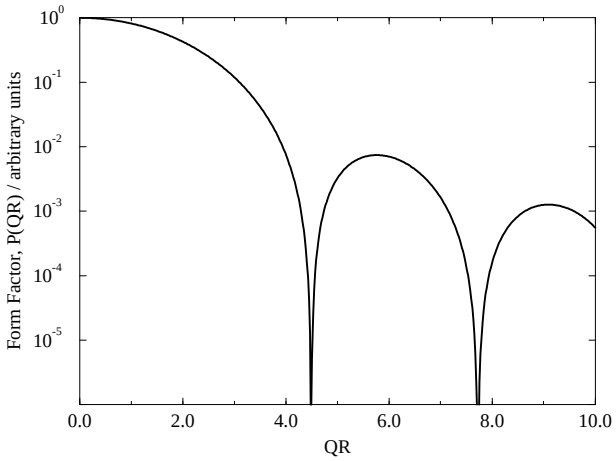

Figure 4.9: Theoretical form factor for a single homogeneous sphere.

Ideally, measurement of such a form factor enables a value for the radius to be calculated from one of two methods. The first is by using $R = 4.4934/Q_{\min}$ and the second involves plotting the data against Q^2 and fitting a straight line close to $Q = 0$. The slope of such a fit is given by a general light scattering result in terms of the radius of gyration $r_{\rm g}$ ($= \sqrt{3/5}R$ for a sphere) of arbitrary shaped scatterers as $-1/3r_{\rm g}^2$. However both of these methods are subject to the complication that for the colloids used in these experiments, the scattering from the PHSA coating is not negligible and the assumption of homogeneity cannot be applied. Although this only introduces a simple step-like refractive index, I consider the more general case for any spherically symmetric particle where the radial variations in the refractive index $\Delta n(r)$ are defined relative to a reference value $n_{\rm c}$, (as sketched in Figure 4.10). Equation 4.28 now acquires a second term containing information about the internal optical structure of the particle,

$$b(Q,R) = 4\pi R^3(n_{\rm c} - n_{\rm s})\left(\frac{\sin QR - QR\cos QR}{(QR)^3}\right) + \frac{4\pi}{Q}\int_0^R r\Delta n(r)\sin Qr\ dr. \tag{4.30}$$

This additional term is independent of the solvent refractive index $n_{\rm s}$. Consequently form factors measured with different values of $n_{\rm s}$ will all have zero first terms and the same non-zero second terms whenever $QR = \tan QR$. Identifying these points, where all such form factors cross and measuring the corresponding value of $Q_{\rm cross}$ gives an accurate value of the optical radius of the particle ($R = 4.4934/Q_{\rm cross}$ for the first crossing point). For Figure 4.11 the solvent refractive index was varied from 1.49 to 1.50 by adding drops of tetralin ($n = 1.54$) and the particle radius determined to be 299nm. For this technique to work, the particle radius and refractive index profile must remain constant in the different solvents over the time-scale of the experiment. Any long-time absorption or swelling will have little effect if the measurements are performed sufficiently

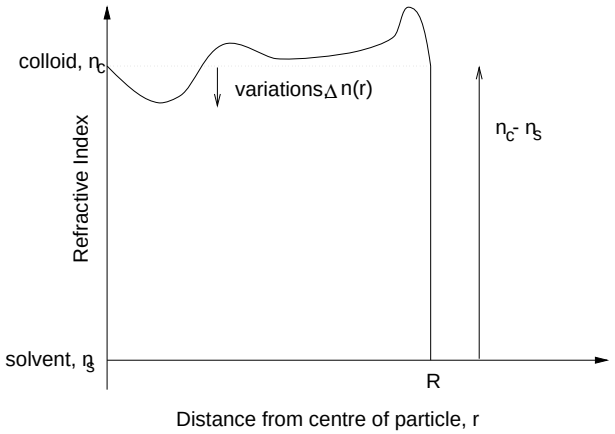

Figure 4.10: Refractive index profile for a radially inhomogeneous sphere.

quickly (over a time scale of a couple of hours)

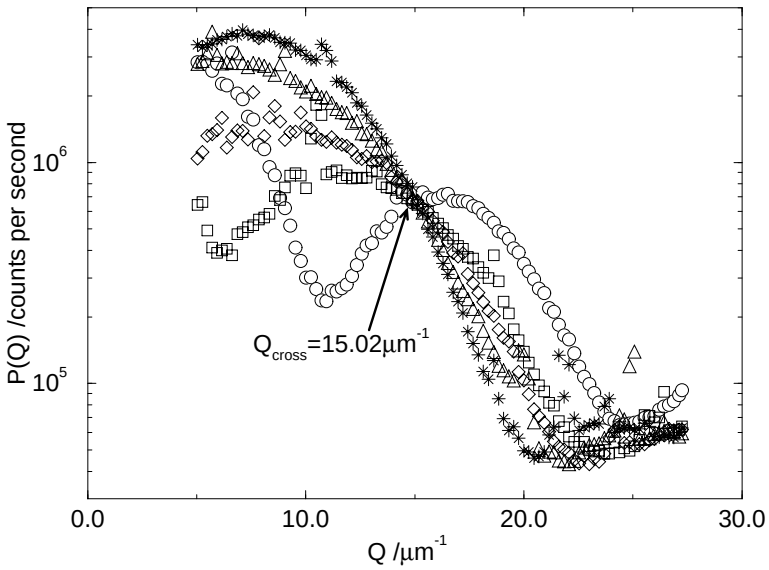

Figure 4.11: Form factors showing crossing point for a sample in which solvent refractive index n_{s} is varied. This procedure enables the radius R_{cross} to be determined to be $4.4934/Q_{\mathrm{cross}} = 299 \pm 2nm$, which agrees with the DLS measurement of R_{DLS}=299nm and the fitted form factor value of $R_{\mathrm{ff}} = 300$nm.

Index Matching

In many situations it is desirable to reduce the probability of a photon being scattered, primarily to ensure that only singly scattered light is observed: multiple scattering causes interpretation difficulties. By making the refractive index of the solvent equal to that of an homogeneous particle ($n_{\mathrm{c}} = n_{\mathrm{s}}$ in Equation 4.29), there is no scattering at any angle as the form factor is always zero. This condition is

referred to as "index matching" and samples prepared in such a solvent appear completely clear at all densities. However, owing to the optical inhomogeneities mentioned in the previous section there will always be some residual scattering from the internal structure of the particles. In this case, the index matching condition can be defined to be when there is no resultant forward scattering i.e. when the two terms in Equation 4.30 cancel at $Q = 0$. Index matching can never be achieved for all wavelengths owing to the slight dependence of refractive index on wavelength (dispersion). In reality, index matched samples appear translucent with a slight yellow tinge, even when $\phi > 50\%$.

To produce an index matching solvent, two or more pure solvents are mixed in a suitable ratio. Assuming that on mixing i components the individual volumes are additive, the combined density ρ is given in terms of the component densities ρ_i and volume fractions $f_i^{(\mathrm{V})}$ by

$$\rho = \sum_{i=1}^{N} \rho_i f_i^{(\mathrm{V})}. \tag{4.31}$$

The refractive index n of such a mixture is given by

$$\left[\frac{n^2-1}{n^2+2}\right] = \frac{4}{3}\pi N_{\mathrm{A}} \rho \sum_{i=1}^{N} \frac{f_i^{(\mathrm{M})} \alpha_i}{M_i}, \tag{4.32}$$

where ρ is the density of the mixture and $f_i^{(\mathrm{M})}$, α_i and M_i are the mass fraction, polarisability and molar mass of the respective components. For the solvents I used (*cis*-decalin and tetralin) these equations can be written (exactly) as

$$\rho = \rho_{\mathrm{cd}} f_{\mathrm{cd}}^{(\mathrm{V})} + \rho_{\mathrm{tet}} f_{\mathrm{tet}}^{(\mathrm{V})} \tag{4.33}$$

and (to within less than 1%) as

$$n = n_{\mathrm{cd}} f_{\mathrm{cd}}^{(\mathrm{V})} + n_{\mathrm{tet}} f_{\mathrm{tet}}^{(\mathrm{V})} \tag{4.34}$$

where the n's, ρ's and $f^{(\mathrm{V})}$'s are the refractive indices, densities and volume fractions of *cis*-decalin and tetralin respectively.

For typical PMMA spheres, $f_{\mathrm{tet}}^{(\mathrm{V})} \approx 1/3$ at index match, giving $\rho = 0.922\mathrm{g.cm}^{-3}$ and $n = 1.500$.

4.2.6 Polydisperse Spherical Form Factors

In any real system, the particles will not be of one size, but polydisperse. To deal with this we relax the monodispersity assumption by permitting a variety of $b_j(Q, R_j)$'s in Equation 4.24 corresponding to scattering from differently sized spheres. In the dilute case we find that all terms in the summation in Equation 4.24 with $j \neq k$ average to zero and the intensity can be rewritten as

$$\langle I(Q) \rangle = \sum_{j=1}^{N} \left| b_j(\mathbf{Q}, R_j) \right|^2. \tag{4.35}$$

Using the definition of the form factor (Equation 4.26) we replace $|b_j(\mathbf{Q}, R_j)|^2$ with $|b_j(0, R_j)|^2 P(QR_j)$ and normalise the intensity with the $Q = 0$ value to get the polydisperse form factor

$$P_{\text{poly}}(Q, \overline{R}) = \frac{1}{N} \sum_{j=1}^{N} \frac{|b_j(0, R_j)|^2}{\left|b(0, \overline{R})\right|^2} P(QR_j). \tag{4.36}$$

By changing from a discrete set of particles to a continuous description, with radii given by the particle size distribution $f(R)$, where $f(R)dR$ particles have radius between R and $R + dR$, the form factor becomes an integral of weighted monodisperse form factors with different radii. The weighting for each size is the appropriate value of f_{psd} multiplied by the square of the relative volume of such a particle,

$$P_{\text{poly}}(Q, \overline{R}) = \frac{1}{N} \int_0^\infty f_{\text{psd}}(R) \left(\frac{R}{\overline{R}}\right)^6 P(QR) dR. \tag{4.37}$$

By effectively summing a range of form factors, the zeros (at e.g. $Q = 4.4934/R$) become "filled in" with scattering from particles of different sizes. The form factors for a 10% polydisperse sample in Figure 4.11 clearly have non zero minima.

Equation 4.37 relates a measurable quantity $P_{\text{poly}}(Q)$ to a property of the particles which we want to know ($f_{\text{psd}}(R)$), however the inversion process is not straightforward. A simple method developed by Pusey and van Megen [74] can be used for samples where the minima are still well defined, otherwise the measured form factor must be fitted by theoretical scattering curves.

Pusey-van Megen Method

If the form factor minima for a given sample are sufficiently well defined then the value of the mean radius and polydispersity can be estimated from the positions and relative depths of these minima. If the value of the form factor at the first minimum is I_{min} and occurs at wave-vector Q_{min} and the secondary maximum has a value of I_{max} then, by expanding an analytic expression for the intensity around the first minimum, Pusey and van Megen find that the polydispersity is

$$\sigma^{-2} = 57.337 \frac{I_{\text{max}}}{I_{\text{min}}} - 15 \tag{4.38}$$

and the mean radius is

$$\overline{R} = 4.4934 \left(1 - \sigma^2\right) / Q_{\text{min}}. \tag{4.39}$$

The expression for the polydispersity becomes meaningless when the maximum and the minimum are no longer distinguishable, i.e. when $I_{\text{max}} \approx I_{\text{min}}$. This naturally restricts this method to systems where the polydispersity is less than

Name	Formula	Radius	Polydispersity
Gaussian	$\sqrt{\frac{1}{2\pi\sigma^2}}exp(\frac{-(R-\overline{R})^2}{2\sigma^2}),\ R=0..\infty$	$\overline{R}$	$\sigma/\overline{R}$
Ramp (R)	$\frac{2}{\Delta R^2}(R-R_0),\ R_0..R_0+\Delta R$	$R_0+2/3\Delta R$	$(\sqrt{2}/6)(\Delta R/\overline{R})$
Ramp (L)	$-\frac{2}{\Delta R^2}(R-R_0),\ R_0-\Delta R..R_0$	$R_0-2/3\Delta R$	$(\sqrt{2}/6)(\Delta R/\overline{R})$
Schulz	$\frac{\alpha^{m+1}R^m e^{-\alpha R}}{\Gamma(m+1)},\ 0..\infty$	$(m+1)/\alpha$	$\sqrt{1/(m+1)}$
Mirror Schulz	$\frac{\alpha^{m+1}(2\overline{R}-R)^m e^{-\alpha(2\overline{R}-R)}}{\Gamma(m+1)},\ 0..2\overline{R}$	$(m+1)/\alpha$	$\sqrt{1/(m+1)}$

Table 4.1: Different forms of the particles size distributions used as fitting functions in Equation 4.37.

$(57.337-15)^{-1/2}\approx 15\%$. However, a more stringent limit to the range of this method's validity comes from an approximation used in its derivation. It is assumed that the distribution is sufficiently narrow so that higher moments of the PSD (such as skewness, the third moment) can be accurately expressed in terms of the polydispersity. In other theoretical works [75] it has been found that for systems with a polydispersity greater than about 5% the values deduced using this method become very sensitive to the exact shape of the distribution, as this assumption becomes invalid.

Fitting Form Factors

Theoretical form factors can be calculated using any chosen PSD and a particle refractive index profile $n_c+\Delta n(r)$. The parameters of such a distribution can then be altered until a good fit between theoretical predictions and experimental measurements is observed. For realistic values of $\Delta n(r)$ and Q and with samples sufficiently far from index match*, the scattering from any inhomogeneities within the particle are negligible compared to the scattering from a homogeneous sphere. For narrow distributions, the extracted parameters (R,σ) do not depend on the type of distribution used. However the form factor for sufficiently polydisperse samples can be fitted well by a selection of distributions with different values of R,σ . With no *a priori* knowledge of the underlying shape of the real distribution as they invariably change from one batch or manufacturing process to the next, it is hard to know what PSD to choose.

The Schulz distribution (see Table 4.1 for definition) is widely used for $f(R)$ in Equation 4.37 when fitting form factors because it is physically sensible: unlike a Gaussian, it has zero probability for negative values of the radius. However, the skewness plays a significant role in the fitting procedure because the weighting by the volume squared of each particle strongly favours larger particles. Any

*For core-shell particles, we can expand Equation 4.30 for small shell thickness ΔR. The restriction for negligible shell scattering becomes $|n_c-n_s|\gg(QR)(Q\Delta R)(\Delta n)$. Substituting relevant parameters for our particles in *cis*-decalin ($|n_c-n_s|\approx 0.01$, $QR\lesssim 6$, $Q\Delta R\lesssim 0.1$, $\Delta n\approx 0.01$), leads to the expression $0.01\gg 0.006$.

distribution which peaks at values above the mean (negatively skewed, such as the Schulz distribution) will have this peak accentuated and will produce a form factor consistent with a narrower distribution with a larger mean. I have experimented using the Schulz distribution and others, including ramps (right angle triangles, either sloping up to the right or to the left) and mirrored Schulz distributions (which skew in the other direction). Table 4.1 lists the equations for these distributions and the range over which they are valid. In Figure 4.12 the theoretical form factors calculated using these distributions are plotted. For values of polydispersity less than 5% there is essentially no difference in form factors (curves not shown). By 9% differences are apparent close to the minima, and at 15% the different distributions give very different theoretical form factors.

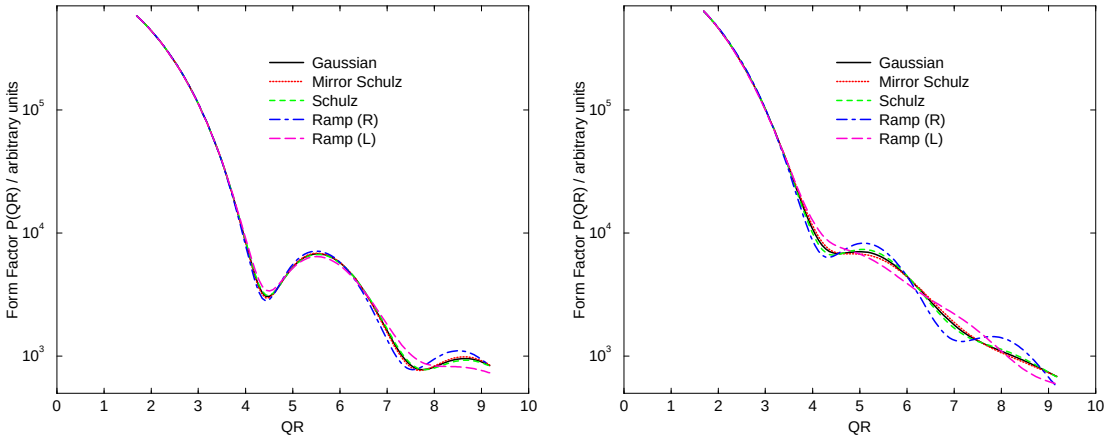

Figure 4.12: Form factors generated by evaluating Equation 4.37 for different particle size distributions, with a fixed mean particle size. At a polydispersity of 9% the differences between curves are noticed near the minima, but for $\sigma = 15\%$ there are marked differences throughout.

Techniques exist which are much less arbitrary than fitting with a particular distribution, and do not prejudice the results with personal bias. Maximum entropy fitting is one example. I used a least squares procedure, which incorporates a Lagrange multiplier for the smoothness of the fit, developed by Glatter [76]. This technique succeeded in reproducing the underlying histogram from theoretical polydisperse form factors constructed assuming homogeneous spheres. When applied to real data, unrealistic fit distributions were generated, even when the effect of the core-shell nature of the particles was included explicitly. However, with additional perseverance, these less subjective techniques should bear fruit.

Ultimately there is no substitute for the painstaking operation of measuring a sufficient number of particles using a transmission electron microscope.

4.2.7 Experimental Considerations

Optical Setup

The experimental setup used for measuring form factors is sketched in Figure 4.13. The glass sample cell is held by a sample holder with three dimensional vernier adjustments and lowered into a solvent bath with refractive index of approximately 1.5 which reduces reflections at glass/solvent interfaces. A collimated Krypton ion laser beam, with wavelength of either $\lambda = 476$nm (blue) or $\lambda = 647$nm (red) is incident on the sample cell and the straight through beam is collected by a beam-stop. The scattered light is focused by a lens onto an adjustable slit. This lens is positioned so that both the sample-lens distance and the lens-slit distance are approximately twice the lens's focal length. This in effect images the slit onto the sample thereby determining the scattering volume. Because of this imaged slit, the volume is a function of the scattering angle, as can be seen in the inset in Figure 4.13. To correct for this, all measured intensities are multiplied by $\sin(\theta)$. The light then proceeds through a pinhole into the photomultiplier tube (PMT). Typically the pinhole has a 500μm diameter which ensures only a few speckles are admitted, and therefore only a narrow Q window is being observed. The photon count is taken over a few seconds which, for dilute samples where the speckles fluctuate many times per second, is sufficient to guarantee a good time average. In systems where the sample can explore all phase space (*ergodic* systems) this time average is equivalent to an ensemble average. The photon count is recorded by a PC, which also controls the angular displacement of the PMT via a goniometer to within 0.1°. Neutral density filters can be inserted into the optical path before the bath or after the slit to ensure the scattered intensity is inside the linear regime of the PMT (see next section on PMT dead time).

The apparatus is carefully aligned ensuring that the straight-through beam passes undeviated through the solvent bath and the sample, and continues through the pinhole and into the PMT when set at an angle of 0°. The sample position along the incident beam direction is adjusted so that the intensity of light scattered at 90° is a maximum with respect to these displacements. Any stray reflections present are removed by placing filters within the solvent bath or by rotating the sample cell so possible scratches on the surface are not illuminated.

A background Q-scan of pure solvent is taken prior to measurements. This is compared to previous background readings to confirm the consistency of the alignment and of the laser power. The background is then subtracted from measurements on samples to give the scattered intensity.

PMT Dead Time

Every photomultiplier has an inherent dead time τ_{D}, due to the small, but finite time required for the electron cascade process to cause a measurable current

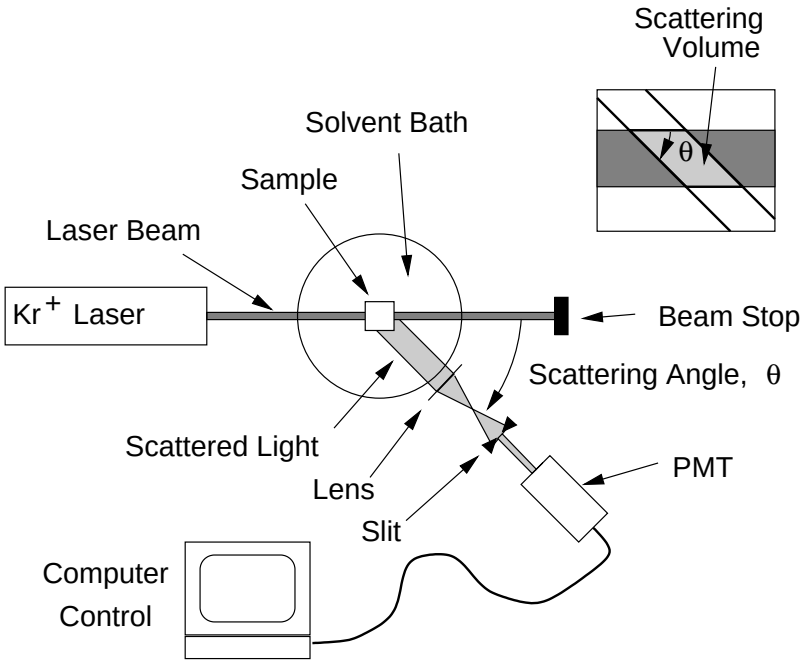

Figure 4.13: Experimental setup for static light scattering. The inset shows how the scattering volume, and hence the intensity, is proportional to $1/\sin(\theta)$.

pulse. If another photon arrives during this time it will not be counted, and the probability of thus missing photons increases with increasing flux: the relation between the real and recorded count rates depends on the statistics of the incident photons. For coherent light, the measured count rate (in photons per second) n is related to the real count n_R by [77]

$$n = \frac{n_R}{1 + n_R \tau_{\mathrm{D}}} + \frac{1}{2}\left[\frac{n_R \tau_{\mathrm{D}}}{1 + n_R \tau_{\mathrm{D}}}\right]^2, \tag{4.40}$$

which permits calculation of the dead time by plotting n as a function of n_R. With a dilute colloidal sample present, n was averaged over thirty seconds by the PMT at an arbitrary fixed angle (67.2°) and the laser power P_{R} (equal to f, an unknown constant, multiplied by n_R) was measured by a power meter located at the beam stop. Figure 4.14 shows n plotted against P_{R}. As f is unknown a second free parameter is introduced to the dead time calibration. However, keeping only terms linear in τ_{D} and rearranging Equation 4.40 reveals that P_{R}/n is a linear function of P_{R}, with slope equal to τ_{D} and an intercept of f:

$$\frac{P_{\mathrm{R}}}{n} = \frac{1}{f} + \tau_{\mathrm{D}} P_{\mathrm{R}}. \tag{4.41}$$

By fitting a straight line through the data (see inset in Figure 4.14) I found $\tau_{\mathrm{D}} = 61 \pm 2$ns, which is equivalent to a saturation intensity of $1/\tau_{\mathrm{D}} \approx$16MHz. All scattered intensities were automatically corrected for this dead time, and neutral density filters were used to ensure the PMT operated well within its linear regime ($n <$ 1MHz).

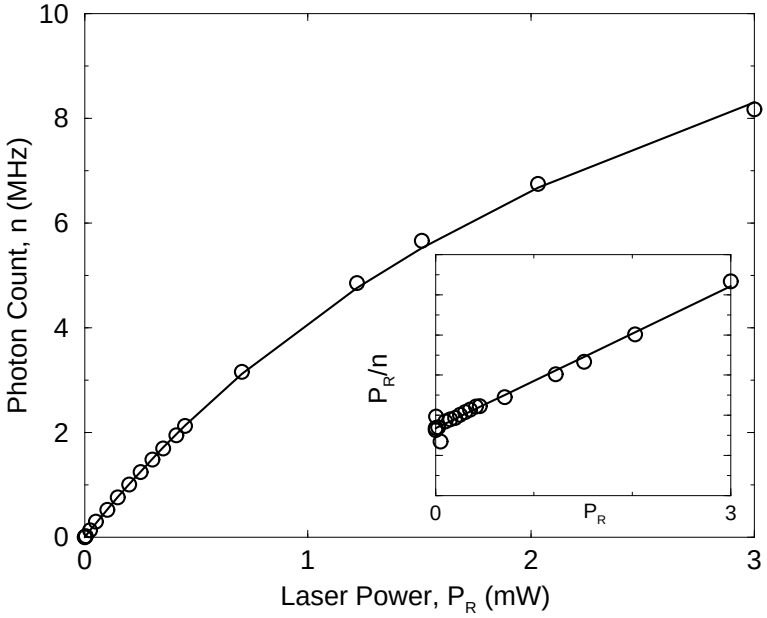

Figure 4.14: Calibrating the PMT dead time. Circles show measured PMT photon count (n) against laser power (P_{R}). The inset shows the same data plotted as the ratio P_{R}/n against P_{R}. The solid line is the straight line fit through all points. The dead time was found to be $\tau_D = 61 \pm 2$ns.

Multiple Scattering

The assumption of singly-scattered light places stringent restrictions on the concentration of samples for which we can measure form factors. The attenuation X, defined as the fractional loss in power of the straight through beam due to the presence of the sample, can be used to quantify the extent of multiple scattering. As no energy is absorbed by the sample, the fraction of incident light scattered must also equal X. If we define q as the probability that a photon scatters once whilst traversing the sample length, then q^2 gives the probability of double scattering, q^3 for triple scattering and so on. We can write X, the total probability of scattering, as

$$X = \sum_{i=1}^{\infty} q^i \tag{4.42}$$

which evaluates to give $X = q/(1-q)$. The fraction of the scattered light which has only done so singly is given by

$$\frac{q}{X} = \frac{1}{1+X}, \tag{4.43}$$

and as X is an experimentally accessible parameter, we can easily quantify the extent of multiple scattering. Effectively, we require negligible reduction in the intensity of the straight through beam ($X \approx 0$) to guarantee insignificant multiple scattering.

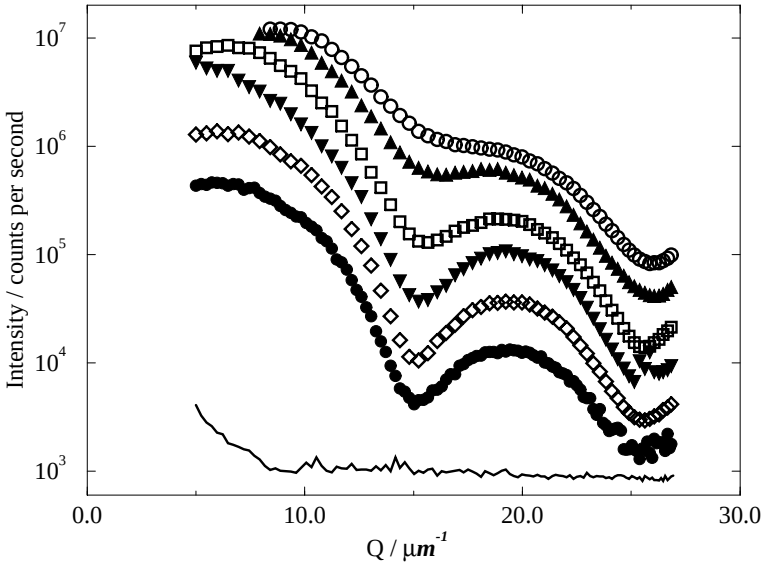

Figure 4.15: The effect of colloidal concentration on the measured form factor. The upper-most curve (empty circles) is the most concentrated sample ($\phi \approx 1\%$), becoming more dilute until the filled circle sample, which is less than one hundredth of this value, and clearly becoming noisy. The solid curve at the very bottom is the background scattering from a sample of pure solvent.

In practice, form factors are taken over a range of dilutions, normally starting at around $\phi \approx 1\%$ and decreasing until the intensity becomes noisy at around the background level ($\phi \approx 0.005\%$), Figure 4.15. The measurement with the deepest minima and a smooth intensity profile is taken to be the required scattered intensity, which is the plot of open diamonds in the figure.

Back Reflections

Often, when attempting to fit experimental form factors, an upturn in the data at large angles is observed, which is inconsistent with any theoretical form factor, as in Figure 4.16. We attribute this effect to scattering from a partially reflected beam. Despite all efforts to reduce reflections, there will always be a diminished beam reflected from the solvent-bath/air interface straight back through the sample. This will be scattered on passing through the sample, and produce a mirror image of the scattering pattern from the incident beam but reduced in intensity. Light initially scattered in the opposite direction to the detector is blocked by neutral density filters positioned in the bath. Mathematically, the light scattered at an angle θ is made up of a forward scattering component $I(\theta)$ and a reflected contribution, $\varrho I(180^\circ - \theta)$, where $\varrho = [(n_2 - n_1)/(n_2 + n_1)]^2$ is the reflectance of the interface between media with refractive indices n_1 and n_2. In terms of Q vectors, this relationship becomes

$$I_{\text{tot}}(Q) = I(Q) + \varrho I(Q^*) \tag{4.44}$$

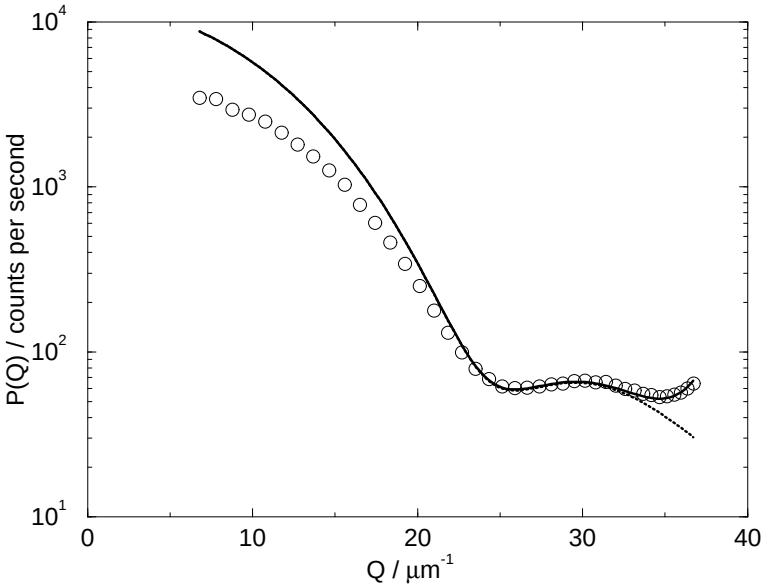

Figure 4.16: The effect of scattered back-reflected light. The circles are the measured form factor, and show the characteristic upturn at high Q. The curve fitted with back-scattering correction (solid line) differs only from the non-corrected curve (dotted line) in this region. The value of the reflectance in this case is $\varrho = 0.0125$, corresponding to $n_1 = 1.0$ and $n_2 = 1.25$. Discrepancies at low Q are presumed to be due to either core-shell scattering or incorrect background subtraction, however investigations produced no satisfactory conclusions.

where Q^* is the Q-vector at angle $\pi - \theta$ and is equal to

$$Q^* = \left[\left(\frac{4\pi n}{\lambda} \right)^2 - Q^2 \right]^{1/2} . \tag{4.45}$$

By introducing such a reflection term in the theoretical form factor an upturn is seen at large angles, due to the bright forward scattered peak of the reflected beam. By judicious adjustment of ϱ between 0 and 0.04 (the theoretical value for a glass/air interface) the calculated upturn can be made consistent with experimental observations.

4.3 Crystallography

4.3.1 Introduction

So far we have only been concerned with observing very dilute samples to characterise the particles. However, once the form factor is known, Equation 4.25 can be used to retrieve an un-normalised structure factor by dividing the total measured intensity by the form factor. In a polydisperse system we can still follow this

prescription to obtain an un-normalised "measured structure factor" [78] defined as the ratio of intensities scattered by a concentrated to a dilute suspension. If we make the (rather crude and unphysical) assumption that there is no correlation between $b_j(Q,R)$'s or $\mathbf{r_j}$'s (equivalent to saying that a particle's size and shape does not alter the structure of the phase in which it is located) then we recover the ideal monodisperse structure factor for a system with the same number density, given by Equation 4.27.† This is rewritten in Equation 4.46 where the two individual particle position vectors have been replaced by the separation vector $\Delta\mathbf{r}_{jk}$. In a crystal, we can make an approximation by dropping the time dependence of this vector; physically this corresponds to ignoring the effects of thermal motions around the mean lattice positions:

$$S^I(Q) = \frac{1}{N}\sum_{j=1}^{N}\sum_{k=1}^{N}\left\langle e^{i\mathbf{Q}\cdot\Delta\mathbf{r}_{jk}}\right\rangle . \tag{4.46}$$

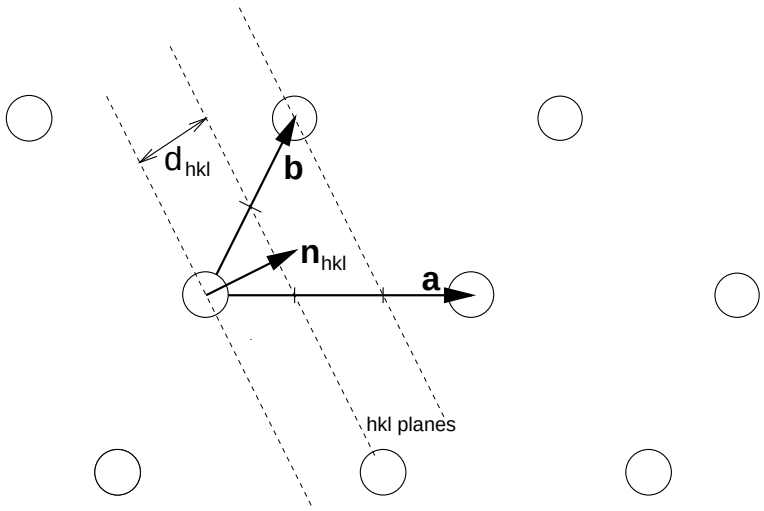

Figure 4.17: Representation of a two-dimensional lattice with primitive translation vectors $\mathbf{a}$ and $\mathbf{b}$. The planes marked are from the set of 320 planes, $\hat{\mathbf{n}}_{hkl}$ is the unit vector normal to this plane and d_{hkl} is the inter-plane separation.

In a crystal, the three lattice vectors are defined such that the sites neighbouring an arbitrary lattice site are at $\mathbf{a}$, $\mathbf{b}$ and $\mathbf{c}$ (Figure 4.17). It follows that the vector $\Delta\mathbf{r}_{jk}$ can only have values made up of linear combinations of these primitive translation vectors. By enforcing that the scattering from all lattice points is constructive (the phase differences $\delta\phi$ defined in Equation 4.16 are all equal to an even number of π's), we find

$$\delta\phi_a = \mathbf{Q}\cdot\mathbf{a} = 2\pi h$$

†In [78] Pusey uses a less dramatic assumption of negligible correlations between scattering amplitudes and positions. He derives an expression for the decoupled structure factor as $S^D(Q) = [1 - X(Q)]\,S^I(Q) + X(Q)$, where $X(Q)$ is a kind of "variance in scattered field amplitudes" averaged over the PSD, $X(Q) = 1 - \overline{b(Q,R)}^2/\overline{b^2(Q,R)}$

$$\delta\phi_b = \mathbf{Q}\cdot\mathbf{b} = 2\pi k$$
$$\delta\phi_c = \mathbf{Q}\cdot\mathbf{c} = 2\pi l \tag{4.47}$$

where h,k and l are integers. These Laue equations place restrictions on the magnitude and direction of $\mathbf{Q}$ at which constructive interference, and hence relative maxima in the intensity (Bragg peaks) are observed. By considering the (hkl) plane which intercepts the primitive vectors at $\mathbf{a}/h, \mathbf{b}/k, \mathbf{c}/l$, Figure 4.17, we arrive at a geometric interpretation of the Laue equations. The inter-plane spacing d_{hkl} is given by projecting the unit vector normal to the (hkl) plane $\hat{\mathbf{n}}_{hkl}$ onto the primitive vectors, divided by the relative hkl parameter:

$$\frac{\hat{\mathbf{n}}_{hkl}\cdot\mathbf{a}}{h} = \frac{\hat{\mathbf{n}}_{hkl}\cdot\mathbf{b}}{k} = \frac{\hat{\mathbf{n}}_{hkl}\cdot\mathbf{c}}{l} = d_{hkl} \tag{4.48}$$

Comparison of Equations 4.47 and 4.48 shows that vectors $\mathbf{Q}$ and $\hat{\mathbf{n}}_{hkl}$ have equal components (to within a constant multiplicative factor) along all three primitive vectors and are therefore parallel. As $\hat{\mathbf{n}}_{hkl}$ is a unit vector, this constant is the magnitude of $\mathbf{Q}$, and they are related by $\mathbf{Q} = Q\ \hat{\mathbf{n}}_{hkl}$. Substituting this into any of the Laue equations (Equation 4.47) gives us the more well known Bragg condition for constructive interference

$$Q = \frac{2\pi}{d_{hkl}} \tag{4.49}$$

from which we can deduce lattice spacings and hence obtain information on crystal structures by measuring the location of Bragg peaks.

4.3.2 Crystal Lattices

In single-sized hard-sphere systems (i.e. not binary mixtures), two simple crystal structures are possible: face centred cubic (FCC) and hexagonal close packed (HCP). These structures only differ in the manner in which the hexagonal planes are stacked on top of each other (Figure 4.18). Consequently, there are Bragg reflections due to the close packed planes, which both crystals have in common, and others which are distinctive *fingerprints* and can be used to identify which structure is present. The lower order reflections are listed by Miller indices in Table 4.2. In the HCP case Miller-Bravais indices are used.[‡] The quantity X is defined in terms of the scattering length Q and the nearest neighbour distance $d_{\mathrm{nn}} = d_{110}$ by

$$X = \frac{1}{2}\left(\frac{Qd_{\mathrm{nn}}}{\pi}\right)^2 \tag{4.50}$$

and is equal to $h^2+k^2+l^2$ in the FCC case and $8(h^2+hk+k^2)/3 + 3l^2/4$ for HCP.

[‡]With Miller-Bravais indices a superfluous fourth lattice vector is used. It lies in the plane spanned by the vectors $\mathbf{a}$ and $\mathbf{b}$ and points at 120° to them. The index which refers to this vector i has value given by $h+k+i=0$ and is inserted after k. Due to the hexagonal symmetry, any cyclic permutation of hki refers to the same plane. This symmetry is not apparent in Miller indices, e.g. planes $12\bar{3}0$ and $\bar{3}120$ are evidently symmetric but 120 and $\bar{3}10$ are not so evident.

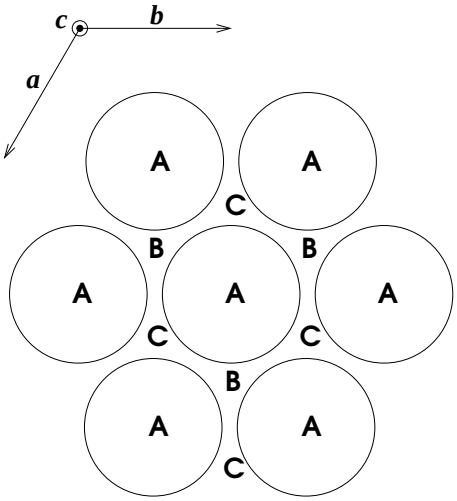

Figure 4.18: Possible stacking positions of hexagonal layers. Both FCC and HCP have the first layer with particles at lattice sites A, and the second layer with particles at B. For HCP the next layer is A and the patern $ABABAB$ repeats. For FCC, the third layer is at position C and continues in the sequence $ABCABC$. The lattice vectors are also shown.

Colloidal crystals are nearly always randomly stacked, so the layer order is neither $ABABA$ nor $ABCABC$. The scattering from such a crystal shows only the lines common to both scattering structures, on top of a diffuse scattering background due to the randomness of the stacking of planes. However, as the structure *ripens* towards a pure state, the peaks unique to that pattern will become evident. For FCC this is usually indicated by the emergence of the 200 peak. Figure 4.19 shows a Bragg pattern for a mixed state taken 10 hours after mixing (dotted line) and the distinctively FCC pattern into which it has ripened, after 10 days (solid line).

4.3.3 Crystal Volume Fractions

Irrespective of whether the structure has been determined, it should be possible to identify all the observed Bragg peaks with a value of X, and usually with a specific hkl reflection. By inversion of Equation 4.50 these values of X can be used to give the inter-particle spacing via

$$d_{\mathrm{nn}} = \frac{\pi}{Q}\sqrt{2X} \tag{4.51}$$

which can be calculated for all peaks to get an average spacing $\bar{d}_{\mathrm{nn}}$. The volume fraction can be found simply by thinking about an FCC crystal with this as the nearest neighbour distance. The FCC unit cell contains a total of four particles, has edge length $\sqrt{2}\bar{d}_{\mathrm{nn}}$, so the volume fraction of the crystal is given by the ratio

FCC	HCP	X
{hkl}	{hkil}	
$\sim$	$10\bar{1}0$	2.6667
111	0002	3.0000
$\sim$	$10\bar{1}1$	3.4167
200	$\sim$	4.0000
$\sim$	$10\bar{1}2$	5.6667
220	$11\bar{2}0$	8.0000
$\sim$	$10\bar{1}3$	9.4167
$\sim$	$20\bar{2}0$	10.6667
311	$11\bar{2}2$	11.0000
222	0004	12.0000

Table 4.2: Bragg reflections in HCP and FCC crystal structures. X is the quantity $1/2(Qd_{\rm nn}/\pi)^2)$.

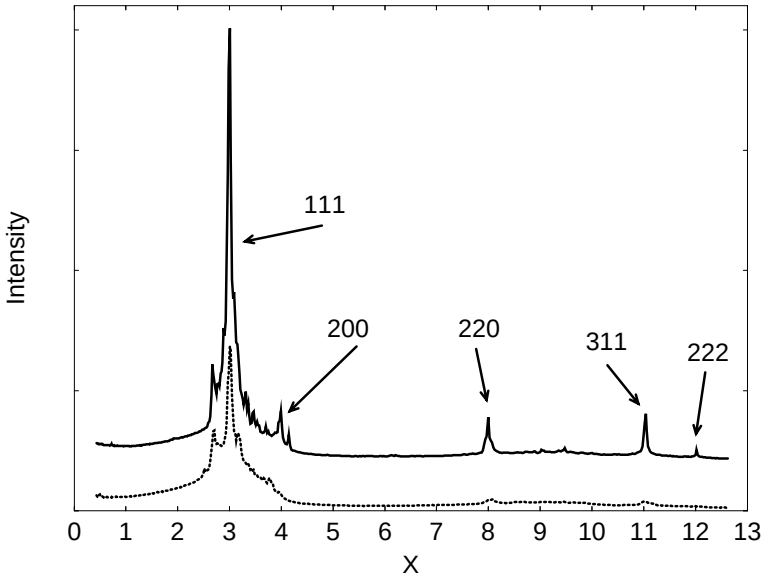

Figure 4.19: Crystallography measurements of intensity against dimensionless quantity X for a coexistence sample of Batch A particles. Crystal volume fraction is assumed to be $\phi = 0.545$, nearest neighbour separation $d_{\rm nn} = 578.6$nm from which the radius is calculated to be 261nm. The dotted curve was taken soon after homogenisation and shows typical Bragg scattering from a crystal in a mixed FCC/HCP state. The solid curve, offset vertically for clarity, was measured 10 days later and shows ripening towards pure FCC structure.

of the colloidal particles' volumes $4V_{\text{part}}$ to that of the unit cell V_{cell} :

$$\phi = \frac{4V_{\text{part}}}{V_{\text{cell}}} = \frac{4\frac{4}{3}\pi r^3}{\left(\sqrt{2}\bar{d}_{\text{nn}}\right)^3} = \frac{16\pi}{3}\left(\frac{r}{\sqrt{2}\bar{d}_{\text{nn}}}\right)^3. \tag{4.52}$$

This relationship can be used to size the particles in a crystal-fluid coexistence sample, in which the crystal volume fraction is assumed to be at the melting value, $\phi = 0.545$.

4.3.4 Optical Setup

The setup used for performing crystallography is similar to that described in Section 4.2.7 and sketched in Figure 4.13, except that an expanded laser beam is used. This illuminates a sufficiently large sample volume containing many randomly orientated crystallites. The focusing lens is removed, the image of the slit is therefore not projected into the sample and we do not need to use the $\sin(\theta)$ correction as the scattering volume does not depend on θ, but is always the entire illuminated volume. A 'diffuser', normally a piece of tracing paper, is inserted just after the slit, to help average out the speckle pattern. By so doing, an average over many frozen speckles (c.f. a powder average in atomic crystallography) is taken: in non-ergodic media such as crystals, we cannot measure a meaningful average temporally.

4.4 Electron Microscopy

With the electron microscope facility we can observe the colloidal particles using electrons as the probe rather than photons. This allows us to see more detail concerning individual particles (see Figure 4.20). However, there is a price to pay, and that is that most current electron microscopes work under vacuum, so the sample has to be dry.

To prepare a sample for transmission electron microscopy (TEM) a few drops of colloidal solution (volume fraction $\phi \approx 0.1\%$) are placed onto a TEM carbon grid and allowed to evaporate. If the original solution is too concentrated, particles will be piled on top of each other, too dilute and not enough particles will be present to ensure decent statistics. In the presence of polymer, the particles tend to aggregate on drying, due to the depletion potential (see Section 2.3.4) which becomes stronger as solvent evaporates and the polymer concentration increases. For this reason more dilute samples are required if polymer is present.

The photographs produced from the TEM facility can be analysed by a variety of image analysis software packages (such as MetaMorph or Optimas) enabling properties of individual particles to be measured and recorded. Complete histograms representative of the real particle size distribution can be compiled from

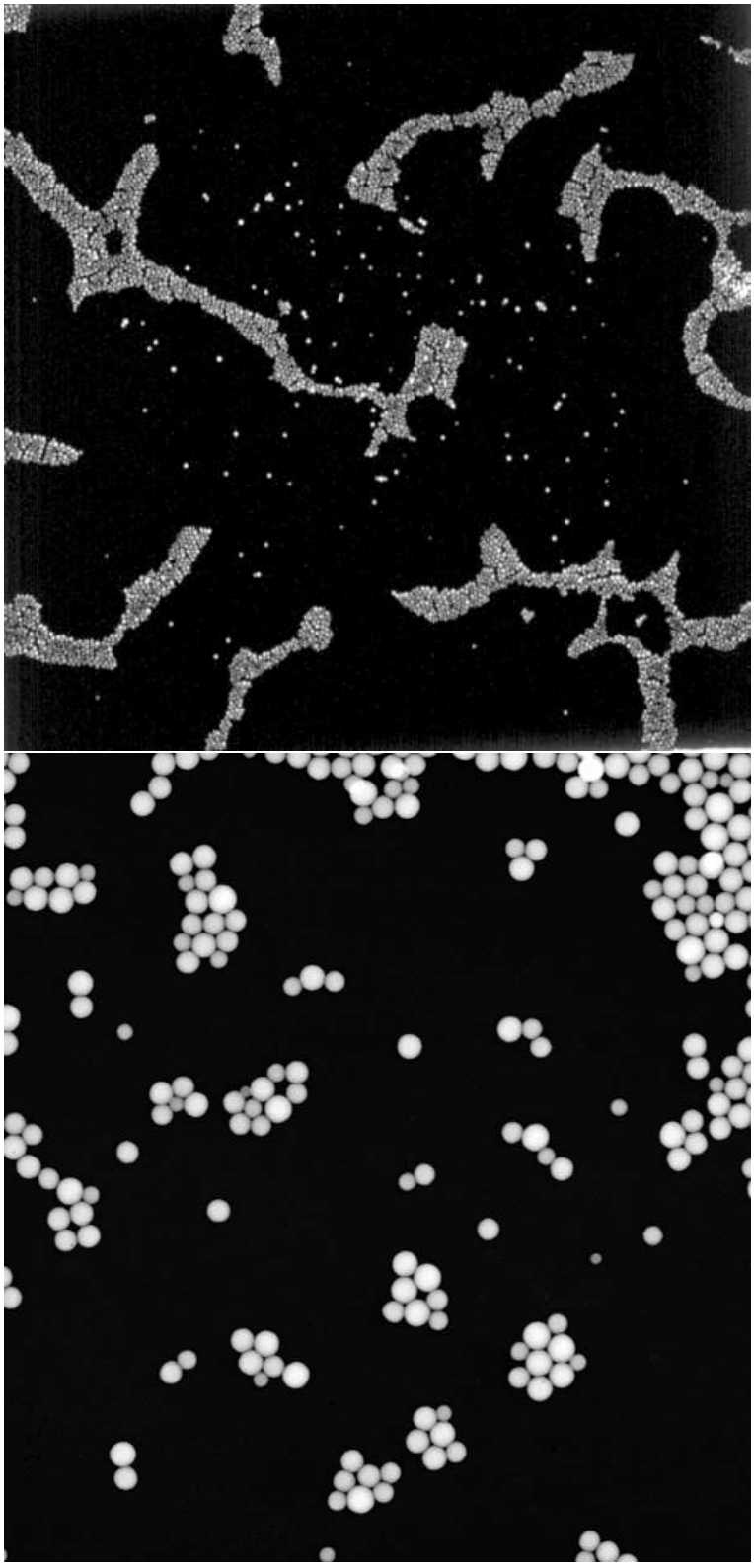

Figure 4.20: TEM photographs. The upper image is at low magnification ($\times 500$) and shows particles clumping together on drying. In the lower image ($\times 3400$) differences in particle size are discernible.

Batch	Fitting $P(Q)$		DLS/TEM		Value Used	
	R(nm)	σ(%)	R(nm)	σ(%)	$\bar{R}$(nm)	$\bar{\sigma}$(%)
A	239 ± 2	6.1 ± 0.3	249 ± 1	4.4 ± 0.4	244 ± 3	5.2 ± 0.6
B			190 ± 3	6.0 ± 0.6	190 ± 3	6.0 ± 0.6
C	294 ± 3	6.7 ± 0.6	312 ± 2	8 ± 0.5	303 ± 6	7.4 ± 0.4
D	300 ± 2	9.2 ± 0.5	299 ± 2	9.8 ± 0.4	300 ± 1	9.5 ± 0.3
E	180 ± 5	13 ± 4	167 ± 1	18.1 ± 0.6	167 ± 2	18.1 ± 0.6

Table 4.3: Summary table for particles used throughout this work. The SLS measurements were fitted with Gaussian distributions. For sample D, the radius was also determined to be 299nm by finding the form factor crossing point over a range of solvent refractive indices.

sufficiently large samples of particles and mean values for any moments of the distribution can be calculated. The uncertainties in the observed mean radius $\Delta_{\overline{R}}$ and in the polydispersity Δ_σ in a sampled distribution decrease with the square root of the number of particles sampled N,

$$\frac{\Delta_{\overline{R}}}{\overline{R}} = \frac{\Delta_\sigma}{\sigma} = \frac{\sigma}{\sqrt{N}}. \tag{4.53}$$

For an uncertainty of less than 1% N must be greater than about 500.

4.5 Characterising the Particles

I used five different batches of particle suspensions throughout these experiments. The average radius and polydispersity of each batch was determined by form factor fitting, and at least one other of form factor crossing points, dynamic light scattering or electron microscopy. The results are summarised in Table 4.3. Particles A and B were 'quasi-monodisperse' and were used as control experiments to confirm our understanding of monodisperse colloidal behaviour. Batches C, D and E are progressively more polydisperse. The differences in mean particle sizes have only a kinetic effect on diffusion and gravitational sedimentation, so general differences in phase behaviour are attributed entirely to polydispersity.

4.5.1 Batch A

Batch A particles were characterised by Moussaïd and Schofield in our group using DLS cumulant analysis. By fitting a theoretical form factor integrated over a Gaussian distribution to the measured form factor, I found $\bar{R} = 239 \pm 2$nm and $\sigma = 6.1 \pm 0.3\%$. Throughout this work I shall quote these particles as having the average of these values: radius $\bar{R} = 244 \pm 3$nm and polydispersity $\bar{\sigma} = 5.2 \pm 0.6\%$.

4.5.2 Batch B

Batch B particles were also characterised by Moussaïd and Schofield using DLS cumulant analysis. The nominal values for Batch B are $\bar{R} = 190 \pm 3$nm and $\bar{\sigma} = 6.0 \pm 0.6\%$

4.5.3 Batch C

As for the previous particles, Batch C was also characterised by Moussaïd and Schofield using DLS cumulant analysis and by myself by fitting Gaussian form factors. The nominal values for batch C are $\bar{R} = 303 \pm 6$nm and $\bar{\sigma} = 7.4 \pm 0.4\%$

4.5.4 Batch D

Batch D particles in both *cis*-decalin and tetralin solvents, were characterised by Moussaïd using DLS to measure diffusion coefficients D (and hence radii from the Einstein relation $D = kT/(6\pi\eta R)$) over a significant Q range. This enables a more accurate value of $\bar{R}$ and σ to be determined than by cumulant analysis [74]. There was no noticeable difference between the radius and polydispersity measurements in the two solvents, so we ignore swelling effects due to tetralin absorption for these particles. As polydispersity in particles is an indicator that there may have been impurities or errors in the manufacturing process (which usually produces particles with $\sigma \approx 5\%$), it is essential to determine whether these mistakes affect the manner in which individual particles behave. For example, one can visualise that an incomplete stabilising coating layer would lead to short range van der Waals attractions and particle aggregation. The DLS characterisation is sensitive to large aggregates, and the measurements were consistent with a non-aggregated system. We conclude that although *something* went wrong in the synthesis of the particles, they can still be treated as hard spheres.

These particles were also characterised by fitting Gaussian form factors and the radius determined by the crossing point technique (Figure 4.11 is the experiment on Batch D particles). All measurements gave similar values. I will use the average values of $\bar{R} = 300 \pm 1$nm and $\bar{\sigma} = 9.5 \pm 0.3\%$.

4.5.5 Batch E

Batch E particles were the most polydisperse ones used. For this reason they were characterised by TEM as well as by SLS. The form factors were fitted to within similar tolerances with a variety of different PSDs. Table 4.4 lists the fit values for different distributions, and the parameters calculated using the Pusey-van Megen method. The strong dependence on the skewness of the chosen fit

Method			Mean Radius $\overline{R}$ (nm)	Polydispersity σ (%)	Skew τ (%)
SLS	Pusey-van Megen		179 ±2	13.4±0.1	N/A
	Fit to PSD	R.Trig	185 ±2	11.0±0.1	9.1
		Schulz	184 ±2	11.8±0.1	7.3
		Gauss	182 ±2	13.0±0.1	0
		M Schulz	180 ±2	13.6±0.1	-8.8
		L.Trig	172 ±2	17.5±0.1	-14.4
Electron Microscopy			167 ±1	18.1±0.6	-15

Table 4.4: Properties of the stock colloid, measured by TEM and SLS, fitted using a variety of PSDs.

distribution is evident.

The results of the TEM analysis of these particles are also present in Table 4.4, and the histogram is presented in Figure 4.21. Although at first it appears that these data are in conflict with the SLS measurements (radii differences of up to 18nm), we can show that this is only an artifact of the SLS data inversion process. By using the measured histogram as the PSD in Equation 4.37 I have generated a 'TEM form factor' which agrees satisfactorily with the measured form factor to within an arbitrary scaling constant (see Figure 4.22). We can conclude that the light scattering and the electron microscopy are in agreement, and that it is only our interpretation of the SLS data which leads to an apparent conflict. This result highlights the difficulties in reliably inverting SLS data to recover information regarding the particle size distribution, and for this reason, the TEM values of $\bar{R} = 167 \pm 1$nm and $\sigma = 18.1 \pm 0.6\%$ are used for batch E throughout this work. Knowledge of the entire histogram, also permits calculation of arbitrary moments of the distribution. These values can only usually be estimated using an expression for higher moments of narrow relatively symmetrical distributions, in terms of the mean and the polydispersity [79]:

$$\overline{R^n} = \bar{R}^n \left[1 + \frac{n(n-1)}{2} \sigma^2 \right] + O(\sigma^3). \tag{4.54}$$

Comparison between the exact and predicted first six moments are presented in Table 4.5. The first two moments are implicitly exact and the next four are all well approximated by the above expression.

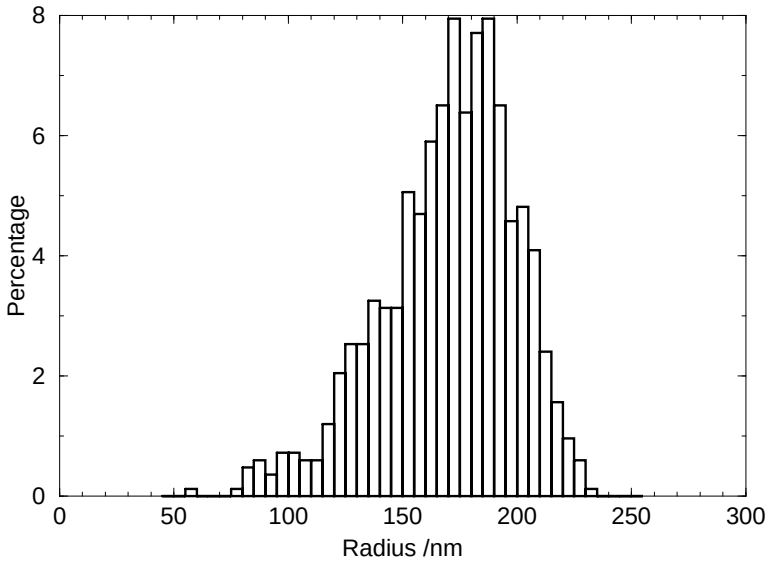

Figure 4.21: Histogram of particle sizes for Batch E, measured by TEM.

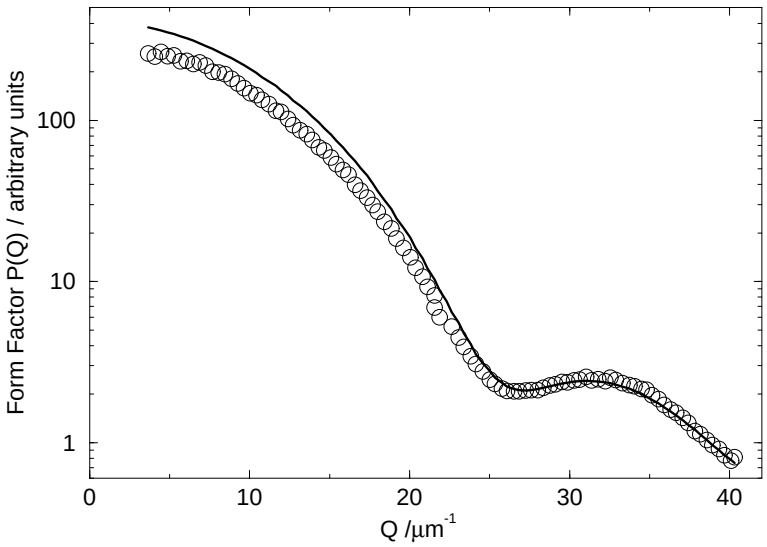

Figure 4.22: Comparison of form factors measured by static light scattering (circles) and reconstructed from TEM measurement of particle sizes (solid line) for Batch E particles. The discrepancies at low Q have been discussed earlier on page 70.

$\langle R^n \rangle$ n	Measured nm	Predicted nm
1	167.48	167.48
2	169.96	169.96
3	172.16	172.35
4	174.14	174.52
5	175.93	176.45
6	177.58	178.13

Table 4.5: Comparison of measured and predicted moments for Batch E particles.

Chapter 5

Observations I: Hard-Sphere Colloids

5.1 Introduction

The hard sphere system represents possibly the simplest interacting thermodynamic system. The particles have no interactions except at contact where there is an infinite repulsion. Although in experimental systems the repulsion can never be infinite, tests on spherical PMMA colloids [80] show that their phase behaviour is in satisfactory agreement with that predicted by simulations of hard spheres [8]. The repulsive interaction, although not infinite, is expected to increase from zero to many $k_{\mathrm{B}}T$ over a distance of 2-3 nm. Despite the extensive work on hard spheres, and the prevalence of polydispersity in real colloids, the few studies which have been performed on polydispersity in hard sphere systems have been restricted to brief observations [78] or kinetic studies [81,82]. However, theoretical and computational predictions have been made and (until recently) seem to agree on one point: there exists a terminal polydispersity σ_{T} above which hard-sphere crystals do not form. Dispute remains over how the system behaves near to this terminal value. In detail, unresolved questions include: does the crystal volume fraction at melting (ϕ_{m}) increase? Does the coexistence gap ($\phi_{\mathrm{m}} - \phi_{\mathrm{f}} = \Delta\phi$) narrow? Is there a re-entrant fluid phase at volume fractions above the stable crystal? Is there substantial fractionation between fluid and crystal phases? Are multiple crystal phases seen?

In this chapter I present details of my experimental studies on polydisperse hard spheres. My findings throw light on some of these issues but also unearth more questions. The experiments I performed were mainly visual observations of colloids with three polydispersities: 5.2%, 7.4% and 9.5%. Crystallographic and fractionation studies were also performed.

5.2 Experimental Procedure

The three colloidal stock solutions used for these experiments were washed and characterised by the methods described in Section 4.5. The mean size and polydispersities were found to be $\bar{R} = 244 \pm 3$nm, $\sigma = 5.2 \pm 0.6\%$ (by SLS fitting and DLS cumulant analysis) for Batch A, $\bar{R} = 303 \pm 6$nm, $\sigma = 7.4 \pm 0.4\%$ (by SLS fitting and DLS cumulant analysis) for Batch C and $\bar{R} = 300 \pm 1$nm, $\sigma = 9.5 \pm 0.3\%$ (by DLS diffusion coefficient measurements, SLS fitting and SLS crossing point measurements) for Batch D. For all cases the quoted radius is from light scattering measurements which, due to the relatively small refractive index difference between the solvated PHSA layer and the bulk solvent, generally underestimates the effective hard-sphere radius. However, to prevent introducing additional errors by estimating the size of the solvated layer, I will use these nominal values as the mean radii of the effective hard spheres.

The first set of experiments, designed to determine differences in phase behaviour between the three samples, was performed by preparing high volume fraction samples and slowly diluting them, observing frequently after each dilution. Three 4cm^3 cuvettes were partly filled with one of each of the stock colloids and index matched by addition of sufficient tetralin. The refractive index of all samples was measured (by centrifuging and then removing a small volume of solvent whose refractive index was measured using an Abbe refractometer) to be $n_\mathrm{s} = 1.497 \pm 0.002$, from which we can determine $f_\mathrm{tet}^{(\mathrm{V})} = 1 - f_\mathrm{cd}^{(\mathrm{V})} = 0.27 \pm 0.03$ and $\rho_\mathrm{s} = 0.918 \pm 0.002$g.cm^{-3}. The density was measured independently to be 0.922g.cm^{-3}. These samples were then centrifuged again and brought to a volume fraction above the coexistence region where a monodisperse sample would be fully crystalline. The exact volume fraction was initially unknown, and the sample mass used as a measure of concentration. The contents of each cell was thoroughly homogenised by prolonged steady tumbling and manual shaking. All three cells were weighed, clamped into a sample holder to reduce vibrations and then observed over a period of many weeks. The heights of developing interfaces were monitored using a $\times 40$ travelling microscope. Crystallography was periodically performed on the samples, with particular care being taken to minimise the disturbances when moving the samples from the holder to the light scattering apparatus. When it was deemed that the samples had reached equilibrium, they were re-weighed (to quantify the amount of solvent evaporation) and diluted using an index matching solvent mixture and again thoroughly homogenised. The procedure was repeated until the samples no longer showed any crystallites: evidence that they had been diluted all the way through the coexistence region and were exhibiting equilibrium fluid behaviour expected at lower ϕ.

Batch D colloidal samples were also prepared in *cis*-decalin, to allow comparisons with the index matched experiments, since changing the solvent may alter particle interactions, and certainly changes diffusion rates and sedimentation velocities. Volume fractions were determined by centrifuging and using the literature value of RCP at this polydispersity ($\phi_\mathrm{rcp} = 0.67$) [47]. Samples were prepared in 2cm^3

cylindrical cells over a ϕ range between 0.49 and 0.59 and then left in the laboratory for observations.

If fractionation occurs during crystallisation, we expect it to be most pronounced in samples with larger polydispersities, i.e. Batch D. Consequently, representative particles from coexisting crystal and fluid phases of Batch D samples (both in *cis*-decalin and at index match) were manually extracted. Samples from a coexistence Batch C sample were also extracted.

To measure height-resolved fractionation in crystallising hard-sphere systems, two samples of index-matched Batch D colloid were prepared in 4cm^3 square-based cuvettes in the coexistence region. One was left undisturbed in the laboratory and the other was placed on a slowly rotating (one revolution per day) tumbler. This arrangement gives zero time-averaged gravity [83]. After three weeks the tumbler was stopped, and the samples left for one more week to allow the crystallites to sediment. Interface heights were measured and crystallography was performed in 1mm scans through each sample. Each sample then had consecutive 3mm bands removed for analysis by SLS to determine fractionation, and finally evaporated to calculate a mass fraction Φ_{M}.

I also performed preliminary measurements on the effects of oscillatory shear on crystal growth in Batch D and Batch E colloids, the influence of micro-gravity on crystallisation in Batch D, and the very long time crystallisation of dilute samples of Batch E.

5.3 Phase Diagram

5.3.1 Coexistence Gap

Normalised Masses, $\mathcal{M}$

Typical behaviour of the various developing interfaces for all three index-matched samples is presented in Figure 5.1. The long-time portion of each crystal branch is fitted with a straight line, and extrapolated to zero time to get the effective crystal percentage f_χ. To characterise the concentration of the different samples without introducing any assumptions concerning the phase behaviour under study (i.e. the freezing and melting volume fractions), I use a normalised mass $\mathcal{M}$, defined as the actual sample mass divided by M_{melt}, the mass at melting. M_{melt} is found by fitting a straight line through the values of f_χ as a function of sample mass in coexistence (as plotted in the inset in Figure 5.2) and extrapolating to find the mass of the sample when $f_\chi = 1$. The mass at freezing, M_{freeze}, is found from the $f_\chi = 0$ extrapolation of this straight line. The main plot in Figure 5.2 shows f_χ plotted as a function of this normalised mass, $\mathcal{M}$.

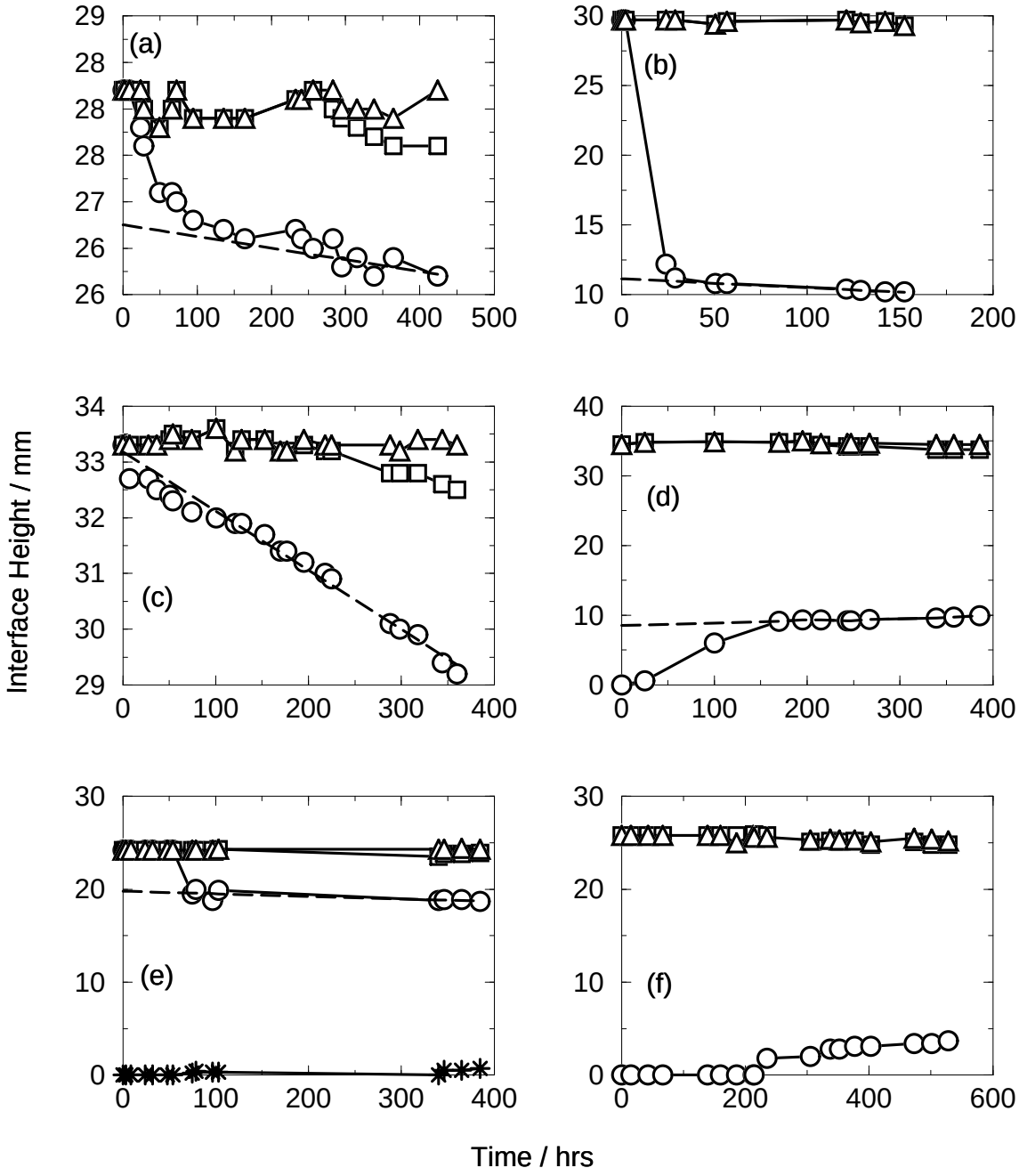

Figure 5.1: Representative sedimentation behaviour of fluid and crystal phases for index-matched samples. The top of the crystal and fluid phases are indicated by circles and squares respectively. The meniscus is marked by triangles and the linear fit through the crystal profile is a dashed line. Graphs (a) and (b) correspond to Batch A samples, with respectively 98% and 38% crystal phase. Graphs (c) and (d) are Batch C with 93% and 25% crystal. In graph (e) the stars indicate a dense amorphous sediment found at the bottom of the sample cell. The percentage of crystalline material in Graphs (e) and (f) are 82% and 0%.

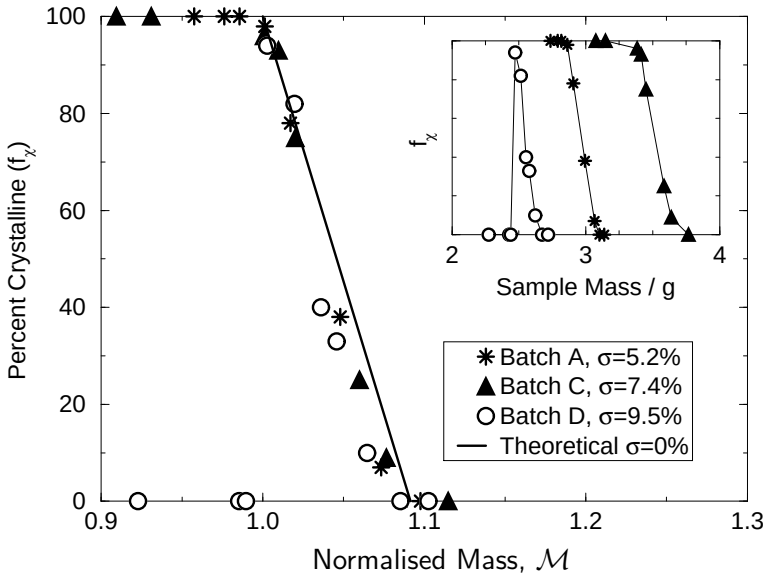

Figure 5.2: Percent crystal, f_χ as a function of normalised mass, $\mathcal{M}$. The values of $\mathcal{M}$ at freezing ($f_\chi = 0$) are 1.08 ± 0.02, 1.08 ± 0.07, 1.07 ± 0.1 respectively for Batches A, C and D. These values are related to the coexistence gap, $\Delta\phi$. In the inset, the data is plotted against the real mass of the sample. In all cases, f_χ varies linearly (within errors) with mass through coexistence. Errors are typically between 0.1% and 1% of the mass, and due primarily to evaporation.

At all concentrations, the samples of Batch A and Batch C colloids behaved similarly to monodisperse hard-spheres. For $\mathcal{M} < 1$ both samples were full of small ($\sim$ 1mm) crystallites, which became larger with dilution. At lower concentrations (higher values of $\mathcal{M}$), crystal was in coexistence with a stable fluid phase. In samples at concentrations below the freezing point, $\mathcal{M} \gtrsim 1.1$, no equilibrium crystal phase was observed, only sedimented columnar crystals, the existence of which have previously been reported by Ackerson and Paulin [68]. The extrapolation of the height of these sedimented crystals back to zero time, gave zero height, and is an indication that they are due solely to settling.

The crystallisation of the Batch D sample differs from the above pattern. In the range of ϕ in which we observe a crystal phase, it is always present sandwiched between a dilute fluid phase above and a small region ($\sim$1mm) of dense amorphous sediment underneath. On both sides of the coexistence region (i.e. below $M_{\rm freeze}$ *and* above $M_{\rm melt}$) no crystals are observed.

The width of the coexistence region, in units of the scaled mass $\mathcal{M}$, are 1.08±0.02 for Batch A, 1.08±0.07 for Batch C and 1.07±0.1 for Batch D. The errors increase as the $f_\chi(\mathcal{M})$ curves in Figure 5.2 are less precisely fitted by straight lines. This non-linearity may itself be an effect of polydispersity. The monodisperse coexistence width, calculated for a system with similar physical properties to my polydisperse samples (i.e. similar particle sizes and densities) is 1.09. The

related monodisperse $f_\chi(\mathcal{M})$ is also plotted on Figure 5.2. By using $\mathcal{M}$ as the dilution variable, we lose information regarding relative volume fractions between the samples, and cannot compare directly with theory. However we can unambiguously say that the decrease in coexistence gap, in units of $\mathcal{M}$ is only very slight over the range of polydispersities studied.

Mass Fractions Φ_{M}

As Batches C and D have similar sizes (303 and 300 nm respectively) and were prepared by the same procedure it is reasonable to assume that they also have similar thickness PHSA coatings. Consequently, relative densities can be compared by straight-forward calculation of mass fractions (Φ_{M}) rather than using less certain volume fraction values. By completely drying the samples, once dilution studies were complete, the overall mass of particles in each sample is obtained. This quantity is simply divided by the total sample mass at each dilution to obtain the mass fraction, with errors given by uncertainties due to weighing and by evaporation of solvent over the course of observations. Solvent loss due to evaporation varied noticeably from cell to cell, and from dilution to dilution, but the change in mass was always less than 1%. In Table 5.1 mass fractions, calculated for melting and freezing using the previously determined values of $\mathcal{M}$, are presented for all three batches. Errors are approximately 1%. Despite no significant change in the coexistence width, Batch D appears to freeze at noticeably higher mass fraction.

Φ_{M}	Batch A	Batch C	Batch D
Freeze	0.483	0.478	0.508
Melt	0.521	0.517	0.543
Gap	0.038	0.039	0.035

Table 5.1: Melting and freezing mass fractions.

Volume Fractions ϕ

To make comparisons with simulations, theories and future experiments, it is convenient to have absolute values of the volume fraction, ϕ. To convert mass fraction to volume fraction of effective hard-sphere particles, the parameter β (see Equation 4.7 for definition) is required, and this can only be determined through measuring the volume fraction of particles through a property which depends on the effective hard sphere volume fraction. For the quasi-monodisperse case it is standard practice to prepare a coexistence sample and, taking the values for melting and freezing from simulations, use the easily measured crystallised fraction to determine ϕ. However, since I wish to determine whether the crystallisation boundaries are altered by polydispersity, I resorted to the RCP route to determine β.

This was successful for Batch D particles, but Batches A and C both showed small iridescent grains upon spinning down, which I assumed to be crystalline regions within the amorphous RCP sediment. As crystalline regions can pack more closely than randomly arranged particles, the values for ϕ obtained by this method will be too low and consequently can only be used to place a lower bound on the calculated volume fractions. An upper bound can be calculated by assuming the sediment is entirely close packed crystal at $\phi = 0.74$. The values for β calculated assuming an RCP (FCC) sediment are 0.05 (0.15), 0.10 (0.20) and 0.13 for samples A, C and D respectively. This corresponds to an increase in core radius due to the solvated layer of 5 (14), 12 (23) and 16 nm respectively.

The volume fraction values at freezing (ϕ_{f}), melting (ϕ_{m}) and for the coexistence gap ($\Delta\phi$) are presented in Table 5.2. We can confidently say that again, in terms of ϕ, the width of the coexistence gap does not appear to depend significantly upon the polydispersity of the sample. However, it is more difficult to say whether the location of the coexistence gap alters with polydispersity due to the difficulty in exactly calibrating volume fractions, but the implication of the mass fraction measurements is that it does shift towards higher concentrations. The phase diagram showing the behaviour over a range of volume fractions and polydispersities is shown in Figure 5.3. The ϕ values for samples A and C are the average of the two techniques, and the error bar shows the typical extent of the upper and lower bounds. This is a systematic uncertainty. The random (experimental) error in each ϕ value is $\lesssim 1\%$.

Batch	A		C		D
Method	RCP	FCC	RCP	FCC	RCP
ϕ_{f}	0.449	0.504	0.468	0.525	0.519
ϕ_{m}	0.490	0.549	0.512	0.574	0.560
$\Delta\phi$	0.041	0.045	0.044	0.049	0.041

Table 5.2: Melting and freezing volume fractions for hard-sphere samples of Batch A, C and D.

5.3.2 Fluid/Glass determination

In quasi monodisperse hard sphere systems above the glass transition $\phi_{\mathrm{gt}} \approx 0.58$, large, irregularly shaped heterogeneously nucleated crystals are seen. However, Henderson *et al.* observed that hard spheres with $\sigma = 11\%$ did not exhibit these large crystals above ϕ_{gt} [84], but did crystallize as expected at lower values of ϕ. Also, Bartlett and Pusey have previously noticed [78] that a $\sigma \approx 8\%$ sample exhibited similar behaviour to the Batch D samples prepared for this study. That is, crystals were seen in coexistence with a fluid, but no crystallites were observed at volume fractions above the coexistence region. They suggested that a glass transition prevented the sample from crystallising, but "because of the difficulty in determining absolute volume fractions it was not possible to decide whether

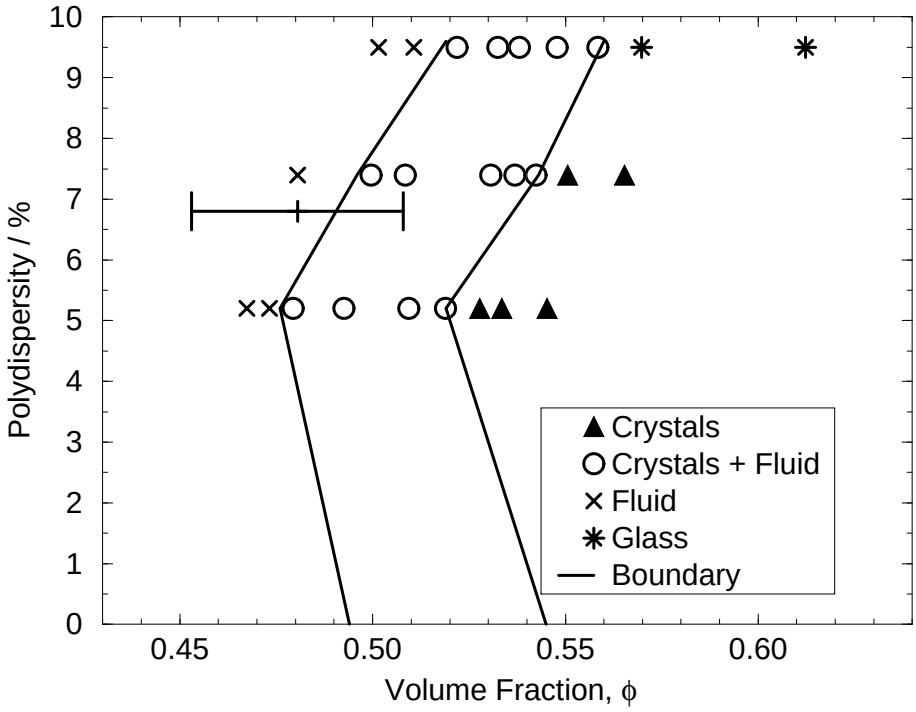

Figure 5.3: Polydisperse hard sphere phase diagram. The points correspond to experimental samples whose behaviour was determined from visual observations and whose volume fractions are calculated as discussed in the text. The error bar shows the typical lower and upper bounds on the volume fraction measurement for Batches A and C. No significant narrowing of the coexistence gap is observed.

ϕ_{gt} decreased from the value found in a monodisperse system or ϕ_m increased." Recently, theoretical work [85] has suggested that a re-entrant fluid phase may be stable at high volume fractions in sufficiently polydisperse samples, which could also explain the lack of crystallisation.

In an attempt to resolve these uncertainties, two non-crystallising samples of Batch D at $\phi \approx 0.57$ and $\phi \approx 0.61$ were analysed by two colour dynamic light scattering (TCDLS) [73]. This technique provides information regarding differences between time and ensemble averaged quantities which can subsequently be used to establish the value of the non-ergodicity parameter $f(q, \text{“}\infty\text{”})$ [86]. This is a measure of correlations at a given q-vector between a sample at $t = 0$ and at $t = \text{“}\infty\text{”}$ (the longest experimentally accessible time), defined in such a way that it takes on the value 0 for ergodic systems and 1 for those which are completely frozen. For the $\phi \approx 0.57$ sample just above the coexistence gap, the time averaged scattered intensity, measured over 15 hours, at a given angle (near to the peak of the structure factor) was found to differ from the value obtained by averaging over many ensembles (speckles). This is an indication of non-ergodicity. We also found that $f(q, \text{“}\infty\text{”})$ for three different angles was only slightly lower than the reported measurements [86] for a glassy sample with comparative volume fraction ($\phi \approx 0.563$) but lower polydispersity ($\sigma \approx 5\%$). We conclude that our sample is possibly ergodic but only on a time-scale greater than the longest experimental time (15 hours). The slow dynamics and probable glass transition effectively blockade the route to crystallinity. This conclusion stands independently of the uncertainties of precise volume fraction calibration.

It is believed (see e.g. [87] where Bartlett argues for scaling ϕ_{gt} with the simulation values determined for $\phi_{rcp}(\sigma)$ in [47]) that the glass transition will move to higher volume fractions for increased polydispersity, possibly as high as $\phi_{gt} \approx 0.61$ for samples with $\sigma = 10\%$. Using this value to calibrate Batch D volume fractions, we find additional evidence for the coexistence gap shifting towards higher volume fractions.

More quantitative analysis of these TCDLS measurements is currently in progress and should be published shortly [88].

5.3.3 Fractionation

Representative samples were extracted from coexisting fluid and crystal phases. These were diluted in *cis*-decalin and the mean particle size and polydispersity determined by fitting Gaussian PSDs to form factors measured using SLS. Table 5.3 summarises these measurements, taken on a number of different Batch D coexistence samples, and on one Batch C sample. Batch D samples show slightly larger, more monodispersed particles in the crystal phase than the fluid phase. The Batch C samples show no observable fractionation. The measurements on Batch D samples show distinct variations in the mean radius from sample to sample. This is attributable to absorption of tetralin by the particles, which,

even after dilution in *cis*-decalin remains in the outer regions of the particles and alters the form factor in an unpredictable way. As the particles in coexisting phases are always exposed to the same solvent environment, we assume that the monodisperse form factors from each phase are identical. Differences in the measured form factors are solely due to fractionation between the phases. The sample in *cis*-decalin does not suffer from this problem.

Batch	Solvent	f_χ	$\bar{R}_{\text{fl}}$, σ_{fl}	$\bar{R}_\chi$, σ_χ	$\Delta\bar{R}$, $\Delta\sigma$
D	index-matched	0.68	276nm,11.5%	280nm,10.0%	4nm,-1.5%
D	index-matched	0.88	285nm,10.3%	286nm,10.1%	1nm,-0.1%
D	*cis*-decalin	0.05	300nm, 9.5%	303nm, 8.8%	3nm,-0.7%
C	index-matched	0.91	295nm, 6.4%	295nm, 6.4%	0nm, 0%

Table 5.3: Fractionation measurements for coexisting crystal-fluid samples. The fractional phase volume of crystal before extraction is f_χ. The differences between mean radii ($\Delta\bar{R} = \bar{R}_\chi - \bar{R}_{\text{fl}}$) and polydispersity ($\Delta\sigma = \sigma_\chi - \sigma_{\text{fl}}$) are listed in the final column.

5.4 Discussion

5.4.1 Theoretical Predictions

Several authors have calculated details of the phase behaviour of polydisperse hard spheres, using a variety of techniques and assumptions [36, 62, 89–94]. The values of the terminal polydispersity σ_{T}, of the coexistence gap $\Delta\phi$ and the predicted differences in radius and polydispersity (defined as the crystal value minus the fluid value), $\Delta\bar{R}$ and $\Delta\sigma$ determined in each of these works are presented in Table 5.4. They all agree on the existence of a terminal polydispersity $\sigma_{\text{T}} \approx 10\%$ above which a system of hard spheres cannot crystallise without fractionating. Other aspects of the behaviour such as fractionation and coexistence gap narrowing, are however, in dispute. Many authors either ignore, neglect or eschew the problems of fractionation, with only Bartlett and Bolhuis & Kofke explicitly calculating size distributions in coexisting phases.

Any complete theory of polydisperse hard-sphere crystallisation must include fractionation predictions and be consistent with the main experimental discoveries presented in this chapter, which, in summary, are:

- The coexistence gap does not narrow appreciably as the polydispersity of the sample is increased.
- There is only slight fractionation between crystal and fluid phases. The crystal phase contains particles which are at most 2% larger, and more monodispersed ($< 1\%$ smaller polydispersity).

Author	Method	σ_{T}	$\Delta\phi$	$\Delta\bar{R}$, $\Delta\sigma$
D&P [36]	MD	11.3 %	0	N/A
MK&K [62]	BD	$\sim 7\%$	N/A	N/A
B&H [89]	DFT	$\sim 6.6\%$	~ 0.05	"very cumbersome"
McR&H [90]	DFT	"exceeds $\sim 5\%$"	~ 0.03	"constrained eutectic"
B&K [91, 95]	MC	5.7%	0.041	$\sim$5%, -6.1%
Bartlett [92]	MFT	8.3%	0	$\sim$1%, $< 1\%$
PRZ&C [93]	MFT	12.1%	N/A	N/A
Pusey [94]		11%	N/A	N/A

Table 5.4: Comparison of predictions for the terminal polydispersity σ_{T} and fractionation. The methods used were Molecular Dynamics simulations (MD) by Dickinson and Parker, Brownian Dynamics (BD) by Moriguchi and co-workers, Density Functional Theory (DFT) by Barrat and Hansen and McRae and Haymet, a simple melting criterion by Pusey, Monte Carlo (MC) simulations by Bolhuis and Kofke and a Mean Field Theory (MFT) by Bartlett and Russel and co-workers. Values of the coexistence gap $\Delta\phi$, and the differences between crystal and fluid radii and polydispersities ($\Delta\bar{R}$ and $\Delta\sigma$) are taken at the terminal polydispersity (σ_{T}), where possible.

However, we do not ask for agreement with the observed arrest of crystallization due to the glass transition as this is inherently a dynamic, or non-equilibrium effect, which would not be accounted for in any equilibrium theory. As both Bolhuis and Kofke [91, 95] and Bartlett [92] predict phase diagrams and make predictions concerning these principal observations I review their results in a little more detail here. Accurate sketches of their respective phase diagrams are shown in Figure 5.4. Despite general agreement over the existence of a terminal polydispersity, there are significant differences in some of their more detailed predictions which others have not calculated at all.

Bolhuis & Kofke's Monte Carlo Simulation

The phase diagram of Bolhuis & Kofke was determined by using Monte Carlo integration along the crystal-fluid coexistence boundary. They simultaneously simulated a fluid and an FCC solid phase at equilibrium, each of either 256 or 864 particles and allowed the particle sizes to fluctuate, with the energy penalty for each size of particles given by an imposed Gaussian chemical potential profile. Originally [91], they found a terminus to the coexistence region at which point the mean particle size in the crystal was over 5% larger than in the fluid and the polydispersities differed by a factor of two: 5.7% for the crystal and 11.8% for the fluid. The volume fractions were 0.588 and 0.547 for the solid and fluid, respectively. More recently [95] they extended their calculations and found that the coexistence region continued indefinitely beyond the previously determined terminus. For more polydisperse fluid phases, the precipitated crystal becomes

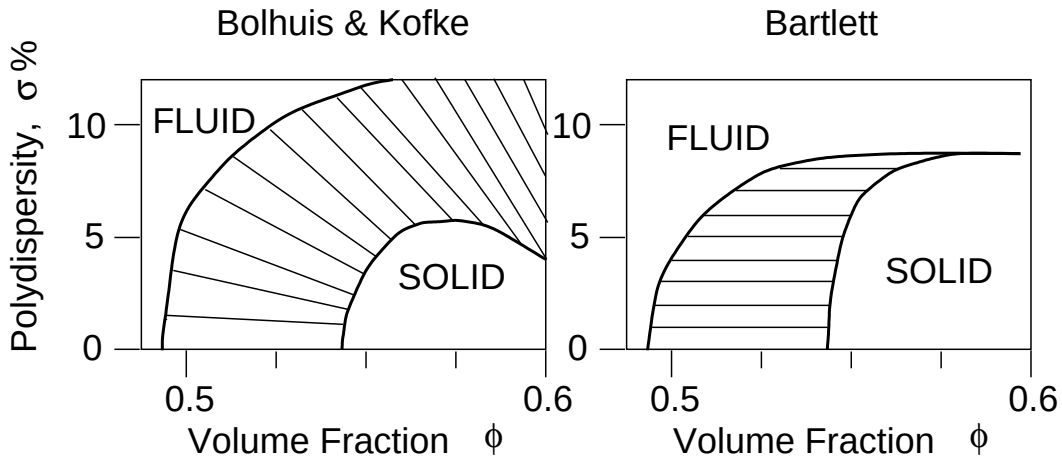

Figure 5.4: Theoretical polydisperse hard-sphere phase diagrams as calculated by Bolhuis & Kofke and Bartlett. The theories differ predominantly over their predictions for fractionation, as can be noted by the slope of the tie-lines: slanted tie-lines imply different σ in fluid and crystal and hence fractionation.

more monodisperse and more compact, eventually approaching the theoretical close packed limit for single sized spheres at $\phi \approx 0.74$. The properties of the phases at the original terminus show the greatest value for the coexistence gap, $\Delta\phi = 0.588 - 0.547 = 0.041$ which is only slightly less than the monodisperse value of 0.051.

Bartlett's Mean Field Theory

In [92] Bartlett calculated the phase diagram using a geometrically-based mean-field theory (i.e. inter-particle correlations are neglected). He assumes that the polydisperse system can be completely characterised by the first four moments of the PSD (specifically, the number density, the mean radius, the mean square radius and the volume fraction ϕ) which, in the case of a binary mixture, can all be independently adjusted. Using ideas from the scaled particle theory (SPT) of a binary system, he models a truly polydisperse system using a two component model. He finds good agreement with the Bolhuis & Kofke results for the pressure in the two phases as a function of σ, and general agreement with their phase diagram. The terminal polydispersity is at $\sigma_{\mathrm{T}} = 8.3\%$ at which point the fluid and solid densities become equal, and therefore $\Delta\phi = 0$, in contrast to the value of 0.041 for Bolhuis & Kofke. Above σ_{T}, the system does not crystallise. This theory predicts almost no fractionation in particle size or in polydispersity, both of which at the terminus are approximately 1% smaller in the fluid phase. At volume fractions above the stable crystal region he predicts a stable re-entrant fluid phase [85]. However, it is likely that the glass transition will intervene and prevent experimental observation of this re-entrant phase. Additional work by Bartlett [87] indicates the possibility of multi-crystal phase coexistence with

an increasing number of distinct crystal phases becoming stable as ϕ and σ are increased.

5.4.2 Comparing Theory with Observations

My experimental observation of crystals forming in samples at polydispersities up to 9.5%, but not at 18% is in quantitative agreement with all previous terminal polydispersity predictions of σ_{T} in the range $5\% - 20\%$. My measurement of $\Delta\phi$ not altering significantly as a function of σ is in general agreement with Bolhuis & Kofke, but not with Bartlett. Conversely the observation of negligible fractionation agrees with Bartlett's prediction but not with that of Bolhuis & Kofke.

Recent theories by Bartlett extending his MFT work [87] and by Sear using a cell theory free energy for the crystal phase [13] have both predicted coexisting, fractionated crystal phases, the number of which increases with the overall polydispersity. This sort of phenomenon could possibly reconcile the predictions of B&K, and of Bartlett with my observations. Firstly, multiple crystal phases would not be observed in the small single-crystal simulation of Bolhuis & Kofke but by including this possibility, fractionation between fluid and crystal phases could be drastically reduced. Also by allowing at least two distinct crystal phases in the theoretical work of Bartlett, it is likely that $\Delta\phi$ will not tend to zero. Detailed determination of the full coexistence behaviour would be required to resolve this, rather than the initial stability calculations performed to date [87].

To resolve the lack of experimentally observed fractionation with the multi-crystal hypothesis, we propose that individual crystallites are composed of a narrower distribution of particles. Separate crystallites may possess different mean particle sizes but any measurement of particle size on a sufficiently large extracted volume will average over enough crystallites to mask the fractionation. Coexisting crystallites must have equal osmotic pressures, Π which (at least in the ideal gas limit, $\Pi = \rho k_{\mathrm{B}} T$) implies equal values of ρ and not of ϕ. As the angular position of Bragg reflections is dependent on the lattice parameter and therefore ρ, *all* crystallites in mechanical equilibrium should have coincident Bragg reflections, independent of volume fraction and mean particle radius. Therefore, *in situ* light scattering studies would also be insensitive to detecting multiple crystal phases. Even away from the ideal gas constraint, any smearing or splitting of the Bragg peak due to different lattice parameters would be experimentally difficult to detect. Further investigations would be necessary to conclusively find out whether this proposed fractionation does occur.

The Dense Amorphous Layer

The existence of a dense amorphous layer has also been reported by others [60,96], but no rigorous explanation has been proposed. Owing to the small spatial extent and the dense nature of this "phase" I was unable to perform light-scattering measurements to probe the structure and dynamics of this layer. One possibility is that the sediment is the re-entrant fluid phase, recently predicted by Bartlett and Warren [85] to be in equilibrium with a high density polydisperse crystal. If this were the case, we would expect this phase to grow at the expense of the crystal phase, as crystalline regions are compressed and melt into the more efficiently packed fluid layer. However, long time ($\sim$ 80 day) observations showed no significant growth of this layer. One such sample was slowly centrifuged ($\sim$ 1500rpm) for several days, which effectively increases gravity by more than a factor of 100, and hence accelerates any sedimentation process by a similar factor. After an equivalent "normal gravity time" of over 800 days, no change in the height of this layer was observed, although the crystal had compacted to $\sim 62\%$ of its initial volume. An alternative explanation consistent with this observation is that this layer is non-ergodic, or glass-like, in which the particles have insufficient space to crystallise. It forms by the initial sedimentation of particles near the bottom of the sample, before they have time to arrange into crystalline regions. Later on, they are denied the space they require to arrange themselves due to compression by the rest of the sample above them. Samples in micro-gravity or density matching solvents would then not have this layer.

5.4.3 Solving the Cell Model Free Energy

Motivated by the observation of minimal fractionation and the existence of analytic expressions for polydisperse crystal and fluid free energies, I chose two simple forms for the fluid and crystal free energies and, imposing equal polydispersities in both phases, solved the equilibrium conditions, adapting a program from Warren. I used a cell model for the crystal free energy per particle $f_{\rm cr}(\phi,\sigma)$ [13] which estimates the entropy of the crystal by calculating the volume available to a particle of a given radius in a cage formed by particles with the mean radius (this is the mean field approximation). This is given by the expression

$$\frac{f_{\rm cr}(\phi,\sigma)}{k_{\rm B}T} = \frac{\sqrt{3}}{\sigma}\left[X^{-}\,\ln(X^{-}) - X^{+}\,\ln(X^{+})\right] - \ln(\sigma), \tag{5.1}$$

where

$$X^{\pm} = \left(\frac{\phi_{\rm cp}}{\phi}\right)^{\frac{1}{3}} - 1 \pm \frac{\sqrt{3}\sigma}{2}, \tag{5.2}$$

and $\phi_{\rm cp}$ is the usual value for closest packing of single sized spheres. The fluid free energy $f_{\rm fl}(\phi,\sigma)$ is derived from a Padé approximant for a monodisperse hard sphere equation of state [10] with radius equal to the sample mean, and is given

by

$$\frac{f_{\rm fl}(\phi,\sigma)}{k_{\rm B}T} = \frac{4\,\phi^2 - 6.10\phi^3 + 1.78\phi^4}{1 - 2.77\phi + 2.38\phi^2 - 0.49\phi^3 - 0.12\phi^4 - 0.01\phi^5} + \phi\,\ln(\phi) - \ln(\sigma). \tag{5.3}$$

In both free energies the final $\ln(\sigma)$ term accounts for the entropy of mixing. A function of the form $a+b\phi$ is added to the fluid free energy to enforce the expected monodisperse behaviour (coexistence between a fluid at $\phi = 0.494$ and crystal at 0.545) at $\sigma = 0\%$. The calculated phase diagram as plotted in Figure 5.5 agrees well with the more exact result of Bartlett, and also predicts a re-entrant fluid phase.

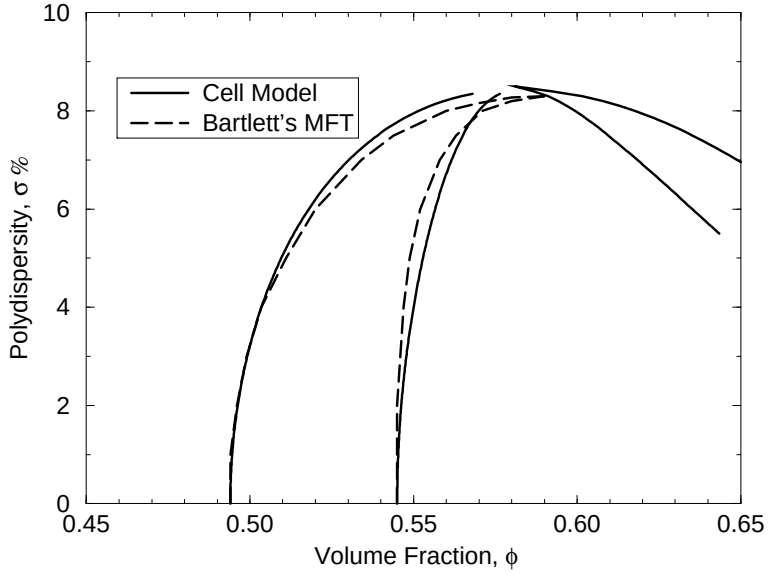

Figure 5.5: Theoretical phase diagrams calculated using Mean Field Theory. The dashed line is Bartlett's results discussed earlier. The solid lines were calculated as described in the text, using a cell theory free energy for the crystal, and display re-entrant fluid behaviour to the right of the normal coexistence region.

5.4.4 Observations of particles in *cis*-decalin

Samples of Batch D colloid were also prepared in *cis*-decalin and studied by visual observations. In general, the behaviour of the particles in this solvent was similar to the observations in a *cis*-decalin/tetralin mixture: crystal fluid coexistence was observed across a narrow range of volume fractions, and above this region, the samples did not fully crystallise. The one interesting difference was that in this region above coexistence a small band of crystals was observed near the top of the sample just below the meniscus. Figure 5.6 shows the fractional heights of interfaces in the sample as a function of volume fraction (determined from $\phi_{\rm rcp}$ and the value of β calculated above). The coexistence gap is slightly smaller than at index match: $\Delta\phi = \phi_m - \phi_f = 0.530 \pm 0.005 - 0.500 \pm 0.005 = 0.030 \pm 0.007$.

Also the location of the coexistence gap is at lower volume fractions than at index match, possibly due to my using the matched value of β for volume fraction calculations.

The observed crystal bands are reminiscent of the heterogeneously nucleated crystals seen in lower polydispersity hard sphere glass samples, and act as further evidence in favour of the glass transition preventing crystallization.

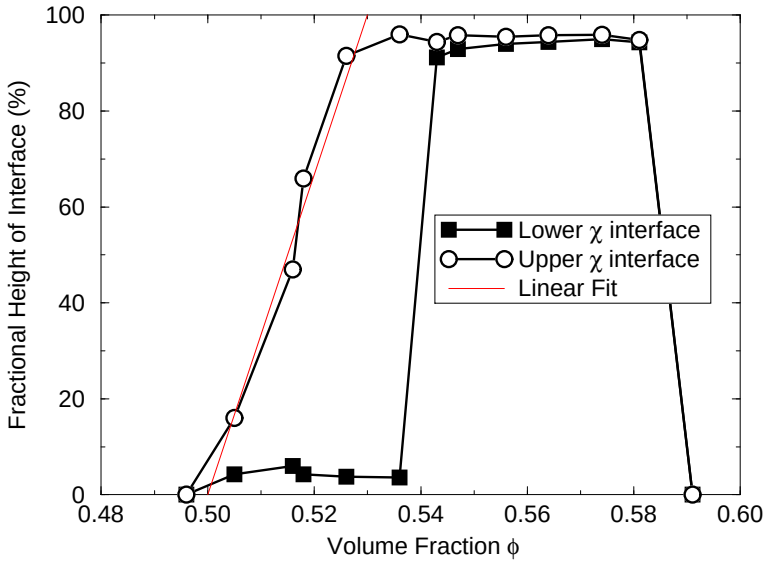

Figure 5.6: Phase Behaviour of Batch D colloid in *cis*-decalin . The vertical extent of the crystal phase is the region between the squares and the circles. A linear fit through the coexistence region gives $\Delta\phi = 0.03 \pm 0.01$. A dense amorphous layer is seen below the crystalline phase. For $\phi \gtrsim 0.54$ a narrow band of crystals are seen just below the meniscus.

5.5 Additional Observations

In this section I present more speculative results based upon secondary, sometimes almost incidental observations of the crystallisation phenomenon. These include time resolved, or kinetic, measurements, which only arise as a consequence of determining the equilibrium phase behaviour. Others (e.g. van Megen in [81]) have studied the kinetics of crystallisation in mono- and polydisperse hard sphere systems with much more rigour than I. Secondly I present results from spatially (height) resolved fractionation measurements, the interpretation of which is at present very speculative. Thirdly I mention the effect of shear on crystallisation, which I observed in a short preliminary experiment. I then briefly comment on experiments performed in micro-gravity on board Space Station Mir, and finally on an observed crystal band in a dilute Batch E sample.

5.5.1 Time Resolved Measurements

Nucleation and Equilibration of Crystal Phases

The data obtained in the visual observation experiments present two relevant time-scales with which to quantify the kinetics of crystal-fluid separation. The first of these is the nucleation time τ_{nucl} required until crystallites are first observed. As an artifact of the daily observations, this value is only accurate to within a minimum of 24 hours. The second time-scale is the equilibration time τ_{equil}, which I define as the amount of time required until the sample reaches the linear sedimentation regime. This value is extracted from the sedimentation profiles plotted in 5.1 and could depend upon densities, viscosities and particle sizes. These times are plotted in Figure 5.7 as a function of volume fraction.

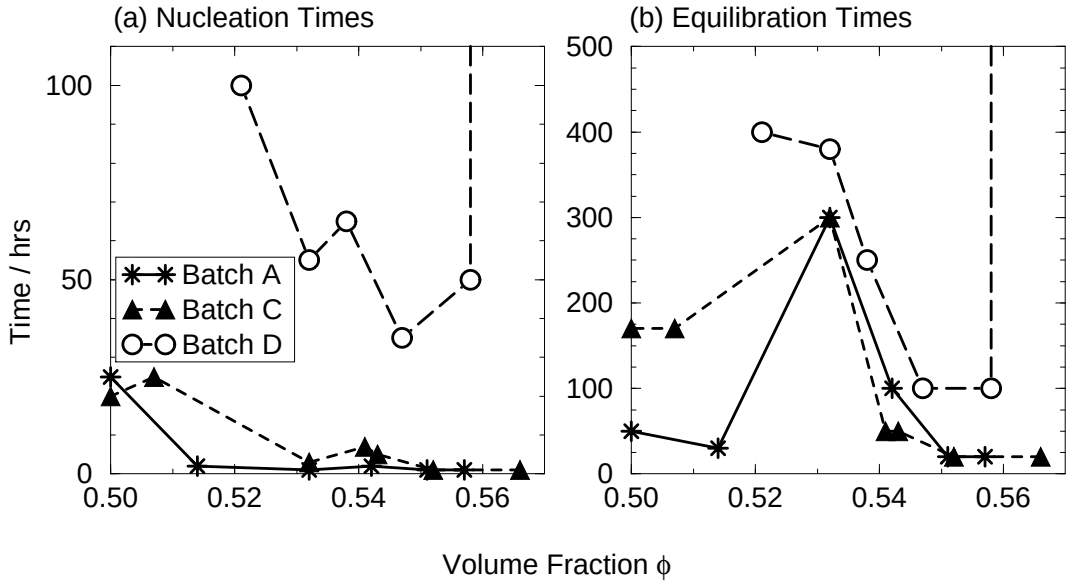

Figure 5.7: Kinetics of crystallisation in polydisperse hard sphere systems. The left hand plot shows the time until crystals were first observed, which we take as an estimation of the nucleation time. The right hand graph shows the time required until the crystal sedimentation reaches a linear settling regime. Batch D is always slower than Batches A and C.

From Figure 5.7 Graph(a) we can see that the nucleation times for Batches A and C are similar, and they are in-fact in qualitative agreement with much more accurate measurements made by van Megen and Ackerson [81,97]. Nucleation rates are fastest near ϕ_{m} and become progressively slower at lower (and higher) volume fractions. These samples have nucleation times of $\sim$1 hour for $0.52 \lesssim \phi \lesssim 0.56$, increasing to 24hours at $\phi = 0.50$. Nucleation times for Batch D are significantly slower, but follow the same trend. The shortest nucleation time ($\tau_{\mathrm{nucl}} \approx 24$ hrs) is around ϕ_{m}, increasing to four times this value at lower volume fractions. Retardation due to polydispersity is well documented [82, 84], and has been explained

by multiple theories. Some of these are built upon the premise of an increased energy barrier to nucleation caused by a diminished chemical potential difference between the two phases, others rely on the fact that the sample *must* fractionate in order to crystallise and this is an inherently slow process, and others still on the supposition that the higher density of the metastable fluid and the proximity to the glass transition is sufficient to slow the relevant particle diffusion velocities. As the chemical potential difference and $\Delta\phi$ are both derived from the free-energy landscape, and as $\Delta\phi$ is not observed to reduce significantly, I remain unconvinced by the "increased energy barrier" argument. I believe the other suggestions are both plausible and it would require careful measurements of diffusion in the metastable fluid and very small scale extraction to determine which is the dominant factor.

The equilibration times plotted in Figure 5.7 Graph(b) also indicate that Batch D is slower to reach the linear settling regime, but the differences are less than for nucleation. There is a noticeable peak in the equilibration times at $\phi \approx 0.53$. This may be due to trade off between a rapid decrease in nucleation time and a decrease in the total number of crystallites present at equilibrium. Samples at higher ϕ nucleate crystals much faster, and at lower ϕ, the nucleation rate is similar, but less crystal phase forms.

As this study was not primarily an investigation into the kinetics of crystallisation, focusing instead on the phase behaviour once equilibrium is reached, there are no real conclusions from this section, except to add to the growing mountain of evidence that polydispersity slows down crystallisation.

Evolution of Crystals

Occasional crystallographic measurements were performed on the crystallising samples. The act of moving the samples across the room and into the sample holder on the light scattering apparatus was always performed with utmost care. Some disturbance of the sample was presumably unavoidable, although no evidence for this was ever actually seen. The angular position of the observed Bragg peaks enables the nearest neighbour separation d_{nn} to be calculated. A change in d_{nn} can be accounted for by one of two possibilities. Either the crystal volume fraction or the average particle size is changing. As the crystals are non-ergodic, and particles once incorporated into a crystallite will remain there indefinitely, changes in lattice parameter with time must be due to crystal compression or expansion. However when comparing the same sample but at different concentrations, having been diluted and thoroughly mixed, it is possible that changes in the lattice parameter are due to either different volume fractions or different average particle sizes.

For the interpretation of these crystallographic results I assume that the mean particle size in the crystal phase remains constant at all concentrations. Therefore variations in d_{nn} from one dilution to the next will indicate that the coexistence

crystal is not at the constant volume fraction given by ϕ_χ. Owing to the slanted tie-lines predicted by Bolhuis & Kofke, they would expect the coexistence crystal volume fraction ϕ_χ to change (in fact decrease) as a sample is diluted through the coexistence region. The straight tie-lines in the theory of Bartlett, however, would predict no change in ϕ_χ

The data presented in Figure 5.8 does not show any systematic change in $d_{\rm nn}$ of the crystal, as the overall volume fraction of the sample is changed. For each Batch the mean value for $d_{\rm nn}$ averaged over all samples, is calculated to be 578±2, 700±4 and 670±3 nm for Batches A, C and D respectively. These values can be combined with the nominal values of the particle radii to determine the mean volume fraction of the crystal phase,

$$\phi_\chi = \frac{16\pi}{3}\left[\frac{\bar{R}}{\sqrt{2}d_{\rm nn}}\right]^3 . \tag{5.4}$$

The average values for the three crystalline phases are $\phi_\chi = 0.45\pm0.02$, 0.47 ± 0.03 and 0.53 ± 0.01. That these volume fractions are lower than those previously determined by spinning and evaporating, is due to the slightly larger effective hard-sphere radius.

At a fixed overall ϕ, samples show evidence of ϕ_χ changing in time. An increasing trend is due to gravitational compression and a decreasing trend is caused by the crystal relaxing: as more crystallites form, the density and hence the osmotic pressure of the fluid phase decreases, allowing the crystal to expand. I have not perused this issue further, but it seems that which effect will dominate is not entirely clear beforehand. Ackerson and Schätzel in [97] introduce a "kinetic parameter" which controls this crystal expansion/relaxation times, and this factor could possibly be connected to physical properties of the system.

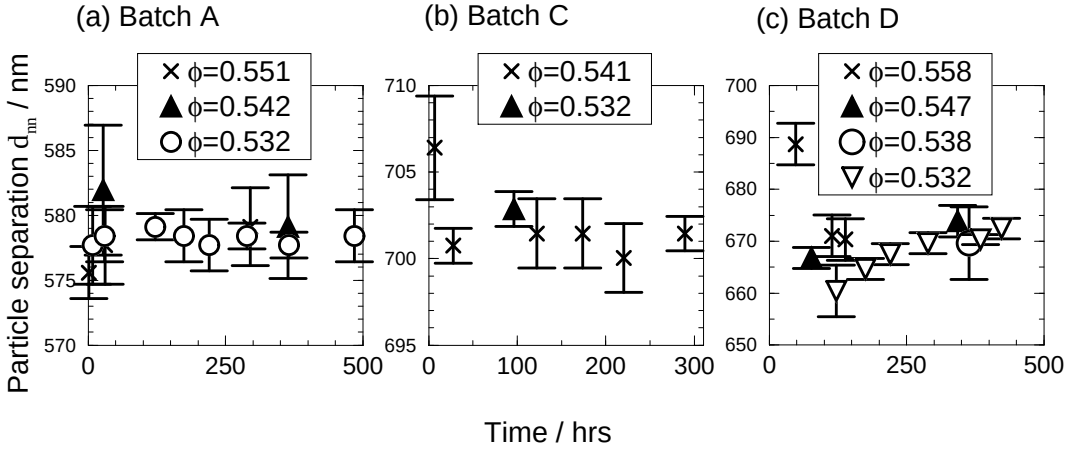

Figure 5.8: Evolution of particle spacing $d_{\rm nn}$ as a function of time for different polydispersities and volume fractions. There is insubstantial evidence of a systematic increase/decrease in ϕ_χ as the sample is diluted through the coexistence region.

From the time resolved crystallographic measurements we can also study how the

crystal structure evolves. Emergence of the 200 peak indicates that the crystal is ripening towards an FCC packing of layers. Batch A always eventually showed a 200 peak, after a minimum time of 122 hours. Batch C behaved likewise, with the minimum time as 245 hours. Batch D never developed the 200 peak, even after 423 hours. As nucleation times differed between Batches B and D by approximately one order of magnitude, perhaps we should wait for a similarly scaled time before seeing FCC crystals in Batch D ($\sim$ 1000 hours or 40 days). However, additional experiments taken after 80 days, and then again after gentle centrifuging for a "normal gravity time" of over 800 days failed to show the emergence of the 200 peak.

ϕ	Batch A		Batch C		Batch D
	Random	FCC	Random	FCC	Random
0.56	-	-	-	-	139
0.55	31	295	-	-	343
0.54	27	364	220	245	364
0.53	30	122	97	342	423

Table 5.5: Evolution of crystal structures. The latest times (in hours) that the different batches were observed to still be in a randomly stacked crystal structure are recorded in the "Random" columns. The earliest times the scattering pattern showed the 200 Bragg peak, the signature of ripening towards an FCC crystal, are in columns "FCC". A dash (-) indicates no experiment at this volume fraction.

5.5.2 Space Resolved Fractionation

In Section 5.3.3 we showed that bulk fractionation is not significant in our crystallising hard-sphere systems. However, Bartlett [87] and Sear [13] have demonstrated that fractionation between multiple crystalline phases may be possible, and we have already used such an argument to align theoretical and simulation results with our data. By extracting material from narrow bands through a sample, we hope to gain insights into localised fractionation and the effect of gravity. We may expect gravity to play more of a rôle in polydisperse systems, as the crystallisation times are sufficiently retarded to be comparable with gravitational settling. In some cases, for example the sedimentary crystals observed in dilute Batch E samples (see Section 5.5.5), it even appears that gravity aids crystallisation. Consequently, we allowed one sample to come to equilibrium in normal gravitational conditions, and another was tumbled very slowly (one revolution per day), resulting in a time-averaged-zero gravity.

The suspension from the extracted bands is analysed by evaporation to determine volume fractions, and by fitting form factors to SLS data to determine radius and polydispersity. Together, we gain information on fractionation of the first, second and third moments of the distribution.

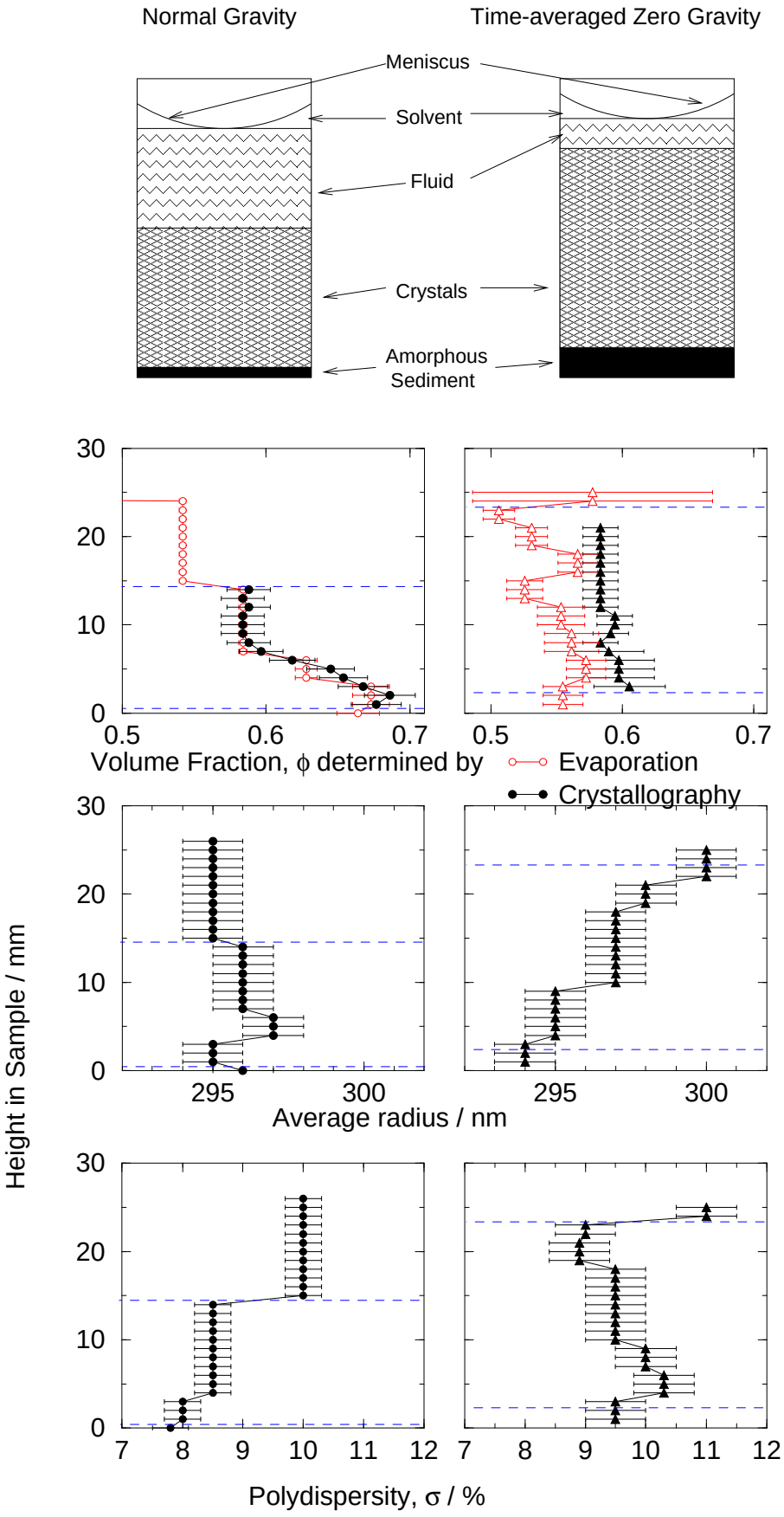

Figure 5.9: Results of Fractionation study on Batch D in normal and time-averaged zero gravity conditions.

Volume Fraction Measurements

Crystallography measurements were taken of narrow (∼1 mm) bands through both samples. The average nearest neighbour separation within each crystal band was deduced from the location of each Bragg peaks using equation 4.51, and averaged over all peaks. The volume fraction of the band was then calculated from Equation 5.4, using the hard sphere radius determined in the extraction measurements (see next Section), and neglecting the effect of the solvated layer. Core volume fractions ϕ_c were also measured by evaporating the extracted material and converting to ϕ using the previously determined value of $\beta = 0.13$. Good agreement between both methods was found.

The top two graphs in Figure 5.9 show how ϕ varies with height in each sample. The normal gravity sample had a crystal which decreased in ϕ from 0.68 to 0.58 over the bottom 8mm, presumably due to compression under the weight of colloid above. Above 8mm, ϕ_χ remained at 0.58 for the rest of the crystal phase, and dropped to 0.54 in the fluid phase. In contrast, the zero-gravity sample showed no such gradient, but had a constant value of $\phi_\chi \approx 0.58$ throughout the crystal. The fluid phase of this sample was very small and proved difficult to extract and evaporate accurately.

Radius Measurements

Prior to evaporation, a drop of the material extracted from each narrow band was diluted and analysed in SLS for $\bar{R}$ and σ measurements. The values found by fitting theoretical form factors calculated for Gaussian PSDs are plotted in the middle graphs in Figure 5.9. In normal gravity, no size fractionation (within errors) is observed. However, in zero-gravity, larger particles are found nearer the top of the sample. This is in contrast to predictions from Bartlett [92] and Bolhuis and Kofke [91] who predict larger particles in the crystal phase. That the radii are not consistent with an overall mean of 300nm can be explained by a previously used argument: these particles have been exposed to a solvent environment of *cis*-decalin and tetralin for a considerable time (many months) and have almost certainly absorbed some tetralin. This will have altered the form factors but identically for both the fluid and the crystal phase particles so relative fractionation measurements are still perfectly valid. As these two samples themselves have different solvent histories they are not directly comparable. To avoid this problem, the particles could have been washed in pure *cis*-decalin after extraction and allowed to expel any previously absorbed solvents.

Polydispersity Measurements

Polydispersity as a function of height is plotted in the lower two graphs of Figure 5.9. In both cases, the polydispersity in the fluid phase ($\sigma \approx 10.5\%$) is greater

than in the crystal phase ($\sigma \approx 9.4\%$). Unlike the radius measurements, there does not appear to be significant variation of the polydispersity with height through either crystal phase.

Discussion/Brain Storming

Interpreting the spatially resolved fractionation data is not straightforward. Here I discuss one possible explanation.

Let us assume that the stock solution PSD is positively skewed so that the modal value is less than the mean and there is a long tail to the distribution. Crystals then form selectively, using only particles of roughly the same size. In a given time, crystals composed of smaller particles may grow to larger sizes, either because more smaller particles are available, or because of their higher mobilities (faster diffusion rates). When the slow tumbling is stopped, all crystallites will have the same ϕ and hence density, but the larger crystallites, composed of the smaller particles will sediment more rapidly, due to the quadratic dependence of sedimentation velocity on an object's radius. With gravity "turned on", crystals grow and sediment at the same time and this effect becomes less significant.

Pushing this speculation further, the lack of height dependence on the polydispersity measurements may be because in any given band of crystalline phase, there are enough crystallites composed of slightly different particle sizes to give a certain value of the polydispersity. Larger extracted samples would presumably give larger polydispersities, and if it were possible to extract an individual crystallite this would have a very narrow PSD. The ergodic fluid phase, however, is composed of particles sampling the entire distribution, and any measurement of σ will give a representative ensemble average. In other words, if $\bar{R}$ in the crystal phase varies from one crystallite to the next, we need a sufficiently large number of crystallites to achieve a representative ensemble average of σ for the entire crystal phase.

Single-crystal-extraction, light-microscopy fractionation studies, or single crystal crystallography could be employed to resolve this matter.

5.5.3 The Effects of Shear

A small sample of Batch D colloid at $\phi \approx 0.57$ was placed in a shear cell with linear plate geometry designed by Haw [98], with shear amplitude of 400μm, plate separation of 600 μm and oscillation frequency of 0.5Hz. The sample was studied using an optical microscope throughout the shearing experiment. After 15 minutes, no crystalline order was observed. After one hour, the particles were arranged in a hexagonal pattern, and the presence of six Bragg spots when illuminated by a low power laser, confirmed the crystalline order. In the same confined

geometry, without shear, this particular sample did not show any order after one week. A sample of Batch E colloid was also placed in the apparatus, at an initial volume fraction of $\phi \approx 58\%$. A variety of shear frequencies and amplitudes were attempted (admittedly in a fairly haphazard way) while ϕ increased unchecked through solvent evaporation. Crystalline order was never observed in this system.

5.5.4 Micro-gravity Experiments

Two index matched Batch D samples were prepared in the coexistence region. Under normal gravity conditions both samples showed fluid-crystal coexistence. Photographs taken in micro-gravity (where the acceleration due to gravity is $10^{-6}g$) on board the Space Station Mir showed no evidence of crystallites after many weeks. However unless the sample illumination is carefully set up, the distinctive crystal iridescence can easily be missed by the camera. Also, this particular mission suffered many publicised misfortunes, which may have disturbed the samples and affected the crystallisation process. Future experiments both, in micro-gravity and using solvent mixtures which match the particles' density, will enable further investigations into the importance of gravity in crystallising hard sphere systems.

5.5.5 Crystals in Batch E samples

Samples of Batch E colloid ($\sigma = 18\%$) were prepared in *cis*-decalin with ϕ values of 0.1, 0.4, 0.5 and 0.6. Those in the ϕ range between 0.4 and 0.6 were never observed to crystallise over the course of many months. However the sample at $\phi = 0.1$, initially a dilute fluid phase, slowly sedimented under gravity. After approximately six months, a narrow ($\sim$0.1mm) band of crystals situated 0.6 mm from the base of the cell was observed, which grew very slowly to $\sim$0.5mm after two and a half years. At this time the band constituted over 20% of the sedimented phase, as shown in the photograph in Figure 5.10

Crystallography was performed on the crystallites and the nearest neighbour separation was determined to be $d_{\mathrm{nn}} = 438 \pm 2$nm. By taking the lowest conservative estimate of the volume fraction of these crystals as the monodisperse melting value of $\phi = 0.545$, we find an effective hard sphere radius of 198 ± 1nm. A more realistic, higher estimate of ϕ would only increase the particle radius in the narrow crystal phase. That this value of the radius is 30nm (almost 20%) larger than the mean core radius is evidence that some fractionation has occured to enable the crystal phase to form.

Crystal bands such as these are often observed in reject stock solutions left undisturbed in the laboratory for long periods of time [99–101], but what is different in this case is that both the initial volume fraction and the complete particle size distribution is known. Capitalizing on this additional and extremely useful

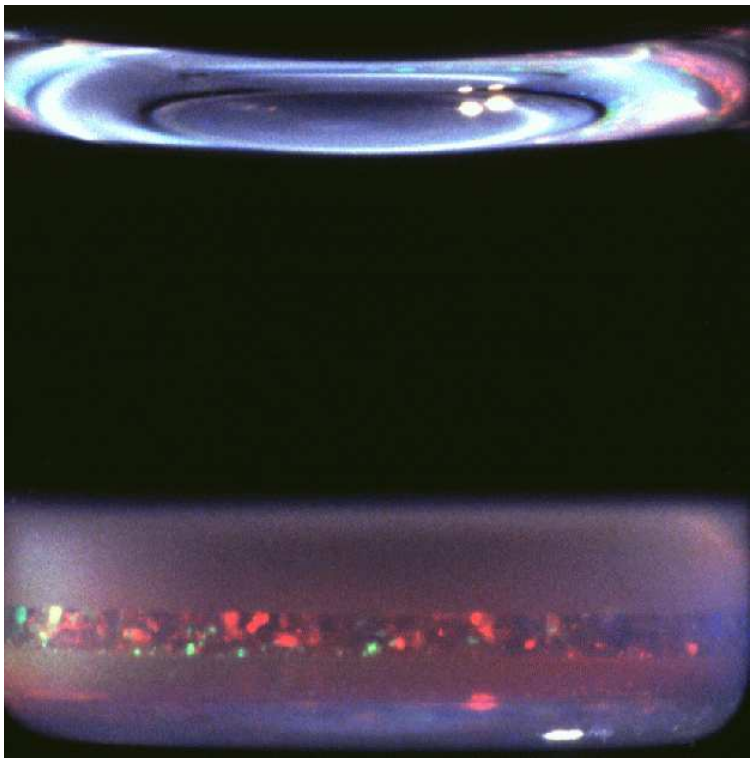

Figure 5.10: Banded crystals due to gravitational settling in Batch E colloid.

information, we have begun computer simulations of non-interacting (no hydrodynamics) sedimenting hard spheres, assuming Stokesian velocities (i.e. $v_{\mathrm{sed}} \propto R^2$). Using the TEM measured PSD for this particular sample, we aim to see whether sufficient fractionation occurs due to sedimentation alone to explain the observed crystalline band, as was found by Janča [59].

5.6 Conclusions

The results from the experiments presented in this chapter allow me to make a few conclusions and predictions about the behaviour of hard sphere suspensions.

- The volume fraction window ($\Delta\phi$) in which a hard-sphere colloidal suspension performs crystal-fluid coexistence narrows only slightly with polydispersity. $\Delta\phi$ decreases from the monodisperse value of 0.051 to ≈ 0.04 at 9.5% polydispersity.
- Fully crystalline samples are not seen above the coexistence gap $\phi > \phi_{\mathrm{m}}$ for $\sigma \approx 9.5\%$. Depending on the particular system, either no crystals (at index match) or a small band of crystals just beneath the meniscus (in *cis*-decalin) are seen. This is attributed to the glass transition preventing homogeneous nucleation.

- My observations do not agree entirely with theoretical works, but share some of the properties of both Bartlett's and Bolhuis & Kofke's predicted phase diagrams. By postulating distinct crystal phases with fractionated distributions, agreement is possible.

- As has been observed previously, the kinetics of crystallisation in polydisperse systems is slowed down. Ripening towards FCC stacking is also retarded by polydispersity.

- Crystal volume fractions ϕ_χ, as determined by crystallography, do not alter as a sample is diluted through the coexistence region.

- Gravity plays an important rôle in determining fractionation. At normal gravity, a ϕ gradient is observed through the sample, which, as expected, is not seen in the time-averaged zero gravity case. In zero-gravity, slight fractionation of particle sizes is seen, with large particles found preferentially in the upper crystal phases.

- Shearing can dramatically aid crystallisation.

- Theoretical polydisperse hard-sphere phase diagrams can be calculated using simple, analytic free energy equations, and solving the equilibrium conditions assuming equal polydispersities in both phases. The agreement with the mean field approach of Bartlett is encouraging.

Having studied polydispersity in hard-spheres, a logical next step would be to look at particles interacting via other potentials. In the next chapter I consider spherical particles which have short ranged attractive forces.

Chapter 6

Observations II: Colloid with Small Polymer

6.1 Introduction

As we saw in Section 2.3.4 the addition of non-adsorbing polymer coils to a suspension of colloidal particles induces an attractive interaction via the depletion mechanism. Such an interaction alters the hard-sphere phase behaviour by widening the ϕ range in which crystal-fluid coexistence is observed. The volume fraction of the coexistence crystal (ϕ_χ) increases as more polymer is added, and may eventually reach the maximum volume fraction which can be tolerated for the particular polydispersity of the system given. In this chapter I aim to determine experimentally if the addition of small size ratio random coil polymer helps or hinders the formation of a colloidal crystal of significantly polydisperse hard spheres. I will also compare my findings with theoretically generated phase diagrams.

6.2 Experimental Procedure

Batch D colloid, of mean radius 300nm and polydispersity of 9.5% was used for these experiments. It was characterised as discussed in Section 4.5.4 and the volume fraction calibrated by the spinning down technique. Dilutions were calculated taking account of the solvated layer by using the previously determined value of $\beta = 0.13$. Polymer of molecular weight $M_\mathrm{w} = 629,500$ and $M_\mathrm{w}/M_\mathrm{n} = 1.03$ was dissolved in *cis*-decalin. This gives $r_\mathrm{g}^\theta = 21.9$nm. At ambient laboratory temperature ($T = 22°$C) the interaction parameter obtained from Berry's data (Figure 12 in [43]) is $z = 0.20$, which results in a slightly swollen radius of gyration of $r_\mathrm{g} = 23$nm, giving a mean size ratio of $\bar{\xi} = 0.077$, with a polydispersity of $\sigma_{r_\mathrm{g}} \approx 9\%$.

Colloid-polymer samples V, W, X and Y were prepared in $4cm^3$ square based cells, at initial colloid volume fractions of 0.4, 0.3, 0.2 and 0.1 respectively. Samples were homogenised by steady tumbling for two days and then clamped into a sample holder and periodically observed over the course of two weeks. At the end of this time, the samples were diluted with pure *cis*-decalin and the process repeated four times. Sample V was mixed with colloid stock solution at $\phi = 0.58$ rather than *cis*-decalin at each dilution. The phase behaviour of each sample was determined by regular visual observations.

6.3 Observations and Results

The observed phase behaviour of the four samples is recorded in Figure 6.1. The samples indicated by solid diamonds separated into two amorphous-looking phases within a few hours of being removed from the tumbler and left undisturbed. The interfaces were observed to fall and sharpen with time, reaching an equilibrium height within one week. This height, as a percentage of total sample height, is indicated by the number adjacent to each symbol. After the second dilution a simple small angle light scattering (SALS) apparatus (consisting of a low powered laser, a sheet of white paper, a hand lens and a darkened room) was used to observe fluctuations of the forward scattered speckles. Both upper and lower phases in all cases were seen to have fluctuating speckle patterns, a clear sign of particle motion. This observation, and the trend in the fractional heights which appear to satisfy the lever rule (Equation 2.1), are consistent with a gas-liquid phase separation, and not transient gelation. After three dilutions, samples W, X and Y no longer showed any sign of gas-liquid phase separation. They remained in a single, stable fluid phase for over a week before signs of sedimentation became apparent: a clear supernatant was visible at the top of the sample, and in some cases a very slow build up of sedimented crystals at the bottom of the sample. Owing to the large time delay before these crystals were observed, and the fact that they were never seen in the bulk of the sample, we attribute them solely to the influence of gravity.

Sample V which was repeatedly mixed with concentrated colloid stock solution, showed stable fluid behaviour at $\phi \approx 0.45$, but above $\phi \approx 0.5$ crystals were evident on the walls and in the bulk of the sample. Over time these crystallites sedimented and formed a growing crystal phase at the bottom of the sample. Beneath the crystal phase was a thin layer ($\sim$ 1mm) of dense amorphous sediment, similar to that observed in the hard sphere experiments discussed earlier. These crystallizing samples are marked by open circles in Figure 6.1, with an accompanying percentage indicating the amount of the crystal phase.

Also included on Figure 6.1 are the experimental hard-sphere points for Batch D in *cis*-decalin determined in the previous section. The phase boundaries are drawn in as guides to the eye.

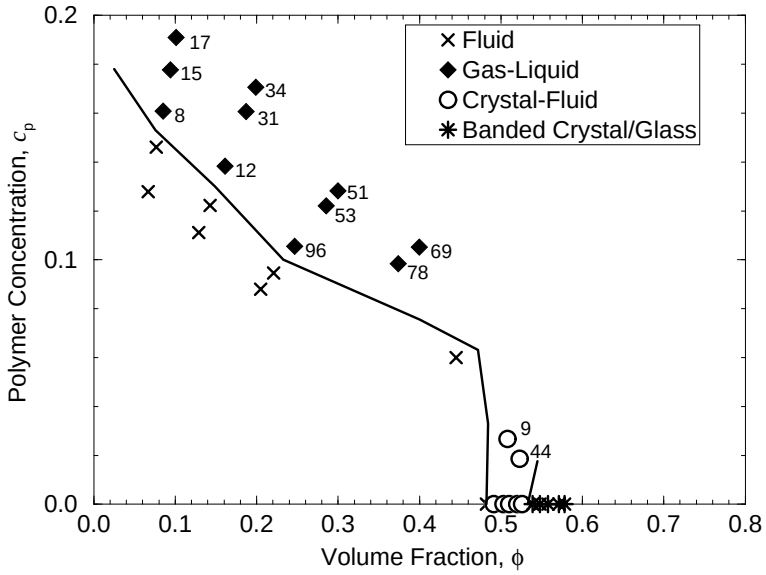

Figure 6.1: Experimental phase diagram for $\xi \approx 0.08$, $\sigma \approx 10\%$ colloid-polymer mixture. The numbers adjacent to each symbol indicate the height of the lower phase, as a percentage of the overall sample height.

6.4 Discussion

In Figure 6.2 the predicted phase behaviour for the monodisperse reference system is plotted. This is calculated using a standard procedure outlined in Section 2.3.4. The cell free energy discussed in the previous chapter is used for the crystal [13], a Padé approximant for the fluid [10] and the polymer is modelled as an ideal solution constrained to move in the free volume, rather that in the entire sample volume. This theoretical phase diagram is in agreement with observations of colloid-polymer mixtures [102], where the colloid polydispersity is approximately 5%. Crystal-fluid coexistence is observed over the substantial region of phase space sandwiched between the metastable gas-liquid boundary (dashed line) and the crystal-fluid boundary (solid line). However for the 10% polydisperse case studied here, crystallization was found to be limited to a much smaller region of phase space. We can therefore answer the question we set ourselves in the previous section: the addition of polymer does *not* aid crystallization, but hinders it. We now proceed to explain why this happens, in terms of the stability of a polydisperse crystal and then using an extension to the polydisperse cell crystal free energy used in the previous chapter.

Crystal Stability Argument

In a hard-sphere colloidal crystal containing particles of equal radius R, the lattice can be uniformly squeezed until each particle makes contact with its

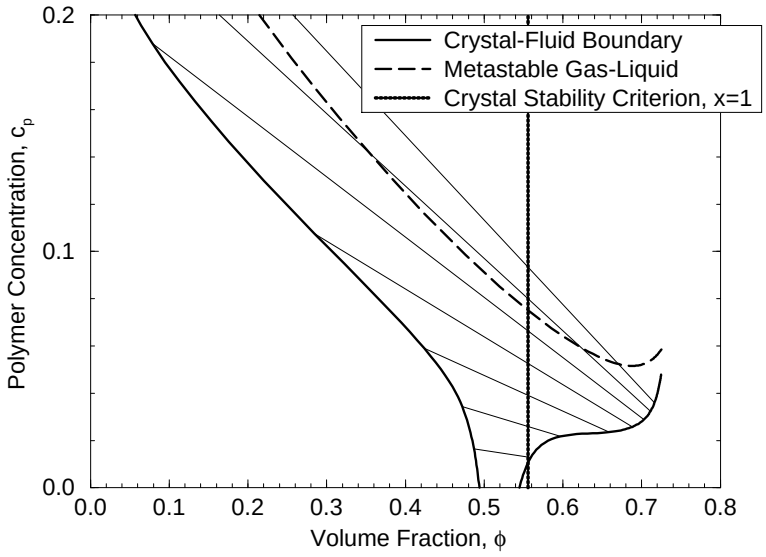

Figure 6.2: Theoretical phase diagram for a monodisperse mixture with R=300nm and $r_g = 23$nm. A vertical line corresponding to the maximum crystal volume fraction for hard spheres with polydispersity of 10% is plotted. See text for more details.

nearest neighbours, at which point the nearest neighbour distance is $d_{nn} = 2R$ and the volume fraction is given by the theoretical close packing of spheres, $\phi_{cp} = \pi/(3\sqrt{2}) \approx 0.74$. For more spacious lattices, the volume fraction is less than this value and given by

$$\phi = \phi_{cp} \left[\frac{2R}{d_{nn}}\right]^3. \tag{6.1}$$

If the particles are polydispersed, particles of a certain size (with a radius R_l greater than the mean radius $\bar{R}$) will make contact with each other at a larger lattice size, when

$$d_{nn}/2 = R_l > \bar{R}. \tag{6.2}$$

By writing this large particle size as being x standard deviations larger than the mean, $R_l = \bar{R}(1 + x\sigma)$, the contact condition becomes

$$d_{nn}/2 = \bar{R}(1 + x\sigma). \tag{6.3}$$

For d_{nn} greater than this value only particles larger than R_l will be touching, and we say the crystal is stable. For smaller d_{nn}, all neighbouring particles with radius greater or equal to R_l are touching and disrupt the formation of the crystal. Obviously, the choice of R_l is somewhat arbitrary: Pusey [94] chose $x = 1$, equivalent to "disruption size particles" of one standard deviation larger than the mean. As $d_{nn} > 2\bar{R}(1 + x\sigma)$ for the crystal to be stable, we can substitute this into Equation 6.1 to deduce a restriction on the volume fraction of a stable crystal at a given polydispersity:

$$\phi = \phi_{cp} \left[\frac{2R}{d_{nn}}\right]^3 < \frac{\phi_{cp}}{(1 + x\sigma)^3}. \tag{6.4}$$

The value of x specifies how much of the high tail of the distribution (in units of the standard deviation) we allow to be incorporated into the crystal phase (Figure 6.3). For a Gaussian PSD, $x = 1$ corresponds to allowing 16% of the particles to have $R > d_{\mathrm{nn}}/2$ and therefore be large enough to disrupt the lattice. For a rectangular PSD, $x = 1$ corresponds to 21% of the distribution, and $x = \sqrt{3} \approx 1.732$ enforces that no particles are overlapping.

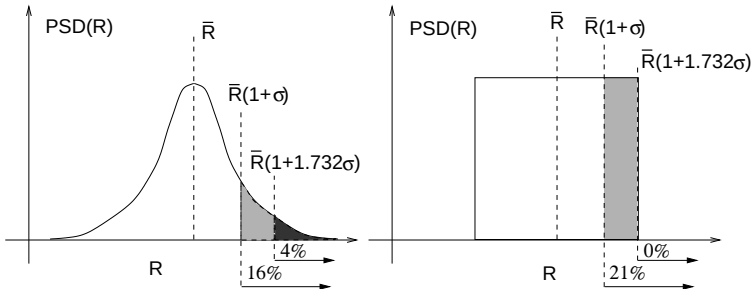

Figure 6.3: The significance of the arbitrary constant x for Gaussian and rectangular particle size distributions. The grey shaded regions indicate the fraction of the PSD we permit to disrupt the lattice when $x = 1$. The region shaded black is the fraction when $x = \sqrt{3}$.

Rearranging this equation, we find an expression for the polydispersity at which a crystal with a certain ϕ becomes unstable:

$$x\sigma = \left[\frac{\phi_{\mathrm{cp}}}{\phi}\right]^{\frac{1}{3}} - 1. \tag{6.5}$$

Pusey argued that an estimate of the terminal polydispersity could be found by applying this condition at the lowest possible density for a crystal, $\phi_{\mathrm{m}} = 0.545$: he found a value of $\sigma_{\mathrm{T}} \approx 11\%$. However, we can use this formula to find the maximum density of a crystal for any given polydispersity. Precisely such a relationship between polydispersity and crystal volume fraction is contained in the cell free energy. As this approach considers a particle surrounded by average particles (the mean field approximation), the value of x is less than 1, $x = \sqrt{3}/2 \approx 0.866$. In the simulations of B&K, they call this maximum packing the infinite pressure limit.

This crystal stability argument can be used to heuristically explain why crystals were only seen in colloid-polymer mixtures close to the zero-polymer, hard-sphere coexistence region. As low polydispersity ($\sigma \approx 5\%$) crystals, in coexistence with a more dilute fluid phase, have been measured with volume fractions above the glass transition ($\phi_{\mathrm{gt}} \approx 0.58$), even as high as $\phi_{\chi} = 0.615$ [102], we can assume that a glass transition is not responsible for preventing a crystalline phase from developing in samples W, X and Y. I therefore hypothesise that these samples do not crystallize because ϕ of the expected crystal phase exceeds the maximum permitted by the crystal stability criterion for 10% polydisperse hard spheres (using a value of $x = 1$) of $\phi_{\chi} \lesssim 0.556$. On the theoretical monodisperse phase

diagram plotted in Figure 6.2, I have added a vertical line corresponding to this terminal crystal density. Any tie lines which cross this line, connect an unstable crystal phase to a fluid, and we do not expect these samples to crystallize. From the diagram it is clear that only samples with polymer concentrations below $c_p \approx 0.02$, will be able to form crystals of tolerably low volume fraction. For the experiments, this condition is only satisfied for sample V with low concentrations of polymer, and indeed, this is when crystals were observed.

6.4.1 Cell Free Energy Calculation

A more sophisticated, but related, argument, can also be used to actually calculate the phase diagram of a polydisperse colloid-polymer mixture. By replacing the crystal free energy used in calculating the monodisperse phase diagram with the cell theory free energy, proposed by Sear [13], the common tangent construction can again be solved to determine phase boundaries [103]. In so doing, I assume that no fractionation occurs between any of the phases and that the monodisperse form of the fluid free energy, plus a term to account for the entropy of mixing is still an appropriate expression to use. This results in the gas-liquid binodal being unaffected by polydispersity. Neither of these assumptions are entirely valid, and more accurate theoretical forms could have been used, but in the context of this exploratory work, I am more concerned with predicting general trends than exactly reproducing experimental phase boundaries.

Although the experimental sample has $\sigma = 10\%$, the cell-model has a terminal polydispersity below this, $\sigma_T \approx 8.5\%$ so I used $\sigma = 8\%$ for the calculations. The predicted hard sphere behaviour at this polydispersity includes a re-entrant fluid phase at sufficiently high colloid volume fractions—whether this phenomenon will ever be observed experimentally is a separate issue, complicated by the presence of the glass transition and consequently the very slow approach to equilibrium. I have therefore decided to leave the re-entrant behaviour out of the predicted phase diagram shown in Figure 6.4. To produce good agreement with the experimental points, the theoretical curves have been scaled slightly along both axes, ϕ by 0.93 and c_p by 0.63. The monodisperse crystal-fluid boundary is drawn as a dot-dashed curve. The dashed curve is the gas-liquid binodal which we assume to be unaltered by polydispersity. The solid curves mark the boundary of crystal-fluid coexistence for the $\sigma = 8\%$ case: only samples between these two lines and beneath the dashed gas-liquid binodal, will show crystal-fluid coexistence. The remaining regions of phase space are either gas-liquid (above the dashed line) or stable fluid at lower polymer concentrations. Theoretical tie-lines are drawn indicated between gas and liquid phases.

The agreement between data points and theoretical predictions, even taking account of the slight scaling of the theoretical curves, is surprisingly good.

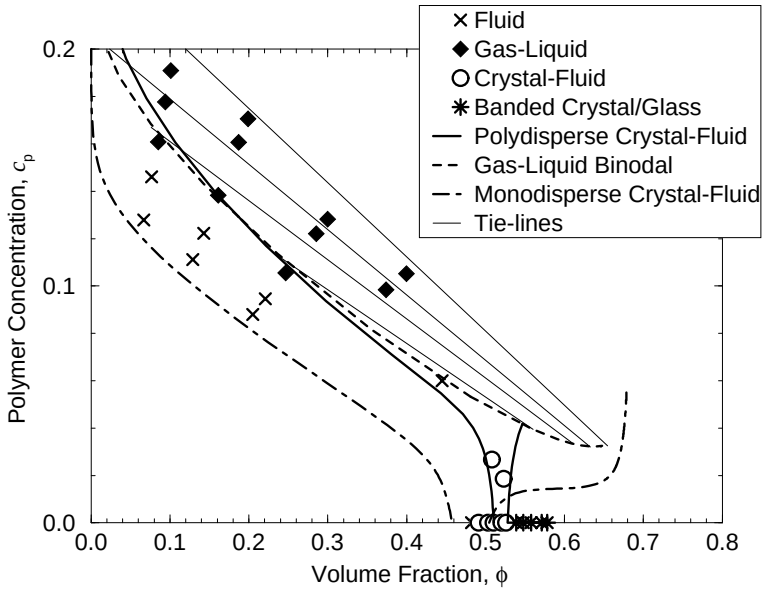

Figure 6.4: Experimental data points and theoretical polydisperse phase boundaries for $\xi = 0.077$ and $\sigma = 8\%$. Theoretical tie-lines between gas and liquid phases are also plotted. The theoretical results come from solving the cell free energy in the standard monodisperse hard-sphere fluid plus polymer model. Theoretical values of ϕ are scaled by 0.93 and $c_{\rm p}$ by 0.63.

6.5 Conclusions

In this chapter I have presented results of an experimental study of the effects of colloidal polydispersity on the phase behaviour of a mixture of colloids and relatively small random coil polymers. This polymer solution induces a well documented attractive depletion potential between colloidal particles. The net effect of this interaction was anticipated, based on previous monodisperse investigations, to aid the crystallization of the sample and expand the region in which fluid-crystal coexistence was seen. However, this was not observed. Crystallization was in-fact suppressed. It is proposed that, due to the osmotic pressure of the polymer solution, the crystal phase is forced to develop at higher volume fractions than usual. In the monodisperse case, this has been observed up to $\phi \approx 0.615$, but an idea of Pusey's, based on the Lindemann melting criterion, indicates that for polydisperse particles these higher volume fraction crystals will be disrupted by variations in particle sizes. This crystal stability idea is also encapsulated in the cell theory of solids, which has been successfully applied to hard sphere systems. Using this theory we have produced a phase diagram which, with slight scaling of the axes, agrees very well with our observations. Further predictions including the possibility of a re-entrant fluid phase and a triple point at which a crystal phase is seen between an equilibrium gas and this re-entrant liquid phase, have yet to be observed, and will probably be masked by the glass transition.

Continuing in the vein of investigations presented here, the next chapter also deals with the study of a colloid-polymer mixture, in which both the colloidal polydispersity and the relative size of the polymer are increased.

Chapter 7

Observations III: Colloid with Large Polymer

7.1 Introduction

In Chapters 5 and 6 I described how polydispersity affects the behaviour of colloids with zero and short range effective interactions ($\xi \lesssim 20\%$). In this chapter I present experimental work on the influence of polydispersity on a system where the effective particle interaction is relatively long-ranged ($\xi \gtrsim 50\%$). The phenomena we are expecting to observe include suppression of crystallisation, fractionation between coexisting phases, shifting of phase boundaries and retardation of phase separation kinetics.

7.2 Experimental Procedure

The colloid used for the majority of experiments in this section was Batch E. As outlined in Section 4.5.5, the average radius and polydispersity of these particles, as determined by TEM were 167nm and 18.1% respectively. A stock solution was washed and its volume fraction calibrated. As polydispersity suppresses the hard-sphere crystallisation of these particles, the factor β used in converting core to hard-sphere volume fractions (see Equation 4.7 for the definition) was determined by comparing ϕ determined from evaporation and by spinning down. The volume fraction of the spun down RCP sediment is assumed to be $\phi_{\mathrm{rcp}} = 0.68$, the simulation value quoted in [47] for samples with $15\% < \sigma < 20\%$. The core volume fraction ϕ_{c} measured by evaporation of such an RCP sediment was $\phi_{\mathrm{c}} = 0.581 \pm 0.005$. This gives a value of $\beta = 0.128 \pm 0.008$, and a corresponding hard sphere radius $R_{\mathrm{HS}} = 176 \pm 2$nm. This value of β was used for calculating all subsequent dilutions of the stock sample. Throughout this work I have used the TEM-determined core radius to characterise the particles, although the particles

behave as though they are hard-spheres of slightly larger radius ($\approx 5\%$). This is because the TEM value was determined directly, to less than 1% uncertainty and introduces no other assumptions or associated errors. Also, this small change will not alter the interpretation of the predominantly qualitative results, or the general agreement with theoretical predictions.

For a quasi-monodisperse comparison, Stock B was used which has $\bar{R} = 190 \pm 6$nm and $\sigma \approx 6\%$. Although the quoted radius is slightly larger than for Stock E, the radii determined by SLS are comparable (185 and 190 nm).

A stock solution of random coil polystyrene was prepared by the method outlined on page 50. The mass averaged molecular weight for this polymer is $M_{\rm w} = 6.85 \times 10^6$ and the polydispersity ratio is $M_{\rm w}/M_{\rm n} = 1.06$. I used data from Berry [43] to convert these manufacturer's quoted values into useful polymer parameters: the radius at the theta temperature T_θ is given by $r_{\rm g}^\theta = 0.0276\sqrt{M_{\rm w}} = 72.2$nm. In *cis*-decalin at ambient laboratory temperature ($20 \pm 2^\circ$), the Fixman parameter $z = 0.86$ and the expanded radius of gyration of these coils is $r_{\rm g} \approx 83$nm with a polydispersity of $\sigma_{r_{\rm g}} \approx 12\%$. The effects of polymer polydispersity on the value of $r_{\rm g}$ and on colloid-polymer phase behaviour are discussed in Sections 4.1.2 and 3.3.3 respectively. Values of $c_{\rm p}$ are always quoted as percentages of the overlap concentration at T_θ, $c^* \approx 7.2$ mg.cm^{-3} (see note on page 52 for definition of overlap concentration). The size ratio parameter ξ, which determines the expected phase behaviour, has an average value of $\xi \approx 0.50$. For interactions of this range in a monodisperse system, we expect a three phase coexistence region and a well defined gas-liquid critical point.

Following the procedures detailed in Section 4.1.3, I prepared samples containing mixtures of the stock colloid and polymer in 2cm^3 cylindrical cells across a wide range of initial colloidal volume fractions and polymer concentrations $(\phi_{\rm i}, c_{\rm p_i})$. After homogenisation by steady tumbling for two days the samples were left for several weeks to equilibrate. During this period phases were observed emerging and the heights of the interfaces between them measured with vernier callipers at regular intervals. After two weeks, samples were assumed to have reached "thermal" equilibrium and any subsequent changes were due only to gravitational sedimentation. Seven samples which at this time showed no separation were allowed to evaporate slowly until a second, shadow, phase emerged. As these samples are presumed to be just across the cloud-point curve (equivalent to a shallow quench) I will refer to them from now on as cloud-point samples.

To gain insight into the nature of the phase separation, I performed basic dynamic light scattering and microscopy on some of the coexistence samples. Many samples were manually separated into individual coexistence phases by the technique described on page 54. The volume fractions of the coexistence phases were determined by spinning down, and by weight loss evaporation, and the radii and polydispersities of the phases were measured by performing SLS on diluted samples. The particles in two of these separated samples were analysed by TEM.

To compare directly kinetics in poly- and monodisperse systems, two samples were prepared in square based 4cm^3 cuvettes at $\phi_{\rm i} = 0.2, c_{\rm p_i} = 52\%$, one containing polydisperse Batch E particles, the other 'quasi-monodisperse' Batch B particles. Both were mixed with the stock polymer solution prepared above. The samples, after thorough homogenisation, were left undisturbed in a temperature controlled water bath at 22°C, and the sedimentation was followed by use of time-lapse video recording. Equilibrium having been reached, both samples were slightly diluted, with stock solutions of $\phi = 0.2$, thereby reducing only the polymer concentration. The homogenisation and video recording were repeated at five different values of $c_{\rm p}$.

7.3 Observations and Discussions

7.3.1 Sedimentation Profiles and Phase Behaviour

Sedimentation profiles for six initial volume fractions and a range of polymer concentrations are presented in Figure 7.1. Certain trends are present in all graphs.

Single Phase Fluids

At low polymer concentrations, samples show no developing interface over the course of the observations. They remain homogeneous and in a single phase for many weeks. Eventually, clear solvent is visible below the meniscus, due to the gravitational settling of the particles, most noticeably in the more dilute colloidal samples.* We call these samples 'Colloidal Fluids' in analogy with previous monodisperse observations (see for example [102]). These sedimentation profiles are plotted as lines (solid or dashed) without symbols in Figure 7.1 and the corresponding phase points are marked by open circles on the phase diagram in Figure 7.2.

Gas-Liquid Coexistence and Transient Gelation

In monodisperse systems there is a clear distinction between samples which separate into two ergodic phases (gas-liquid separation) and those which undergo gelation. From early times, gas-liquid samples show evidence of an interface dividing the lower ergodic fluid phase from the upper phase, a dilute colloidal gas.

*This observation is in qualitative accord with the theoretical results for the sedimentation of hard-spheres [60, 104] which predicts that the scaled sedimentation velocity $v(\phi)/v_0$ (where v_0 is the dilute stokes velocity defined in Equation 4.3) should decrease with volume fraction as $(1-\phi)^{6.55}$.

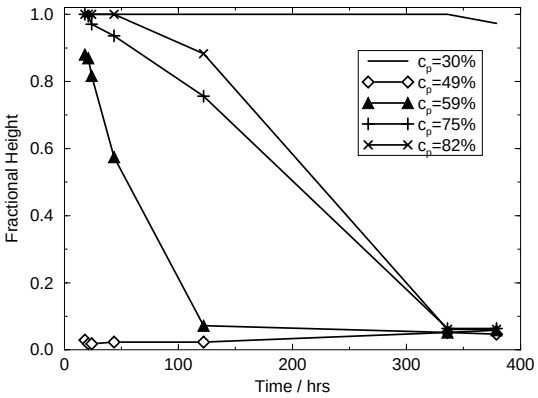

a) Volume Fraction $\phi = 1.0\%$

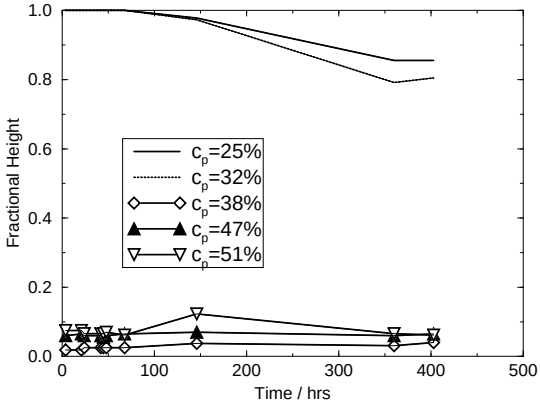

b) Volume Fraction $\phi = 2.5\%$

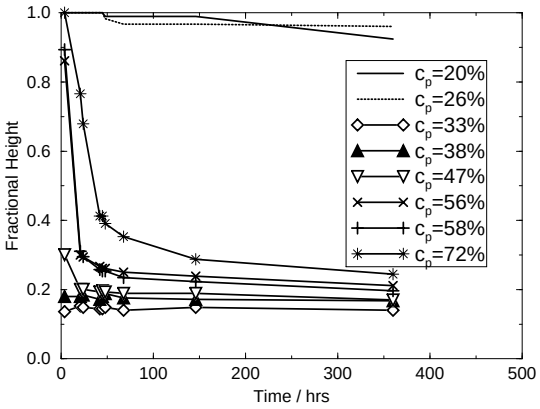

c) Volume Fraction $\phi = 10\%$

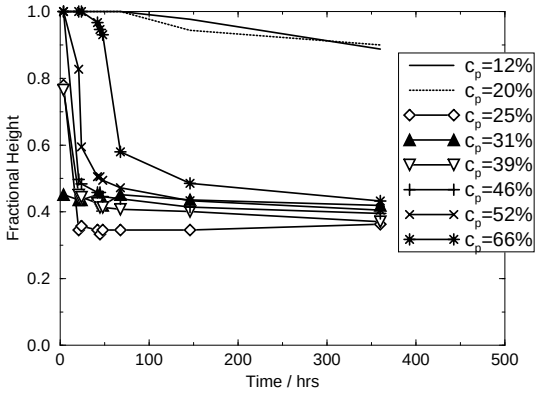

d) Volume Fraction $\phi = 20\%$

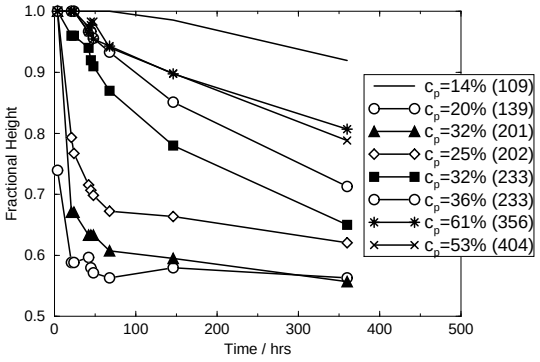

e) Volume Fraction $\phi = 30\%$

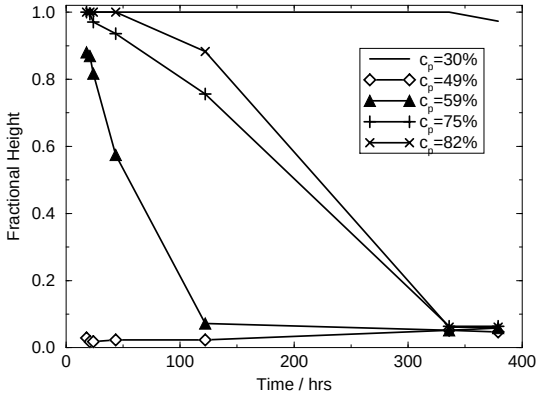

f) Volume Fraction $\phi = 35\%$

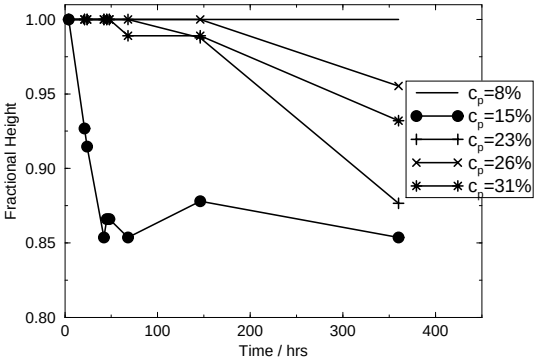

g) Volume Fraction $\phi = 40\%$

Figure 7.1: Sedimentation profiles for 7 different volume fractions. The concentration of polymer ($c_{\rm p}$) for each curve is quoted in the legend. Samples in Graph (e) cover a range of volume fractions between 29% and 32% so an estimate of the polymer concentration in the free volume is given in brackets after the usual $c_{\rm p}$ value.

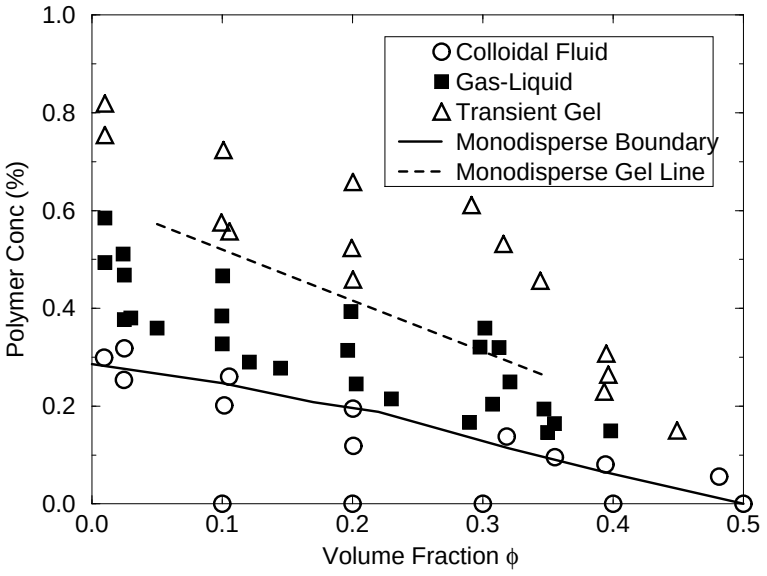

Figure 7.2: Experimental phase diagram for Batch E colloid and $r_{\rm g} \approx 82$nm polymer coils. The size ratio is $\xi = 0.50$ and the colloidal polydispersity is $\sigma = 18\%$

A transient gel differs on two counts. Firstly, there is an appreciable (∼hours) delay time, τ until an interface is first observed, during which time all particles throughout the sample are stuck in a system-spanning network. Secondly, when the gel collapses under its own weight, and an interface is finally seen, the upper phase is free of particles, a clear supernatant.

However, for this polydisperse system the distinction appears blurred. All samples with sufficient concentration of polymer eventually develop an interface between a colloid-rich lower phase and an upper phase. Depending on the precise value of the initial polymer concentration, the upper phase varies continuously between a gas phase clearly containing particles (at lower $c_{\rm p}$) and a particle-free supernatant (at higher $c_{\rm p}$), with no obvious discontinuity at the gel line. The delay time τ required until the interface becomes apparent is also dependent on the polymer concentration, increasing smoothly with higher $c_{\rm p}$.

To aid classification, elementary dynamic light scattering was performed on these separating samples by illuminating them with a low power laser and observing the speckle pattern by eye. Non-clear upper phases showed a rapidly fluctuating pattern which was similar to the scattering from a pure dilute colloidal suspension. This is verification of the gas-like behaviour of the upper phases. The lower phases were often too small to be illuminated even by a focused laser beam, and suffered from the problems of multiple scattering. Nevertheless, the speckle patterns for the lower phases from samples just across the boundary typically showed slow dynamics of speckle patterns, similar to those observed in concentrated colloidal fluids without polymer. At higher concentrations some evidence for frozen behaviour was observed. Very preliminary DLS experiments, kindly performed by Dr.A.Moussaïd on these samples, showed that time averaged intensities varied

between different scattering volumes, implying that temporal and ensemble averaging is not equivalent. However, the upper phases of these non-ergodic gel-like samples clearly contained particles. Light microscopy of the higher c_{p} samples also revealed clusters and branches, with some particles freely diffusing between the larger structures. Owing to the small radii of the particles and the resolution of the microscope, it was impossible to differentiate particle sizes.

The two observations which are useful for characterising gels lead to gel lines at different positions for this polydisperse system. Clear supernatants are first seen at greater values of c_{p} than when non-ergodicity and evidence of a delay time is first observed. As a compromise I decided to classify samples as Transient Gels when their delay time was greater than 4 hours. These are plotted on the phase diagram as open triangles and on the sedimentation profiles as crosses or stars connected by solid lines. Samples with $\tau < 4$ hrs were deemed not to be gels, but labelled as two phase samples because the upper phases clearly contained particles. In analogy with monodisperse experiments, we call these 'Gas-Liquid', which although accurate for those just across the phase boundary, may not be the correct classification for samples nearer the gel-line. These samples are indicated by symbols (circles, squares, etc.) connected by solid lines in Figure 7.1 and by dark squares in Figure 7.2.

The trend of Fluid to Gas-Liquid to Transient Gel for increasing values of c_{p} holds for all Graphs in Figure 7.1 except (e). However, these samples were not all prepared at exactly $\phi = 0.3$, but over a range between 0.29 and 0.31. This small change in volume fraction makes a significant difference to the free volume available to the polymer coils in the different samples. To offset this, I have quoted polymer concentrations in the free volume ($c_{\mathrm{p}}^{(\mathrm{free})} = c_{\mathrm{p}}/\alpha$) in brackets after the experimental c_{p} value. As discussed on page 18, α is strongly dependent on the size ratio and the volume fraction and is defined as the ratio of the free volume V_{free} to the total sample volume V_{T}. This scaled polymer concentration is proportional to the polymer activity and is theoretically a more sensible quantity to quote, although it is not used experimentally as it cannot be measured directly but must always be calculated by using approximate theoretical results (derived from scaled particle theory in this case). Reassuringly, the trend observed in the other six cases for increasing c_{p} is recovered for (e) for increasing $c_{\mathrm{p}}^{(\mathrm{free})}$.

Perhaps surprisingly, the quoted values of $c_{\mathrm{p}}^{(\mathrm{free})}$ are greater than 100% which means that the coils overlap. However, the uncertainties in colloid size and absolute volume fraction, the temperature dependence of the polymer radius of gyration r_{g}, the use of radius of gyration (as opposed to other possible radii) in calculating the overlap concentration and the effect of these uncertainties on the function α, mean that we should only use the scaled concentration values as indicative of a trend, rather than taking the numbers at face value.

Monodisperse comparison

Throughout the observations across the entire phase diagram, crystals were never seen. As discussed in Section 3.3.3 and in Chapter 5, this is because the crystalline phase is disrupted by excessive variations in particle sizes, despite the possibility of size and particle fractionation between phases. In quasi-monodisperse reference experiments (in which $\sigma \approx 5\%$ [102, 105, 106]) crystal-fluid, crystal-gas and three phase coexistence were observed. Although the existence of these extra phases complicates such a reference system, it is possible to estimate the polydisperse behaviour from the monodisperse phase diagram. By disregarding the crystal branch of the free energy, all boundaries with crystalline phases are removed from the phase diagram. All that remains is the gas-liquid coexistence curve, the metastable sections of which become stable when the possibility of a crystal phase is removed (see Section 2.3.4).

In Figure 7.2, the quasi-monodisperse reference boundary is included. For $0 < \phi \lesssim 0.4$ this is the gas-liquid boundary and above $\phi \approx 0.4$ it corresponds to the fluid-crystal boundary. Within experimental uncertainties, the gas-liquid section is in agreement with my experimental points, so any shift in the boundary caused by polydispersity is smaller than experimental uncertainties ($\approx 5\%$). Alternatively, we can say that the stability of this system sample is neither increased nor decreased by altering the polydispersity from 5% to 20%.

The monodisperse gel line is also plotted on Figure 7.2 and again, the agreement between the two systems is within uncertainties, especially considering the somewhat arbitrary nature of the polydisperse gel line.

7.3.2 Coexistence Samples and Fractionation

Measurements on Coexistence Samples

The manually separated samples permit direct measurement of two interesting properties: the volume fractions and the degree of fractionation (difference in mean radius and polydispersity) in coexisting samples. Table 7.1 gives initial ($\phi_{\rm i}$,$c_{\rm p_i}$) for evaporated cloud curve samples on which coexisting volume fraction and fractionation data were taken. Volume fractions were measured by evaporation, and polymer concentrations as discussed on page 129. Those in Table 7.2 were only analysed for volume fractions, and for completeness Table 7.3 contains the phase coordinates ($\phi_{\rm i}$,$c_{\rm p_i}$) of the remaining samples. The volume fractions of the coexistence phases were determined by centrifuging, and the figures in brackets relate to additional measurements performed by evaporation. For samples where one phase was too small to extract accurately, its volume fraction ϕ_1 was calculated to be consistent with the known value of $\phi_{\rm i}$ and the measured values of ϕ_2 and the relative phase volumes f at time of extraction. Values of mean radius and polydispersity in Table 7.1 were determined by fitting theoretical form

Sample	$\phi_{\rm i}$ (%)	$c_{\rm p_i}$ (%)	Designation	ϕ (%)	$c_{\rm p}$ (%)	$\bar{R}_{\rm SLS}$ (nm)	$\sigma_{\rm SLS}$ (%)
gr25*	3±1	38±1	Gas-	2±1	39±1	170±4	15±3
			Liquid	19±5	18±5	187±1	10.8±0.5
gr20*	4±1	39±1	Gas-	1±1	43±1	170 ±5	17±3
			LIquid	24±3	12±5	184±2	12.1±0.7
g20*	12±1	30±1	Gas-	2±1	38±1	182±2	12.2±0.7
			LIquid	49±5	3±2	184±1	10.8±0.5
g15*	15±1	19±2	Gas-	13±5	31±1	179±2	13±1
			Liquid	30±5	9±3	180±2	13±1
p15*	23±2	22±1	Gas-	2±1	55±5	158±7	20±4
			Liquid	32±7	8±2	180±2	11.7±0.7
p1*	29±2	17±1	Gas-	1±1	60±3	149±10	26±8
			Liquid	38±1	4±1	180±2	11.7±0.7
w1*	35±3	15±1	Gas-	6±3	55±4	170±2	15±1
			Liquid	45±7	2±1	182±1	11.4±0.7

Table 7.1: Summary table of cloud curve samples, which phase separate. The coexisting phases were manually separated and volume fraction and SLS measurements were taken. ϕ was measured by the evaporation technique and the quoted errors include systematic uncertainties for the conversion to effective $\phi_{\rm hs}$, and errors arising from problems during extraction and handling. Polymer concentration was calculated by enforcing equal polymer chemical potential and converting $\mu_{\rm p}$ values to $c_{\rm p}$ values as discussed in the section on tie-lines on page 129. Particle sizes and polydispersities are determined by SLS and the errors are due to the normal fitting difficulties.

Sample	ϕ_{i} (%)	$c_{\mathrm{p_i}}$ (%)	Designation	ϕ (%)	c_{p} (%)
g25	10	33	Gas- Liquid	7 31	36 7
g30	10	38	Gas- Liquid	1 56	45 0
g35	10	47	Gas- Liquid	3 40	57 3
g40	10	56	Tr.Gel	1 49	68 1
g45	10	58	Tr.Gel	1 56	69 1
g50	10	72	Tr.Gel	1 (0) 41 (40)	91 4
p20	20	25	Gas - Liquid	12 (10) 35 (37)	36 5
p25	20	31	Gas- Liquid	11 33	46 9
p30	20	39	Gas- Liquid	1 42	70 2
p35	20	46	Tr.Gel	1 46	78 1
p40	20	52	Tr.Gel	0 (1) 48 (46)	87 1
p45	20	66	Tr.Gel	0 41	123 5

Table 7.2: Summary table for coexistence samples. Values listed were measured by spinning down separated phases, and those in brackets were measured by weight-loss evaporation. Initial values have relative uncertainties of $\sim 5\%$ and fractionation values have relative uncertainties of around 10%.

factors generated from a range of PSDs to measured SLS data.

Coexisting phases from two samples were diluted and allowed to dry on carbon grids in preparation for a direct PSD measurement using the TEM facility. However, the particles aggregated during the drying stage. We presume that this was due to the increasing strength of the depletion potential caused by the polymer becoming more concentrated. Although the such systems are an interesting topic for study in their own right, individual particles in the aggregated clumps proved impossible to measure. For this reason, I was unable to obtain accurate histograms for coexistence phases. I would advise future experimentalists to wash such samples several times to remove the polymer, before preparing TEM grids.

Sample	ϕ_{i} (%)	$c_{\mathrm{p_i}}$ (%)	Designation
wb25	0.9	30	Fluid
wb35	1.0	49	Gas-Liquid
wb45	1.0	59	Gas-Liquid
wb55	1.0	75	Tr.Gel
wb65	1.0	82	Tr.Gel
gr20	2.5	25	Fluid
gr25	2.5	32	Fluid
gr30	2.5	38	Gas-Liquid
gr35	2.5	47	Gas-Liquid
gr40	2.5	51	Gas-Liquid
g15	10	20	Fluid
g20	10	26	Fluid
p10	20	12	Fluid
p15	20	20	Fluid

Sample	ϕ_{i} (%)	$c_{\mathrm{p_i}}$ (%)	Designation
w10	31.8	14	Fluid
w15	30.8	20	Gas-Liquid
w20	32.1	25	Gas-Liquid
w25	29.8	32	Gas-Liquid
br3	31.2	32	Gas-Liquid
br5	30.1	36	Gas-Liquid
w40	31.6	53	Tr.Gel
w30	29.1	61	Tr.Gel
br4	35.5	10	Fluid
br1	35.5	16	Gas-Liquid
br2	34.7	19	Gas-Liquid
w50	34.4	46	Tr.Gel
br8	39.4	8	Fluid
b10	39.8	15	Gas-Liquid
b15	39.3	23	Tr.Gel
b20	39.6	26	Tr.Gel
b25	39.5	31	Tr.Gel
br7	44.9	15	Tr.Gel
br6	48.1	6	Fluid

Table 7.3: Summary table for samples without ϕ measurements. Relative errors are $\sim 5\%$.

Understanding Fractionation

The data in Table 7.1 clearly show that larger, less polydisperse particles are present in the more dense liquid phase. This phenomenon can be understood by noting that the system is not only polydisperse in size but also in *energy* through the particle size dependence of the overlap volume and hence the depletion potential. Figure 7.3 shows how the strength of the depletion potential at $c_{\mathrm{p}}^{(\mathrm{free})} = 0.1$ varies with separation for three particle sizes, the mean (167nm) and

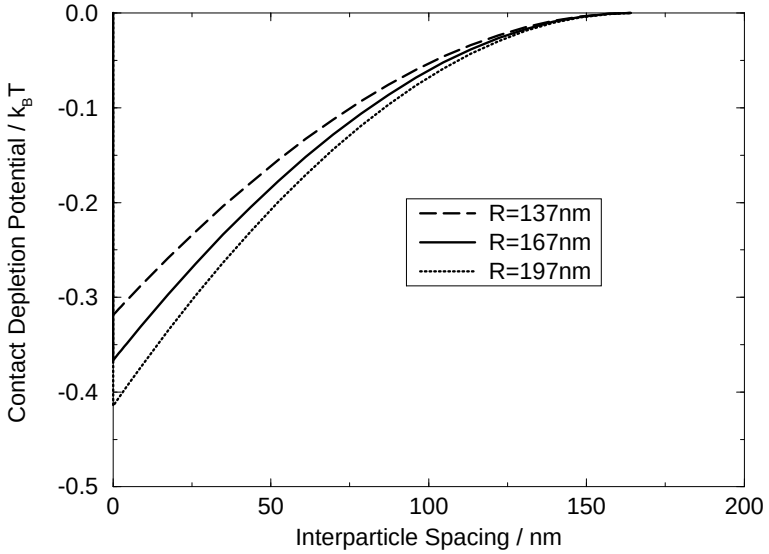

Figure 7.3: Depletion potentials between particles of radii 137, 167 and 197nm. The polymer size in all cases is $r_g = 82$nm and $c_p^{(free)} = 0.1$. At all separations, the larger particles experience a stronger attractive potential.

one standard deviation either side (137 and 197nm). The larger particles clearly experience a stronger attractive force. Mathematically, the value of the potential at contact, for two spheres of radius R and polymer of radius r_g is given by

$$\frac{U_{\rm dep}}{k_{\rm B}T} = c_{\rm p}^{(\rm free)} \left(1 + \frac{3}{2}\frac{R}{r_{\rm g}}\right). \tag{7.1}$$

If the spheres have unequal radii R_1 and R_2, then the harmonic mean $R_{\rm h} = (2R_1R_2)/(R_1 + R_2)$ replaces R in Equation 7.1. Larger particles in the sample will experience a stronger attractive potential than smaller ones, and the system can lower its energy by partitioning so that the larger particles are closer together: in the denser phases.

This simple argument can also explain the gradual transition between Gas-Liquid and Transient Gel samples. In a monodisperse sample, just across the gel transition boundary, the depletion potential between *all* the particles is sufficient to cause clustering. However, if there is a distribution of sizes, this boundary is smeared out, and by increasing $c_{\rm p}$, progressively smaller particles will have sufficiently deep potentials to be incorporated into clustered or gel-like structures.

Following the arguments of Bibette in [48,49] we consider the polydisperse system to be composed of three distinct size populations, with radii equal to 137, 167 and 197nm as mentioned previously. Assuming naïvely that each pure species independently undergoes its own phase transition, we have overlaid theoretical phase boundaries (calculated using code written by Dr.P.Warren [103], based on the theory of Lekkerkerker *et al.* [22] which I review in Section2.3.4) for mixtures of these three particle sizes with the $r_g = 82$nm polymer. (See Figure 7.4.)

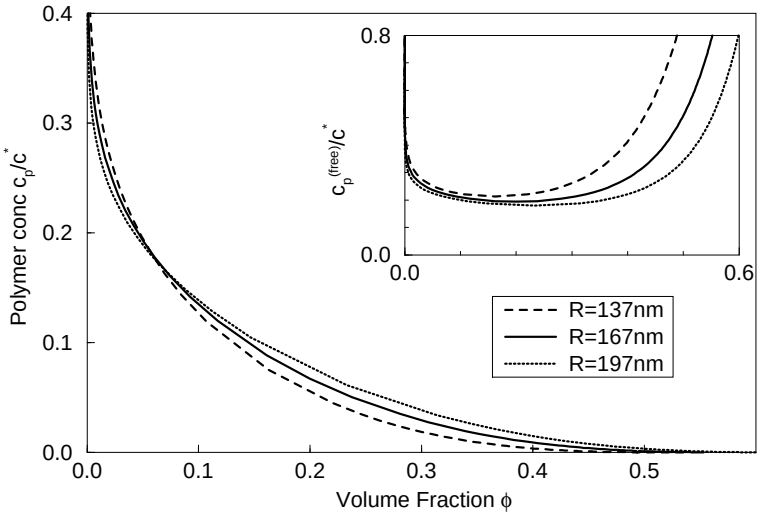

Figure 7.4: Theoretical phase boundaries for the mean radius particles (R=167nm) and for one standard deviation either side (137 and 197nm). The polymer size in all three cases is $r_g = 82$nm. The larger particles will always be found in the denser phase. The inset shows the same data plotted against the polymer concentration in the free volume $c_p^{(free)}$. In this case, the larger particles are always in the minority phase. See text for discussion.

The first point to note is that the maximum deviation between curves is approximately $0.02c^*$, which corresponds to an experimentally imperceptible shift in phase boundaries. The second point will give us insight into fractionation and illuminates a crucial difference between the two different polymer concentration representations, corresponding to two methods (only one physically realisable) of performing the experiment. In the main plot, where the vertical axis is the experimental parameter c_p, the denser phase will be enhanced with larger particles. At low values of ϕ the 197nm system becomes unstable at lower values of c_p and these larger particles will be ejected into the more dense minority phase. At larger values of ϕ the situation is reversed and the incipient, less-dense phase will preferentially contain the smaller particles. This prediction is in agreement with observations and the previous discussion on size dependent depletion potentials.

The inset, where the vertical axis is $c_p^{(free)}$, corresponds to a Gedanken experiment where the polymer chemical potential is fixed. The number of polymers is therefore permitted to fluctuate, and this could ideally be achieved by use of a semi-permeable membrane separating the sample from a polymer reservoir. In this situation, the 197nm particles phase separate at a lower value of c_p for all values of ϕ and these larger particles will always be ejected into the minority phase. So for experiments above the critical density ($\phi \approx 0.25$), when the minority phase is a colloid-poor gas, this low density phase will contain the larger particles.

Calculating Tie-lines

Projection of coexistence points onto the $\phi - c_{\mathrm{p}}$ plane is a useful operation, even in completely monodisperse samples. By so doing, we can graphically highlight the difference in both colloid *and* polymer densities between the coexistence phases. In polydisperse systems we will be able to discern whether or not such samples have compositions given by the relevant cloud point values, as is expected for monodisperse systems. However, directly measuring the polymer concentration in a sample is a non-trivial process.

Recently Bodnár and Oostebaan [107] have demonstrated a novel non-intrusive method for deducing tie-line endpoints, from careful measurements of coexistence phase volumes along at least three dilution lines. However, their technique is not applicable here as it assumes the monodisperse property of cloud, shadow and coexistence curves being identical.

I have instead used an indirect technique to measure c_{p}. Knowing (ϕ_{i}, $c_{\mathrm{p_i}}$) of the initial sample, ϕ_1 and ϕ_2, the coexistence volume fractions of upper and lower phases respectively and the equilibrium value for the relative volume of lower phase present f (equal to $f = (\phi_{\mathrm{i}} - \phi_1)/(\phi_2 - \phi_1)$ and taken at extraction time), it is possible to calculate the polymer concentrations in the two phases as described below.

Assuming the system is at equilibrium, the polymer chemical potentials μ_{p} are equal in both phases, and given by

$$\mu_{\mathrm{p}} = k_{\mathrm{B}} T ln(n_{\mathrm{p}}^{(\mathrm{free})} \lambda_{\mathrm{p}}^3) \tag{7.2}$$

where k_{B} is the Boltzmann constant, T is the temperature, $n_{\mathrm{p}}^{(\mathrm{free})}$ is the polymer number density in the free volume in the sample and λ_{p} is the de Broglie thermal wavelength for the polymer. The free volume V_{free} as defined earlier, is the fraction of the entire sample volume V_{T} which the centre of an idealised spherical polymer coil can access and is given by

$$V_{\mathrm{free}} = \alpha(\phi, \xi) V_{\mathrm{T}}. \tag{7.3}$$

The variable α is a function of ϕ and ξ and can be approximated using scaled particle theory [22]. By imposing equal chemical potentials in the two phases

$$\mu_{\mathrm{p_1}} = \mu_{\mathrm{p_2}}, \tag{7.4}$$

Equation 7.2 implies that number densities in the free volume are also equal,

$$n_{\mathrm{p_1}}^{(\mathrm{free})} = n_{\mathrm{p_2}}^{(\mathrm{free})} \tag{7.5}$$

as the other parameters in the definition of μ_{p} are constant. The experimentally accessible polymer concentration c_{p} is related to $n_{\mathrm{p}}^{(\mathrm{free})}$ by

$$n_{\mathrm{p}}^{(\mathrm{free})} = \frac{N_{\mathrm{A}}}{\alpha(\phi, \xi) M_{\mathrm{w}}} c_{\mathrm{p}} \tag{7.6}$$

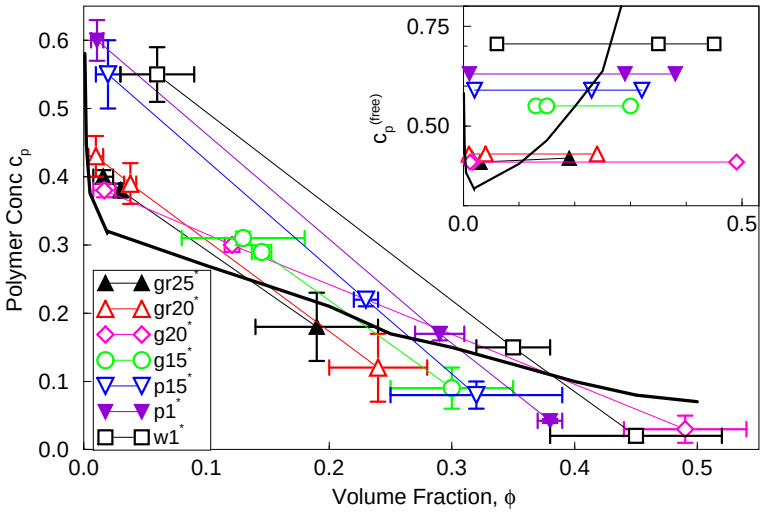

Figure 7.5: Experimental phase diagram showing tie-lines calculated for cloud curve samples. The solid line is the experimentally determined boundary between fluid and gas-liquid samples. The inset has vertical axis of polymer in the free volume.

where N_A is Avogadro's number. Equations 7.5 and 7.6 can be combined to give

$$\frac{c_{p_1}}{\alpha(\phi_1, \xi_1)} = \frac{c_{p_2}}{\alpha(\phi_2, \xi_2)} \tag{7.7}$$

where we allow different ξ's to account for colloidal size fractionation between the two phases. Conservation of polymer requires

$$c_{p_i} = (1 - f)c_{p_1} + f c_{p_2} \tag{7.8}$$

and Equations 7.7 and 7.8 can then be solved simultaneously to give values of c_{p_1} and c_{p_2}.

Following this prescription, I have calculated the polymer concentrations in each phase for the seven cloud-point samples, using the measured volume fractions and particle radii, the initial (ϕ_i,c_{p_i}) and the known value of r_g. These values, which are included in Table 7.1, have been used to construct 'semi-experimental' tie-lines, which are shown on the phase diagram in Figure 7.5. In the inset which has a vertical axis of $c_p^{(free)}$, the tie-lines are horizontal.

It is clear from Figure 7.5 that the coexistence phases do not lie directly on the observed cloud-point curve, but are situated within the marked uncertainties. Despite this, a trend is still apparent, that the fluid phases appear to be denser than (below and to the right of) the cloud-point curve, which is particularly evident in the inset plot. This observation is in qualitative agreement with observations for generic, polydisperse, phase separating systems: the dense arm of the coexistence curve for any initial volume fraction† is (for typical projections/measurements) at

†In polydisperse systems coexistence curves are defined for a particular initial density or volume fraction, as a function of another variable, such as temperature, or polymer concentration. See page 33.

higher densities than the observed line of instability (the cloud point curve). The validity of this statement does depend upon the particular projection onto the initial parameter space being used, but for cases in the polymer literature using practical projections via volume fraction measurements, this scenario of "denser than expected dense phases" has been observed [37, 41].

To my knowledge, my method for obtaining tielines has unfortunately not been applied to a monodisperse system where we expect coexistence samples to sit on the cloud-point curve. This would obviously help place more stringent limits on the interpretation of these data, determining whether the deviations from the cloud-point curve are due to polydispersity or experimental limitations.

Astute readers may have noticed that in the inset plot, the initial sample symbols (the points in the middle of the tie-lines) for Samples p15, p1 and w1 appear below the cloud point curve whereas in the main plot they are above it. The reason for this is that the initial homogeneous sample is in fact at a higher value of $c_{\mathrm{p}}^{(\mathrm{free})}$ (or chemical potential) than the equilibrium value. By phase separating, the sample creates more space for the polymers to explore and consequently the polymer concentration reduces to the equilibrium value. The initial sample points plotted on this inset have the correct values for ϕ_{i} but have values of $c_{\mathrm{p}}^{(\mathrm{free})}$ altered so as to lie on their respective straight tie lines. For example, the w1 sample has an initial polymer concentration in the free volume of $c_{\mathrm{p_i}}^{(\mathrm{free})} = c_{\mathrm{p}}/\alpha(\phi_{\mathrm{i}}, \xi_{\mathrm{i}}) = 150\%$ which reduces to $c_{\mathrm{p_i}}^{(\mathrm{free})} = 75\%$ after separation.

7.3.3 Testing the 'Universal Fractionation Law'

Background

A general, rigorous, perturbative approach to coexistence in slightly polydisperse systems was developed and tested by Evans, Poon and myself in [39]. The universal law derived therein states that the normalised difference between the n^{th} moments of the PSDs in two coexisting phases $\Delta\langle R^n\rangle \big/ \bar{R}$ is proportional to the normalised $(n+1)^{\mathrm{th}}$ moment of the parent distribtion $\langle R^{n+1}\rangle \big/ \bar{R}$:

$$\frac{\Delta\langle R^n\rangle}{\bar{R}} = \alpha \frac{\langle R^{n+1}\rangle}{\bar{R}}. \tag{7.9}$$

The non-universal coefficient α depends on intensive properties of the two phases (in this case, ξ, $\phi_{1,2}$ and $c_{\mathrm{p}_{1,2}}$), but is independent of the initial state and of the size distribution in the sample. This leads to (among others) two specific predictions. Firstly for all coexisting phases with equal α the difference in mean normalised sizes between each pair of phases ($\Delta R/\bar{R}$) varies only with the polydispersity of the parent distribution, via a squared dependency:

$$\frac{\Delta R}{\bar{R}} = \gamma\, \sigma_{\mathrm{p}}^2. \tag{7.10}$$

Secondly, by taking ratios we can eliminate the unmeasuraale constant γ in Equation 7.9. Dividing the $n = 2$ case by the $n = 3$ case yields

$$\frac{\Delta R}{\bar{R}} = \left(\frac{\sigma_{\mathrm{p}}^2}{\tau_{\mathrm{p}}^3}\right) \Delta\sigma^2. \tag{7.11}$$

The difference in mean normalised sizes between two coexistence daughter phases $\Delta R/\bar{R}$ is predicted to be proportional to the difference in the square of their polydispersities $\Delta\sigma^2$. The constant of proportionality depends only on the polydispersity and the skew ($\tau^3 = \left\langle (R - \bar{R})^3 \right\rangle / \bar{R}^3$) of the parent.

Testing Equation 7.10

To test the first of these predictions, gas-liquid samples were prepared, using Batches A and C to compare with samples p15, p1 and w1, previously prepared using Batch E colloid. The polydispersities (5.2% and 7.4% respectively) and mean radii (244 and 303 nm) of these particles were determied as described in Section 4.5. A separate polymer solution ($M_{\mathrm{w}} = 10.0 \times 10^6$ and 15.4×10^6) was prepared for both colloidal stocks ensuring a size ratio of $\xi = 0.45 \pm 0.03$ within the uncertainties of ξ for the Batch E samples ($\xi = 0.50 \pm 0.03$). From each stock, three mixtures were prepared at different concentrations, as indicated on the phase diagram in Figure 7.6. Despite the fact that these cover a broad region of the phase diagram, the coexisting gas and liquid phases vary primarily in fractional volume, and only slightly in composition between all nine samples. This similarity of gas phases and of liquid phases, and hence the justification of constant γ can be seen by considering the calculated tie-lines plotted on Figure 7.6, which terminate in localised gas and liquid regions. The similarity of all lower (and upper) phases was confirmed experimentally by the visual observation of similar turbidities.

Each of the samples was thoroughly mixed and then left undisturbed for observing. The protocol described previously for extraction (see Figure 4.6) was followed and the coexisting phases analysed by SLS to determine mean particle sizes, and hence a value for $\Delta\langle R^n \rangle \Big/ \bar{R}$ Figure 7.7 shows this value plotted as a function of parent polydispersity, on a log-log plot. The data was fitted by a power law and the exponent determined to be 2.2±0.3. This is in good agreement with the theoretical value of 2.

Testing Equation 7.11

Using the SLS fractionation data and the TEM histogram for the stock solution of Batch E particles, I calculated all the terms in expression 7.11 for each cloud point sample. In Figure 7.8 SLS measured values of $\Delta\sigma^2$ are plotted as a function of the normalised size difference. The errors are due to combined uncertainties in the SLS determined parameters and are larger for phases with larger polydispersities.

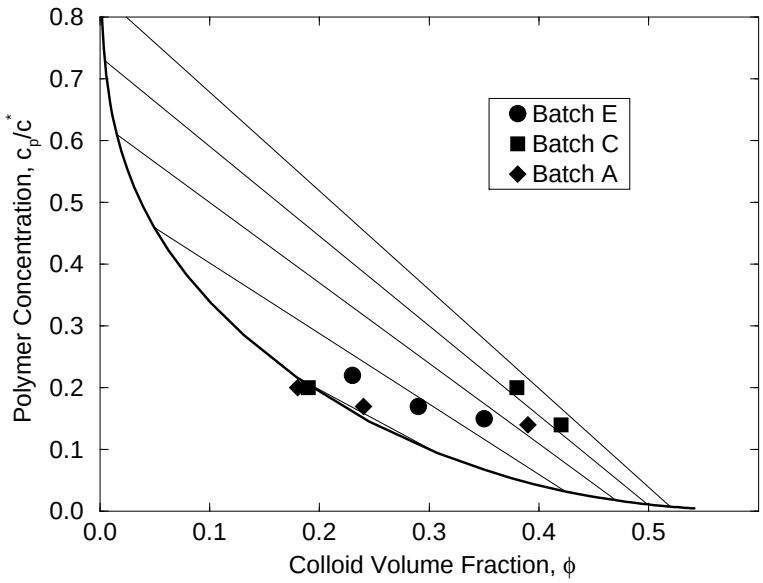

Figure 7.6: Gas-liquid samples prepared from Batches A, C and E. The theoretical boundary and tie-lines are calculated following the method of Lekkerkerker *et al.* [22]. The tie-lines corresponding to all the samples terminate in localised regions of the phase diagram, thereby somewhat justifying the assumption of constant γ.

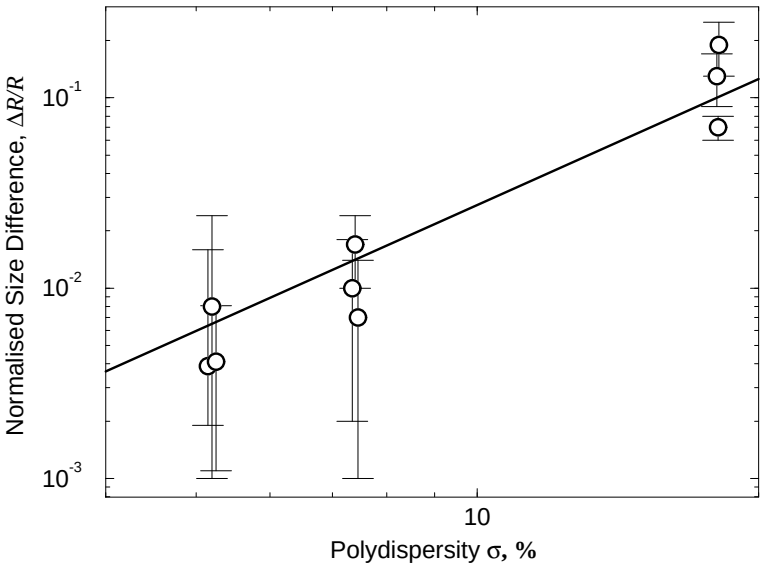

Figure 7.7: Log-log plot showing the difference in mean normalised sizes in coexisting phases as a function of the polydispersity of the parent solution. The bold line shows the power laws fit with exponent 2.2±0.3. The errors in σ are less than 10%.

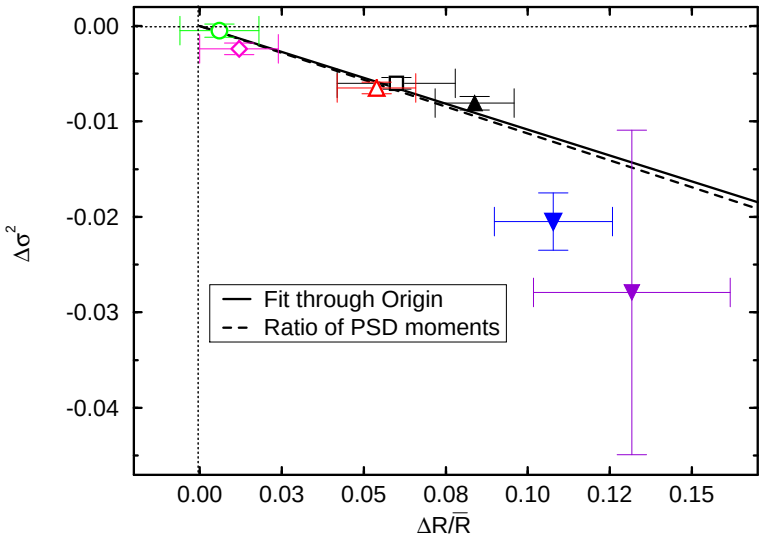

Figure 7.8: SLS fractionation data for cloud curve samples (symbols as before). Difference in polydispersity squared ($\Delta\sigma^2$) is plotted against normalised difference in radii ($\Delta R/\bar{R}$). The solid line is a fit through the data and the dashed line is the theoretical prediction using TEM data.

The straight line fit through these points, weighted by their respective errors, is in good agreement with the predictions of the theory based on the second to third moment ratio as measured by TEM histogram. Samples from near the critical point (g15 and g20) are those close to the origin on this plot, for which the fractionation is negligible.

These studies represent the first experimental test to date of the universal law, Equation7.9. Further implications of these predictions and other experimentally verifiable scenarios are discussed in the references [39, 108].

7.3.4 Mono- and Poly-disperse Kinetics

Figure 7.9 shows comparative sedimentation profiles for quasi-monodisperse Batch B and polydisperse Batch E samples. For large polymer concentrations, $c_p \approx 52\%$ both samples show the delayed sedimentation behaviour associated with transient gelation. The delay time for the polydisperse gel is approximately 10 hours longer than for the monodisperse case. As both samples are diluted, the difference becomes smaller, until below $c_p \approx 32\%$ when there is no noticeable difference in sedimentation profiles. [‡]

Unlike for crystallisation, polydispersity does not appear to hinder the kinetics in gel-formation and collapse or in gas-liquid separation. For the phase separations

[‡]Delay times are sensitive and presently unknown functions of many parameters, including sample height, width and temperature.

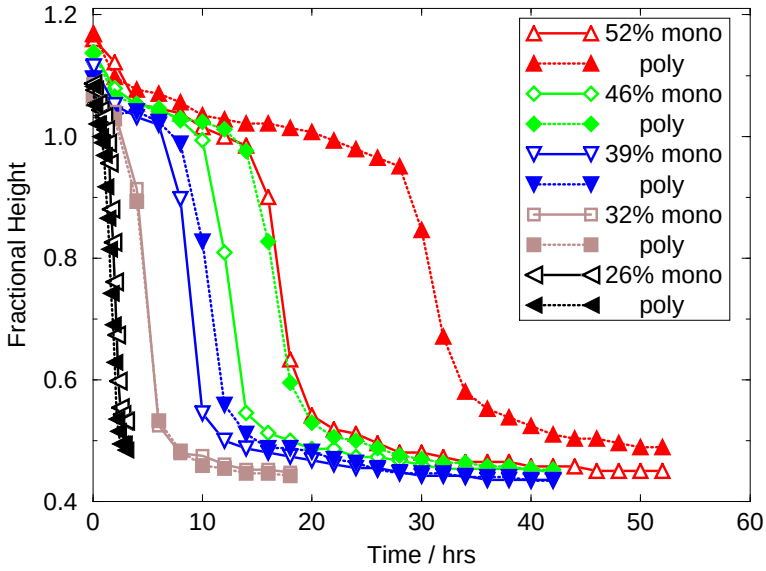

Figure 7.9: Comparative sedimentation profiles of monodisperse (open symbols) and polydisperse (filled symbols). All samples are at $\phi = 0.2$.

occurring in this case, a range of particle sizes will not disrupt the formation of a phase: in fact random phases generally prefer (have a lower free energy with) more polydisperse particles. Therefore, although the final, fully equilibrated state may be fractionated, it is conceivable that an intermediate density equilibrated state accompanied by a crisp interface between the phases would develop first, on a time-scale comparable to the monodisperse system. As I was only concerned with detecting equilibration by density observations, it is possible that the slower process of equilibration of higher moments via particle diffusion between ergodic phases, was still taking place.

The considerable practical problem of distinguishing these different kinetics has only recently come into the spotlight. Overcoming these difficulties will require advances in the synthesis of appropriate tagged particles to enable experimentalists to measure time resolved size distributions, in dense, evolving, coexistence phases.

7.3.5 Larger Polymer System

For completeness, I include here the phase diagram I measured for a polydisperse system with a larger size ratio. Samples were prepared using Batch E colloid in mixtures with $M_w = 15.4 \times 10^6$. The polymer radius of gyration at ambient temperature ($20 \pm 2^\circ$) is 152nm and the size ratio is $\xi \approx 0.75$.

The method I discussed above for determining phase behaviour was used again on these samples. Observations of developing interfaces allowed categorisation of

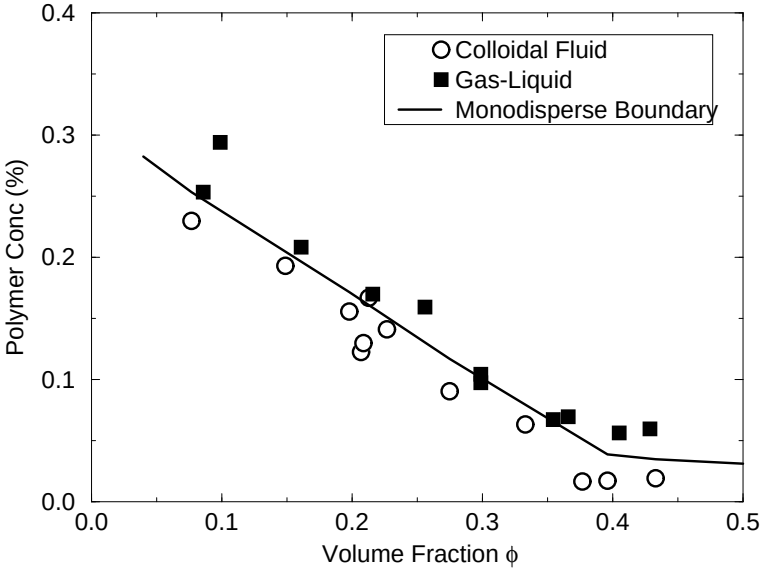

Figure 7.10: Phase Diagram for Batch E colloid plus random coil polymer with size ratio $\xi \approx 0.75$.

samples as either Gas-Liquid or Colloidal Fluid. Samples which initially showed Gas-Liquid behaviour were diluted until they crossed the cloud point curve and became stable Colloidal Fluids. The phase diagram is plotted in Figure 7.10 and the phase boundary, which appears to be particularly straight over the region studied, is drawn in by hand. The nature of the phase separation appeared to be similar to that studied above: a colloid-rich fluid phase and a colloid-poor upper phase developed after a few hours, and crystals were never seen. However, no further investigations were performed on this system and it is simply included for completeness.

7.4 Conclusions

In addition to presenting experimental results for a specific polydisperse system the work in this chapter also raises questions for more general multicomponent systems.

Is 20% *polydispersity insufficient in general to cause experimentally detectable shifts in the location of the cloud-point curve ?*
My findings substantiate the affirmative response to this question, and, for example, Kita and co-workers found that for polymer systems at higher polydispersities ($M_{\rm w}/M_{\rm n} = 2.8$ equivalent to $\sigma_{\rm r_g} \approx 60\%$) there is an experimentally observable shift [41]. Perhaps using Evans' definition of "small" polydispersity (the Hamiltonian as a function of non-identical parameter is effectively flat over the range of species considered) it will be possible to determine *a priori* whether a particu-

lar width of distribution will noticeably disrupt the phase behaviour for a given system. (Admittedly, this does require a good expression for the Hamiltonian to start with.)

Will the "universal law" be corroborated for other polydisperse systems ?
I have presented the first experimental test of this law. It will be interesting to see if other multi component systems will also comply.

How can we measure fractionation kinetics ?
For the colloid-polymer system studied here, polydispersity does not appear to alter the kinetics of zeroth moment or density equilibration. So unfortunately, no new industrial techniques for increasing shelf-life by manipulating the size distributions of components were discovered. However, the problems involved in measuring and understanding the equilibration of higher moments, and hence the kinetics of fractionation has been touched upon.

What does this say about the Gibb's phase rule ?
Gibb's predicted that a system can separate into as many phases as it has free parameters (e.g. density, volume ..). Multicomponent systems, which have individual densities for each species, can theoretically separate into a multitude of phases. That this multi-phase coexistence was not observed implies that greater polydispersity, and perhaps energies which depend more sensitively on the polydisperse parameter, would be required before we see more than three phase coexistence.

Chapter 8

Conclusions

8.1 Summary of Results

In this work I have presented a detailed experimental investigation into the phase behaviour of polydisperse spherical colloids in three different systems.

8.1.1 Hard-Sphere Colloids

Firstly, I considered the hard-sphere system and mapped out the volume fraction-polydispersity phase diagram. Samples with $\sigma \lesssim 7\%$ showed crystallization behaviour almost indistinguishable from quasi-monodisperse hard spheres. Samples with $\sigma \approx 10\%$ only crystallized in the coexistence region, up to a maximum of 97% crystallized, with 3% coexisting fluid. The obvious implication of this observation is that for systems at this polydispersity a fluid phase is essential for crystallization, acting as a type of "rubbish bin" into which are deposited all the particles from the fringes of the distribution which would normally disrupt the formation of a lattice. This would also explain the observed slower kinetics, as more time would be required for the long-scale diffusion necessary to achieve such a sorting of particles. However, bulk fractionation studies show no such phenomenon, so we conclude that *in the bulk* both crystal and fluid phases are composed of very similar distributions of particles. However, we do not dismiss the possibility of variation in mean particle sizes between coexisting crystallites. Dynamic light scattering studies indicate that the slow dynamics may be caused by a glass transition. This effect would be sufficient to prevent complete crystallisation. The width of the coexistence region does not diminish with increasing polydispersity in the range studied. We found initial evidence for an increase in the melting and freezing volume fractions, but until the present difficulties involved in precisely measuring volume fractions for polydisperse spheres are resolved, this issue will remain uncertain.

8.1.2 Colloid plus Small Polymer

On adding small random coil polymer to these hard sphere colloids, we expect the coexistence gap to increase in width. This has been previously observed experimentally in quasi-monodisperse systems. However, when I added small polymer to the polydisperse colloid, this broadening was not observed. A simple explanation for this is that due to the additional osmotic pressure of the polymer solution the crystal phase is squeezed to volume fractions above the value at which a polydisperse crystal is stable. We calculated this value using an idea of Pusey's, based on the Lindemann melting criterion. By incorporating a cell model free energy for a polydisperse hard-sphere crystal into the standard colloid-polymer theory a phase diagram was calculated. This simple approach does not allow for fractionation between crystal and fluid phases, but nevertheless reproduces similar looking phase diagrams to those measured experimentally. After slight scaling along both axes the calculated boundaries overlay the experimental data almost exactly. Studies of other predictions of this approach, including a re-entrant fluid phase and even the presence of a triple region are left as exercises for the interested reader.

8.1.3 Colloid plus Large Polymer

The third part of this investigation involved adding larger polymer to a colloidal suspension which was known to be too polydisperse to crystallise normally. The only expected coexistence was between gas and liquid phases, and this was indeed observed. In fact, in this situation, polydispersity neither shifted the phase boundaries nor affected the kinetics of the phase separation compared to the quasi-monodisperse case. Detailed study of the fractionation of particle sizes and polydispersities between coexisting phases enabled experimental testing of a very general and widely applicable fractionation law.

8.2 Suggestions for Future Work

Several possible avenues of further exploration, inspired by this and other investigations in the field of colloidal polydispersity, spring to mind. Those which extend directly from my observations were previously suggested in the appropriate chapters, so here I present more speculative ideas. Detailed study of the properties of crystallization in a hard-sphere system, using precise extraction techniques which permit the mechanical retrieval of single crystallites, would enable the fractionation-on-freezing question to be answered definitively. My cursory look at how shear aids crystallization in polydisperse systems prompts much more detailed attention. Also, long time studies of how sedimentation and gravity play a rôle in crystallisation of very polydisperse hard-sphere systems, would be very interesting in the light of the observed crystal bands for $\sigma \approx 18\%$ samples in

this work, and by others. Further experimental verification of the universal fractionation law would also be very exciting. On the theoretical front, it would be interesting to see how the results obtained from the simple approach at solving the polydisperse-colloid-plus-polymer system would compare with more rigorous simulations or theoretical treatments. Finally, looking at kinetics in polydisperse systems, including such ideas as the dynamics of moment equilibration, would open up a whole new can of worms.

Bibliography

[1] L.D. Landau and E.M. Lifshitz. *Statistical Physics*, volume 5. Pergamon Press Ltd., Oxford, 3rd edition, 1980.

[2] L.E. Reichl. *A modern course in statistical physics*. Univeristy of Texas Press, 1984.

[3] J.W. Gibbs. *The Scientific Papers of J.Willard Gibbs*, volume 1. Ox Bow Press, Woodbridge, Connecticut, U.S.A., 1993.

[4] G.K. Batchelor. Brownian diffusion of particles with hydrodynamic interaction. *J. Fluid Mech.*, 74(1):1–29, 1976.

[5] J.K.G Dhont. *An introduction to dynamics of colloids*. Elsevier, Amsterdam, 1996.

[6] N.F. Carnahan and K.E. Starling. Equation of state for nonattracting rigid spheres. *J.Chem.Phys.*, 51:635, 1969.

[7] K.R. Hall. Another hard-sphere equation of state. *J.Chem.Phys.*, 57:2252, 1972.

[8] W.G. Hoover and F.H. Ree. Melting transition and communal entropy of hard spheres. *J.Chem.Phys.*, 49(8):3609–3617, 1968.

[9] S-E. Phan, W.B. Russel, Z. Cheng, J. Zhu, P.M. Chaikin, J.H. Dunsmuir and R.H. Ottewill. Phase transition, equation of state and limiting shear viscosities of hard sphere dispersions. *Phys.Rev.E.*, 54(6), 1996.

[10] S.B. Yuste, M. López de Haro and A. Santos. Structure of hard-sphere metastable fluids. *Phys.Rev.E*, 53(5):4820–4826, 1996.

[11] G.A. Mansoori, N.F. Carnahan, K.E. Starling and T.W. Leland, Jr. Equilibrium thermodynamic properties of the mixture of hard spheres. *J.Chem.Phys.*, 54(1):1523–1525, 1971.

[12] R.J. Buehler, R.H. Wentorf, J.O. Hirschfelder and C. Curtiss. The free volume for rigid spherical molecules. *J.Chem.Phys.*, 19(61):61–71, 1951.

[13] R.P. Sear. Phase separation and crystallisation of polydisperse hard spheres. *Europhys. Lett.*, 44(4):531–535, 1998.

[14] J-P. Hansen, D. Levesque and J. Zinn-Justin, editors. *Liquids, Freezing and the Glass Transition.* Elsevier, Amsterdam, 1991.

[15] W. van Megen and P.N. Pusey. Dynamic light-scattering study of the glass transition in a colloidal suspension. *Phys.Rev.A*, 43(10):5429–5441, 1991.

[16] S. Asakura and F. Oosawa. *J. Polymer Sci.*, 33:183, 1958.

[17] A. Vrij. *Pure and Applied Chem.*, 48:471, 1976.

[18] J.L. Lebowitz, E. Helfand and E. Praestgaard. Scaled particle theory of fluid mixtures. *J.Chem.Phys.*, 43(3):774–779, 1965.

[19] M. Dijkstra, R. van Roij and R. Evans. Direct simulation of the phase behaviour of binary hard-sphere mixtures: Test of the depletion potential description. *Phys.Rev.Lett.*, 82(1):117–120, 1999.

[20] Y.N. Ohshima, H. Sakagami, K. Okumoto, A. Tokoyoda, T. Igarashi, K.B. Shintaku, S. Toride, H. Sekino, K. Kabuto and I. Nishio. Direct measurement of infinitessimal depletion force in a colloid-polymer mixture by laser radiation pressure. *Phys.Rev.Lett.*, 78(20):3963–3966, 1997.

[21] X. Ye, T. Narayanan, P. Tong, J.S. Huang, M.Y. Lin, B.L. Carvalho and L.J. Fetters. Depletion interactions in colloid-polymer mixtures. *Phys.Rev.E*, 54(6):6500–6510, 1996.

[22] H.N.W. Lekkerkerker, W.C.K. Poon, P.N. Pusey, A. Stroobants and P.B. Warren. Phase-behaviour of colloid plus polymer mixtures. *Europhys.Lett.*, 20(6):559–564, 1992.

[23] R.M.L. Evans, W.C.K. Poon and M.E. Cates. Role of metastable states in phase ordering dynamics. *Europhys.Lett.*, 38(8):595–600, 1997.

[24] W.C.K. Poon, F. Renth, R.M.L. Evans, D.J. Fairhurst, M.E. Cates and P.N. Pusey. Phase separation kinetcis in colloid polymer mixtures at triple coexistence: Kinetic maps from free energy landscapes. submitted to *Phys.Rev.Lett.*

[25] A.D. Pirie. *A light scattering study of colloid-polymer mixtures.* PhD thesis, University of Edinburgh, 1995.

[26] P.N. Pusey, A.D. Pirie and W.C.K. Poon. Gelation in colloid polymer mixtures. *Physica A*, 201:322, 1993.

[27] W.C.K. Poon, L. Starrs, S.P. Meeker, A. Moussaïd, P.N. Pusey and R.M.L. Evans. Delayed sedimentation of transient gels in colloid-polymer mixtures: dark field observations, rheology and dynamic light scattering studies. to appear in *Faraday Discuss.* 102.

[28] W.C.K. Poon, A.D. Pirie and P.N. Pusey. Gelation in colloid-polymer mixtures. *Faraday Discuss.*, 1995.

[29] P.B. Warren. Combinatorial entropy and the statistical mechanics of polydispersity. *Phys.Rev.Lett.*, 80(7):1369–1372, 1998.

[30] P. Sollich and M.E. Cates. Projected free energies for polydisperse phase equilibria. *Phys.Rev.Lett.*, 80(7):1365–1368, 1998.

[31] A. van Beurten, P. annd Vrij. Polydispersity effects in the small-angle scattering of concentrated solutions of colloidal spheres. *J.Chem.Phys*, 74:2744–2748, 1981.

[32] W. Hartl nad C.Segschneider, H.Versmold and P.Linse. On the structure factor of liquid-like ordered binary-mixtures of colloidal suspensions. *Mol.Physics*, 73(3):541–552, 1991.

[33] T DeDonder. *L'Affinite (deuxieme partie).* Gauthier-Villars, Paris, 1931.

[34] E. Dickinson. Polydispersity and osmotic pressure of stable ordered colloidal dispersions. *J.Chem.Soc.Faraday II*, 75:466–473, 1979.

[35] E. Dickinson, R. Parker and M. Lal. Polydispersity and the colloidal order-disorder transition. *Chem.Phys.Lett.*, 79(3):578–582, 1981.

[36] E. Dickinson and R. Parker. Polydispersity and the fluid-crystalline phase-tranisition. *J.Phys.Lett*, 46(6):229–232, 1985.

[37] R. Koningsveld. Liquid-liquid equilibria in multicomponent polymer systems. pages 144–161, 1970.

[38] J.A. Gualtieri, J.M. Kincaid and G. Morrison. Phase equilibria in polydisperse fluids. *J.Chem.Phys*, 77:521–536, 1982.

[39] R.M.L. Evans, D.J. Fairhurst and W.C.K. Poon. Universal law of fractionation for slightly polydisperse systems. *Phys.Rev.Lett.*, 81(6):1326–1329, 1998.

[40] P.J. Flory. *Principles of Polymer Chemistry.* Cornell, Ithaca, 1953.

[41] R. Kita, T. Dobashi, T. Yamamoto, M. Nakata and K. Kamide. Coexistence curve of a polydisperse polymer near the critical point. *Phys.Rev.E*, 55:3159–3163, 1997.

[42] N. Clarke, T.C.B. McLeish and S.D. Jenkins. Phase behaviour of linear/branched polymer blends. *Macromolecules*, 28:4650–4659, 1995.

[43] G.C. Berry. Thermodynamic and conformational properties of polystyrene. I. Light-scattering studies on dilute solutions of linear polystyrenes. *J.Chem.Phys.*, 44(12):4550–4564, 1966.

[44] T. Coussaert and M. Baus. Demixing vs freezing of binary hard-sphere mixtures. *J.Chem.Phys.*, 109(14):6012–6020, 1998.

[45] P.B. Warren. Fluid-fluid phase separation in polydisperse hard sphere mixtures. preprint cond-mat/9807117.

[46] J.A. Cuesta. Demixing in a single-peak distributed polydisperse mixture of hard spheres. preprint cond-mat/9807030.

[47] W. Schaertl and H. Sillescu. Brownian dynamics of polydisperse colloidal hard spheres: Equilibrium structures and random close packings. *J.Stat.Phys*, 77:1007–1025, 1994.

[48] J. Bibette. Depletion interactions and fractionated crystallization for polydisperse emulsion purification. *J.Coll.Int.Sci.*, 147(2):474–479, 1991.

[49] J. Bibette, D. Roux and B. Pouligny. Creaming of emulsions: the role of depletion forces induced by surfactant. *J.Phys.II*, 2:401–424, 1992.

[50] J. Bibette, D. Roux and F. Nallet. Depletion interactions and fluid-solid equilbrium in emulsions. *Phys.Rev.Lett.*, 65(19):2470–2473, 1990.

[51] X.L. Chu, A.D. Nikolov and D.T. Wasan. Effects of particle-size and polydispersity on the depletion and structural forces in colloidal dispersions. *Langmuir*, 12(21):5004–5010, 1996.

[52] Y. Mao. Depletion force in polydisperse systems. *J.Physique II*, 5(12):1761–1766, 1995.

[53] J.Y. Walz. Effect of polydispersity on the depletion interaction between colloidal particles. *J.Coll.Int.Sci*, 178(2):505–513, 1996.

[54] P.B. Warren. Phase behavior of a colloid plus binary polymer mixture: Theory. *Langmuir*, 13(17):4588–4594, 1997.

[55] R.P. Sear and D. Frenkel. Phase behaviour of colloid plus polydisperse polymer mixtures. *Phys.Rev.E*, 55:1677–1681, 1997.

[56] M.R. Stapleton, D.J. Tildesley and N. Quirke. Phase equilibria in polydisperse fluids. *J.Chem.Phys.*, 92:4456–4467, 1990.

[57] E. Salomons and M. Mareschal. Atomistic simulation of liquid-vapour coexistence in binary mixtures. *Europhys.Lett.*, 16:85–90, 1991.

[58] L. Pan and S. Toxvaerd. Phase separation in two-dimensional binary fluids of different-sized molecules: A molecular-dynamics study. *Phys.Rev.E*, 54:6532–6536, 1996.

[59] J. Janča. Isoperichoric focusing phenomenon in bidisperse suspension of colloidal particles. *J.Coll.Int.Sci*, 189:51–57, 1997.

[60] K.E. Davis, W.B. Russel and W.J. Glantschnig. Settling suspension of colloidal silica: Observation and x-ray measurements. *J.Chem.Soc. Faraday Trans.*, 87(3):411–424, 1991.

[61] T. Biben and J-P. Hansen. Localized density profiles in binary colloidal suspensions. *Molecular Phys.*, 80(4):853–859, 1993.

[62] I. Moriguchi, K. Kawasaki and T. Kawakatsu. The effects of size polydispersity in nearly hard sphere colloids. *J.Phys. II France*, 3:1179–1184, 1993.

[63] P.B. Warren. Combinatorial entropy and the statistical mechanics of polydispersity. Technical report, Unilever, 1997.

[64] L. Antl, J.W. Goodwin, R.D. Hill, R.H. Ottewill, S.M. Owens and S. Papworth. The preparation of poly(methyl methacrylate) latices in non-aqueous media. *Colloids and Surfaces*, 17(1):67–78, 1986.

[65] C. Pathmamanoharan, C. Slob and H.N.W. Lekkerkerker. Preparation of polymethylmethacrylate latices in non-polar media. *Colloid Polym. Sci.*, 267:448–450, 1989.

[66] Jean-Batise Perrin. *Brownain Motion and Molecular Reality.* Red Lion Court, Fleet Street, London, 1910. translated by F.Soddy.

[67] V. Martelozzo. Private Communication.

[68] S.E. Paulin and B.J. Ackerson. Observation of a phase transition in the sedimentation velocity of hard spheres. *Phys.Rev.Lett.*, 64(22):2663–2666, 1990.

[69] M.D. Eldridge, P.A. Madden, P.N. Pusey and P. Bartlett. Binary hard-sphere mixtures: a comparison between computer simulation and experiment. *Mol.Phys.*, 84(2):395–420, 1995.

[70] B.H. Zimm. Apparatus and methods for measurement and interpretation of the angular variation of light scattering; preliminary results on polystyrene solutions. *J.Chem.Phys.*, 16(12):1099–1116, 1948.

[71] P.N. Pusey. Measurement of diffusion coefficients of polydisperse solutes by intensity fluctuation spectroscopy. In J.H.S. Green and R. Dietz, editors, *Industrial Polymers: Characterization by Molecular Weight*, pages 26–36. Transcripta Books, London, 1973.

[72] F. Ferri. Use of a charge coupled device camera for low-angle elastic light scattering. *Rev. Sci. Instrum.*, 68(6):1–10, 1997.

[73] B.J. Berne and R. Pecora. *Dynamic Light Scattering.* Wiley, New York, 1976.

[74] P.N. Pusey and W. van Megen. Detection of small polydispersities by photon correlation spectroscopy. *J.Chem.Phys*, 80:3513–3519, 1984.

[75] D.J. Fairhurst. Unpublished.

[76] O. Glatter. Determination of particle-size distribution functions from small-angle scattering data by means of the indirect transformation method. *J.App.Cryst.*, 13(7-11), 1980.

[77] B. Saleh. *Photoelectron Statistics*. Springer-Verlag, Berlin Heidelberg New York, 1978.

[78] P.N. Pusey. Colloidal suspensions. In Hansen et al. [14], chapter 10.

[79] G. Parry and P.N. Pusey. *J. Opt. Soc. Am.*, 69:796, 1979.

[80] P.N. Pusey and W. van Megen. Phase-behaviour of concentrated suspensions of nearly hard spheres. *Nature*, 320:340–342, 1986.

[81] J.L. Harland and W. van Megen. Crystallization kinetics of suspensions of hard colloidal spheres. *Phys.Rev.E*, 55(3):3054–3067, 1997.

[82] S.I. Henderson and W. van Megen. Metastability and crystallization in suspensions of mixtures of hard spheres. *Phys.Rev.Lett.*, 80(4):877–880, 1998.

[83] P. Bartlett, P.N. Pusey and R.H. Ottewill. Colloidal crystallization under time-averaged zero gravity. *Langmuir*, 7:213–215, 1991.

[84] S.I. Henderson, T.C. Mortensen, S.M. Underwood and W. van Megen. Effect of particle size distribution on crystallisation and the glass transition of hard sphere colloids. *Physica A*, 233:102–116, 1996.

[85] P. Bartlett and P.B. Warren. Re-entrant melting in polydisperse hard spheres. preprint cond-mat/9902029.

[86] W. van Megen, S.M. Underwood and P.N. Pusey. Nonergodicity parameters of colloidal glasses. *Phys.Rev.Letts.*, 67(12):1586–1589, 1991.

[87] P. Bartlett. Fractionated crystallisation in a polydisperse mixture of hard spheres. *J. Chem. Phys.*, 109(24):10970–10975, 1998.

[88] D.J. Fairhurst, W.C.K. Poon and A. Moussaïd. Polydispersity in hard sphere colloids. in preparation.

[89] J.L. Barrat and J.P. Hansen. On the stability of polydisperse colloidal crystals. *J.Physique*, 47:1547–1553, 1986.

[90] R. McRae and A.D.J. Haymet. Freezing of polydisperse hard spheres. *J.Chem.Phys.*, 88:1114–124, 1988.

[91] P.G. Bolhuis and D.A. Kofke. Monte carlo study of freezing of polydisperse hard spheres. *Phys.Rev.E*, 54(1):634–643, 1996.

[92] P. Bartlett. A geometrically-based mean-field theory of polydisperse hard-sphere mixtures. *J.Chem.Phys.*, 107(1):188–196, 1997.

[93] S-E. Phan, B. Russel, J. Zhu and P.M. Chaikin. Effects of polydispersity on hard sphere crystals. *J.Chem.Phys*, 108(23):9789–9795, 1998.

[94] P.N. Pusey. The effect of polydispersity on the crystallization of hard spherical colloids. *J.Physique*, 48:709–712, 1987.

[95] P.G. Bolhuis and D.A. Kofke. Freezing of polydisperse hard spheres. *Phys.Rev.E*, 59(1):618–622, 1999.

[96] P. Bartlett. Private communication.

[97] B.J. Ackerson and K. Schätzel. Classical growth of hard-sphere colloidal crystals. *Phys.Rev.E*, 52(6):6448–6459, 1995.

[98] M.D. Haw, W.C.K. Poon and P.N. Pusey. Direct observation of oscillatory-shear-induced order in colloidal suspensions. *Phys. Rev. E*, 57(6):6859–6864, 1998.

[99] P. Bartlett. Private communication.

[100] A.B. Schofield. Private communication.

[101] S.M. Illett. Private communication.

[102] S.M. Ilett, A. Orrock, W.C.K. Poon and P.N. Pusey. Phase beahviour of a model colloid-polymer mixture. *Phys.Rev.E*, 51:1344–1352, 1995.

[103] P.B. Warren. Private communication.

[104] R. Buscall, J.W. Goodwin, R.H. Ottewill and T.F. Tadros. The settling of particles through Newtonian and non-Newtonian media. *J.Coll.Int.Sci.*, 85(1):78–86, 1982.

[105] M.F. Soliva. Private communication.

[106] L. Starrs. Private Communication.

[107] I. Bodnar and W.D. Oosterbaan. Indirect determination of the composition of the coexisting phases in a demixed colloid polymer mixture. *J.Chem.Phys.*, 106(18):7777–7780, 1997.

[108] Glenn H. Fredrickson. Imperfect fluids and inheritance. *Nature*, 395:323–324, 1998.